Rheology and Pipeline Flow Behavior of Fumed Silica Nanoparticle Suspensions

by

Arshdeep Singh

A thesis
presented to the University of Waterloo
in fulfillment of the
thesis requirement for the degree of
Master of Applied science
in
Chemical Engineering

Waterloo, Ontario, Canada, 2018

Author's Declaration

I hereby declare that I am the sole author of this thesis. This is a true copy of the thesis, including any required final revisions, as accepted by my supervisor and examiners.

I understand that the thesis may be made electronically available to the public.

ABSTRACT

Suspensions are used in a wide variety of industrial and household applications; some examples being paints, ink, wastewater streams, cough syrups, and sauces. Rheology of suspensions depends on various factors such as the particle size, shape and their surface chemistry other than the nature of the continuous phase. Nanoparticles, when used to produce suspensions offer unique rheological properties due to their extremely small size and high surface area. In this study, fumed silica nanoparticles of hydrophilic grade were used to form suspensions in water. Three different hydrophilic grades of fumed silica nanoparticles were chosen for rheological studies. Various properties such as zeta potential, particle size distribution, rheological and pipeline flow behavior were studied as a function of concentration, pH change, temperature, and presence of an electrolyte in the study.

The results show that the silica nanoparticles form stable suspensions in water. The suspensions show shear-thinning behavior for the range of shear rates investigated. With an increase in particle concentration, the suspensions become more and more viscous. The Dynamic light scattering results show that the particle size increases with an increase in concentration. The shear viscosity decreases with an increase in temperature. Zeta potential results show that the particles are negatively charged in the aqueous phase and zeta potential value decreases in magnitude with an increase in particle concentration. The size distribution peaks do not show any pattern with a change in pH in the absence of an electrolyte whereas, in the presence of an electrolyte, the peaks move toward higher particle size confirming the presence of bigger aggregates in the presence of an electrolyte. The relative viscosity of suspensions increases more rapidly than the Einstein equation for hard spheres. Also, the relative viscosity at low pH value is higher for very low particle concentration suspensions but with an increase in concentration, suspensions show higher viscosity at high pH values. An addition of an electrolyte has a sharp increasing effect on the viscosity of dilute suspensions. Also, zeta potential turns more and more negative with increase in pH in the absence of an electrolyte whereas zeta potential values get compressed in the presence of an electrolyte. Pipeline flow results show that suspensions show drag reduction characteristics for very low particle concentration samples whereas almost no drag reduction properties for relatively higher particle concentration suspensions.

Acknowledgements

Table of Contents

List of Figures

List of Tables

Chapter 1: Introduction

1.1 Background:

Silicon and Oxygen are the most common constituents of earth's crust and together they form silicon dioxide (SiO_2), commonly referred to as Silica. The building block of silica and silicate structures is SiO_4 tetrahedron where oxygen is covalently bonded to silica in a tetrahedral geometry with four of the oxygen atoms covalently bonded to each silicon atom; hence forming large interconnected networks [1]. Silica can be classified on the basis of whether it is natural or synthetically produced, is in a crystalline form such as quartz or in an amorphous form such as glass. The Figure 1 given below depicts silica in an amorphous form:
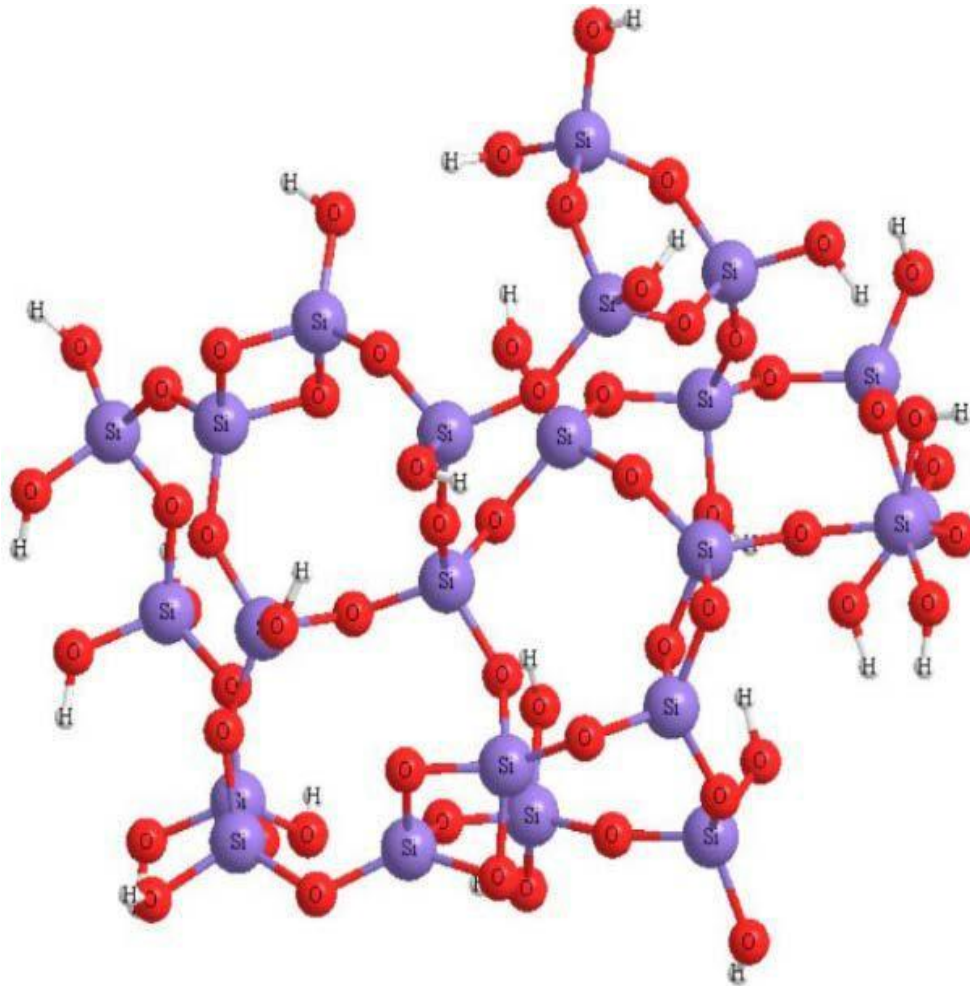
Figure 1: Amorphous structure of Silicon dioxide [2]

Silica nanoparticles (SiO$_2$) have been a part of extensive research due to their numerous applications [3-5]. Another interesting property of silica nanoparticles is that they can be chemically modified to suit various applications [6] and their properties like shape, size, surface area, porosity can be precisely controlled to suit them for diverse applications [7]. Silica is an abundant material and is found in many minerals on earth, is found in sand and clay mostly in its crystalline form, which is Quartz [8].

1.2 Fumed silica:

Fumed Silica, is the non-crystalline form of silica. It is usually produced as fine and very small particles with a high surface area and low bulk density prepared via the flame hydrolysis process [9]. Owing to its small particle size, special morphology, unique surface properties, these particles find their usage in many applications in industry. The specific surface area of fumed silica powders can range anywhere from 50 to 600 m^2/g [10].

1.2.1 Manufacturing process:

The manufacturing process of fumed silica powder is a vapor-based process operated at elevated temperatures. It is generally prepared via hydrolysis reaction of vapors of Silicon tetrachloride (SiCl$_4$) in the presence of hydrogen and oxygen at a temperature of 1000 °C [11]. The flame hydrolysis is essentially a process that involves the reaction of the mixture of a precursor (commonly a metal chloride), air/water and Hydrogen in a reactor. The process is generally operated on a continuous basis. The precursor, such as metal chloride reacts with water vapor which is formed by the reaction of Oxygen and Hydrogen present in the mixture [12]. The reactions involved in the production process of fumed silica are mentioned as follows:

$$2H_2 + O_2 \rightarrow 2H_2O$$

$$SiCl_4 + 2H_2O \rightarrow SiO_2 + 4HCl$$

$$\overline{2H_2 + O_2 + SiCl_4 \rightarrow SiO_2 + 4HCl} \tag{1}$$
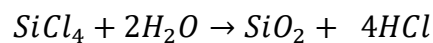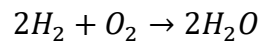
The reaction of SiCl$_4$ (Silicon tetrachloride) when it burns in oxygen and hydrogen flame, produces primary particles. While it is in a molten state, the primary particles constantly collide with each other; they fuse together into bigger secondary particles called as aggregates, by surface interactions. Before the separation of silica particles from HCl, the reaction mixture is sent to a cooling zone. The silica particles, being very small and having a huge surface area, physically

absorb the HCl which is removed by the treatment of Silica with moist air. This treatment, in turn, lowers the content of HCl in silica product to a very low value i.e. 0.025 % [11]. The controlling parameters for bringing out a change in surface area of fumed silica powders are the proportion in which reactants are added, the temperature of the reaction mixture and turbulence of the flow [13]. The aggregates in fumed silica particle suspensions, often form agglomerates due to attractive forces between them. A graphical representation of the formation of agglomerates is presented in the figure given below:
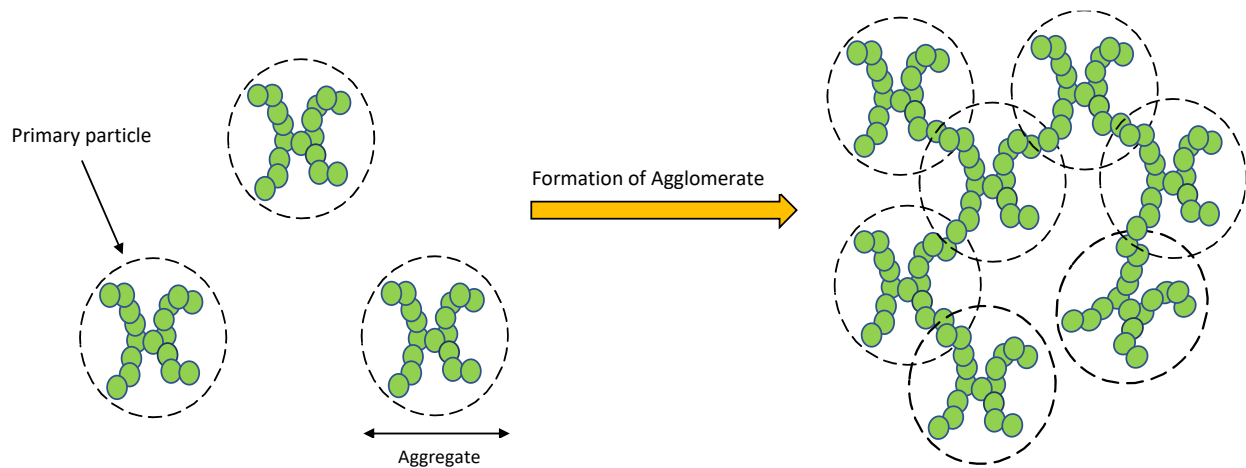
Figure 2: Schematic representation of the formation of an agglomerate from aggregates [10]

1.2.2 Classification of fumed silica:

Fumed silica exists in different grades depending upon the nature of primary particle's surface. It can be broadly classified into two types as given below:

1. **Hydrophilic Silica:** It has been found that Silanol groups (Si-OH) groups are present on the surface of silica [14]. A silanol group is present per every second atom of silica. Due to the presence of such large numbers of these groups, interactions by fumed silica particles are majorly governed by those groups. Owing to the silanol groups on its surface and its oxide nature, the fumed silica produced by flame hydrolysis process is hydrophilic in nature [15].

2. **Hydrophobic Silica**: The hydrophobic silica is produced by chemical conversion of surface groups i.e. Si-O-H groups on its surface. The elimination of hydroxyl bonds present on the originally hydrophilic surface can lead to a hydrophobic surface. This can be done by a treatment of hydrophilic grade silica with alkyl chloro-silanes or alkyl silazanes which deactivates the surface silanol groups and the surface becomes hydrophobic [15,16].

1.2.3 Applications of fumed silica:

Fumed silica, due to its unique properties, provides benefits for many consumer and industrial applications, some which are:

1. **Composite polymer electrolyte for batteries:** The usage of solid polymer electrolytes in batteries has many benefits; they help get rid of battery leakage, there is no more need for a separator and they are also capable of being produced at low cost. But they suffer from low conductivity problem. If silica is introduced as a filler, it forms a three-dimensional network and hence the composite polymer electrolytes then show high conductivity value, mechanical stability, and easy processability. The composite also exhibits shear thinning behavior which is also beneficial for electrolyte processing [17].

2. **For removal of excess phosphorous from wastewater:** Phosphorus is a very vital nutrient, but an excess of phosphorus can cause a problem which is eutrophication of water bodies. Investigations show that fumed silica powder when used within coordination with pulverized oyster shell, calcined and hydrothermally annealed at a certain temperature and batch time produces a material that can remove phosphorous which does not break down easily to form sludge. This phosphate removal material can readily remove phosphate by precipitating Ca-phosphates. So, fumed silica can be used as a reagent for phosphorous removal [18].

3. **Producing photocatalytic material:** Fumed silica and TiO_2 composite porous ceramic material prepared using phosphoric acid binder changes the photocatalytic activity of TiO_2. The photocatalytic porous ceramic material thus produced exhibits higher tensile stress, higher surface areas and a reasonable activity as a photocatalyst. It also overcomes common limitations associated with TiO_2 i.e. separation and recovery issues with the TiO_2 based originally used photocatalytic material [19].

4. **Removal of Zinc (Zn) from wastewater:** Heavy metals, such as Zinc are being continuously released into the environment due to industrial processes and are a health hazard for human and for aquatic habitat [20]. Electrodialysis is one of the various methods that are in place to remove heavy metals from a stream of wastewater. It involves the application of electric potential difference which brings ions in motion which are separated using a semipermeable membrane [21, 22]. It was found that the polymer membranes used for dialysis when doped with fumed silica powder experience a significant increase in performance; the membranes

were more resistant to fouling and ionic conductivity and membrane hydrophobicity was also enhanced [23].

5. **Rheology control:** The usage of paints and coating for a particular application depend a lot on their flow behavior. To meet the requirements such as high surface finish and good leveling characteristics, different binders and additives have been used from time to time. Pyrogenic silica is a very effective rheology modifier and is widely used as a rheology modifier in many systems such as Coating and paints [24].

6. **Enhanced oil recovery:** Polymer flooding is the most commonly used technique for Oil recovery. It is quite effective but expensive at the same time because it consumes extensive quantities of polymer. Emerging nanomaterials especially silica-based nanomaterials help to deal with this challenge. Addition of silica nanomaterials changes viscosity considerably and significantly improves oil recovery [25].

7. **Nanocomposites:** Recently, use of nanotechnology has created many new opportunities such as producing valuable inorganic-organic hybrid composites. Nano-sized inorganic filler such as silica can surprisingly modify properties of the composite materials; they can significantly enhance thermal properties and strength of materials and make them more usable to suit the operating environment. The crystalline form of silica nanoparticles has received a lot of interest recently for their application in nanocomposites because they have a very ordered structure, they have a very high surface area are relatively cheaper to produce [26].

8. **Reinforcement of elastomers:** The reinforcement of soft materials such as elastomers is done by blending them with rigid and hard materials and it has a lot of Industrial applications. Using fumed silica as a reinforcing filler in elastomers such as high-performance rubber products produces a considerable improvement in their mechanical properties as they can reap both the benefits by gaining stiffness of the reinforcing material and yet retaining the original elastic nature and properties [27].

9. **Fabrication of super hydrophobic surfaces:** Non-wettable surfaces which have high water contact angles (WCA's) and an easy sliding of water droplets coming into contact are called as super hydrophobic or ultra-hydrophobic surfaces [28]. For a surface to be super-hydrophobic, it requires certain conditions of chemical composition and surface topography [29]. Hydrophobically modified Silica can be used to prepare super hydrophobic coatings on glass which show self-cleaning properties and withstand its super hydrophobicity even after

multiple cycles of abrasion and adhesion. It can withstand its super hydrophobicity at different pH values and it works on any size and shape of glass [30].

10. **Recyclable gas storage:** Natural gas is a potential source of energy. Methane is the primary constituent of natural gas and is relatively green energy source as it produces less CO_2 as compared to fossil fuels. Methods currently in practice for transportation or storage of natural gas require compressing the gas to high pressures and then cooling it to a temperature less than 190.6 K which makes it very expensive. Gas hydrate is a promising candidate for storing natural gas in a cost-effective, extremely safe, non-explosive and environmentally friendly manner [32]. A recent investigation about the formation-dissociation cycle of methane gas hydrate in a silica-water suspension show high hydrate conversion and offers many other advantages over existing conventional methods. Therefore, use of silica in methane hydrate presents us with a viable platform for recyclable gas storage [33].

Chapter 2: Literature review

A suspension can be thought of as a heterogeneous fluid which contains solid particles well dispersed throughout the system and which are large enough to settle if left undisturbed. The solute particles do not dissolve in the medium and are suspended throughout the bulk of the solvent. The suspended particles may be seen under the microscope. Suspensions are unstable from the thermodynamic point of view. We see a lot of suspensions in daily life around us such as fog, smoke, dust, milk, blood etc. [34]. Several classifications are used in the literature to describe suspensions. Depending upon the nature of dispersion medium and the dispersed phase, suspensions can be classified into following types:

- **Aerosols**: Aerosols consist of solid or liquid particles in gases such as smoke (solid in gas) or fog (liquid in gas).
- **Bubbly liquids**: As the name suggests, they are liquids with the presence of bubbles in them such as effervescent liquids.
- **Emulsions:** Emulsions are a suspension of immiscible liquid droplets in a host liquid, such as milk.
- **Hydrosols:** They consist of solid particles in a host liquid such as paint pigments.

The size of particles in suspensions can vary from submicron to millimeter range [35]. Colloids, on the other hand, are the uniformly dispersed mixtures in which dispersed particles are smaller and they do not settle. Due to their small very particle size, surface area to volume ratio for colloids is very large. Colloids and suspensions are different from solutions in which dissolved substance does not exist as a solid because solvent and solute are mixed homogeneously [34]. The rheology of suspensions, their stability criterion, and their flow behavior and drag reduction have been elaborated subsequently.

2.1 Fundamentals of Rheology:

"Rheology is the science dealing with the deformation and flow of materials" [36]. It deals with how materials respond to the application of mechanical forces or to deformation or a combination of both. Various factors such as temperature, pressure, shear rate, duration of shear and pressure may affect the rheological properties of a material [37]. The field of rheology is dominated by an inquiry into the flow of complex fluids such as polymers, emulsions, slurries, and suspensions etc. The shear stress versus shear rate relationship of complex fluids is usually quite different than for

a Newtonian fluid, which describes the shear behavior for simple liquids. These fluids are generally very viscous, and their rheological properties are also of importance. Hence, the flow behavior of non-Newtonian fluids is a central part of rheology [38]. Consider a layer of fluid in motion between two large parallel plates. Both the plates have a surface area A and have a distance Y between them, as shown in figure 3 given below:
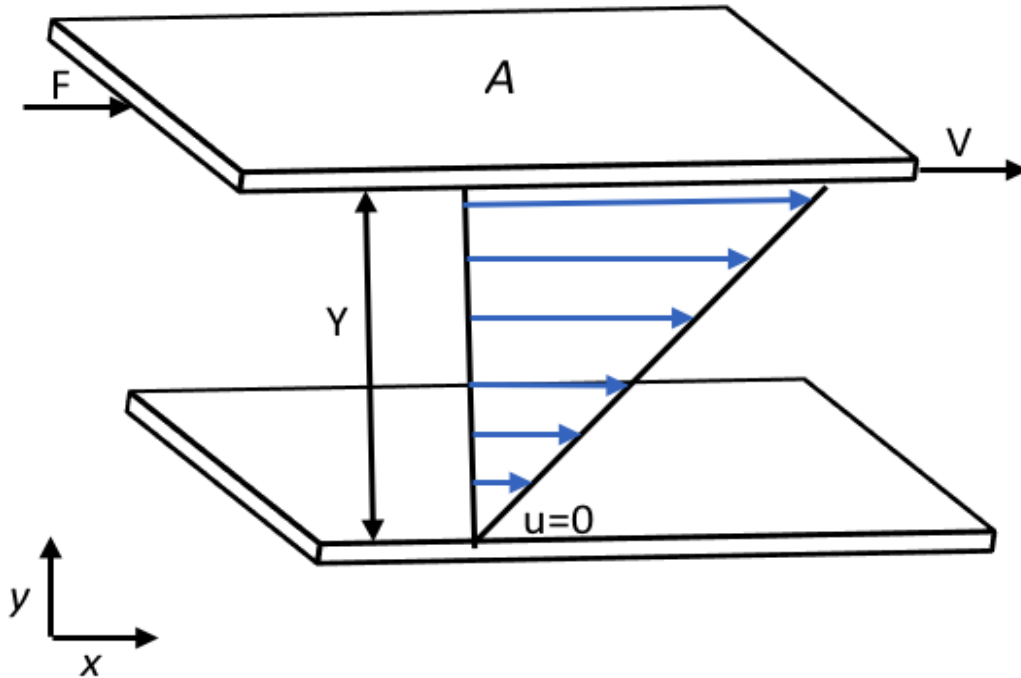
Figure 3: A graphical representation of one directional shear flow

The lower plate is stationary while the upper plate starts moving in the positive x-direction with a constant velocity "V". The fluid starts gaining some momentum and the moving plate will generate a motion in other layers of liquid as well. After some time, the system reaches a steady state situation. Once steady state is reached, the velocity of a layer of fluid just above the lower stationary plate will be zero whereas the layer of fluid just below the uppermost moving plate will move with the velocity same as the moving plate i.e. "V". Also, if we investigate the velocity profile between two plates, we will find that it increases linearly with the positive "y" axis from lower to the upper plate. We observe that a constant force "F" opposite is required to keep the upper plate in motion. This force required to maintain the motion of the upper plate per unit surface area of the plate "A" is called as shear stress and it is found to be directly proportional to the

velocity of the upper plate and also it bears an inversely proportional relationship with the distance "Y" between the two plates as:

$$\frac{F}{A} = Shear\ stress \propto \frac{V}{Y} = \mu\frac{V}{Y} \tag{2}$$

The proportionality constant μ in the above equation is a fluid property called as the dynamic viscosity of the fluid. As the velocity profile is linear, the Equation 2 can be written similarly for a very small segment fluid. So, the differential form of Equation 2 can be written as:

$$Shear\ stress = \tau_{y,x} = -\mu\frac{dV}{dy} \tag{3}$$

In Equation 3, we replace $\frac{F}{A}$ by the shear stress symbol $\tau_{y,x}$ i.e. a force acting in the -direction on a unit area normal to the "y" direction. The negative sign indicates that the shear stress acts opposite to the direction of motion on a faster-moving fluid. Equation 3, which states that the shear force per unit area is directly proportional to the negative of velocity gradient, is known as *Newton's law of viscosity*. The fluids which follow this law are known as *Newtonian fluids*. Polymeric liquids, slurries, and suspensions often do not follow this and are called as *non-Newtonian fluids*. We can also understand the same situation from the perspective of momentum transfer as:

The equation 2 for an incompressible fluid of density ρ can also be re-written as:

$$Shear\ stress = \tau_{y,x} = -\frac{\mu}{\rho}\frac{d}{dy}(\rho V_x) \tag{4}$$

The quantity "$\rho\ V_x$" can be looked at representing momentum per unit volume of fluid and therefore $\tau_{y,x}$ represents the transfer of x-direction momentum in the y-direction. The negative sign means that the transfer of momentum happens downhill w.r.t velocity i.e. in the direction of a fluid layer having a higher velocity to the lower velocity fluid layer. The velocity gradient serves as a driving force for momentum transport. Often the ratio of viscosity and density of a liquid is represented by a symbol as:

$$\nu = \frac{\mu}{\rho} \tag{5}$$

Where ν is known as *Kinematic viscosity* [39, 40].

2.2 Flow behavior of suspensions:

Viscosity is the most commonly sought after rheological quantity and it plays a significant role in flow behavior of any fluid. Viscosity is constant for Newtonian fluids at a given pressure and temperature and is independent of shear rate (γ) whereas when we talk about non-Newtonian fluids, viscosity depends and is specified at a given shear rate and is known as shear viscosity. The shear viscosity of a liquid is obtained by dividing its shear stress with shear rate and it depends on different factors such as flow geometry and forces acting on the fluid in the past other than shear rate. Because apparent viscosity depends on shear rate, it is generally known as shear viscosity [41]. In real life, viscosity depends a lot on pressure, temperature and on how long shear is applied. When subjected to shear rate, suspensions generally show two distinct types of non-Newtonian behavior explained as under.

2.2.1 Shear Thinning behavior:

Flow behavior of a lot of materials such as slurries, emulsions, and polymer solutions are different from a Newtonian fluid & follow shear thinning behavior. Shear thinning is a non-Newtonian behavior in which viscosity of a fluid decreases with an increase in shear rate. It is also sometimes referred to as pseudo-plastic behavior [42]. In polymeric solutions, it was observed that for very low shear rates, the apparent viscosity is almost independent of shear rate and tends to be constant called as *Zero shear viscosity* generally represented by"η_0"

$$\lim_{shear\ rate \to 0} \frac{Shear\ stress}{Shear\ rate} = \eta_0 \qquad (6)$$

Apparent viscosity also approaches a constant value at very high shear rates for polymer solutions; and that value is called as infinite shear viscosity, η_∞.

$$\lim_{shear\ rate \to \infty} \frac{Shear\ stress}{Shear\ rate} = \eta_\infty \qquad (7)$$

The strength of shear-thinning varies from one system to another. The minimum shear rate value beyond which any fluid starts showing shear-thinning behavior is known as critical shear rate value which depends on various factors like particle shape and size, polymer concentration, nature of solvent etc. [41]. The figure given below depicts the flow behavior for a typical shear-thinning fluid (log-log scale):
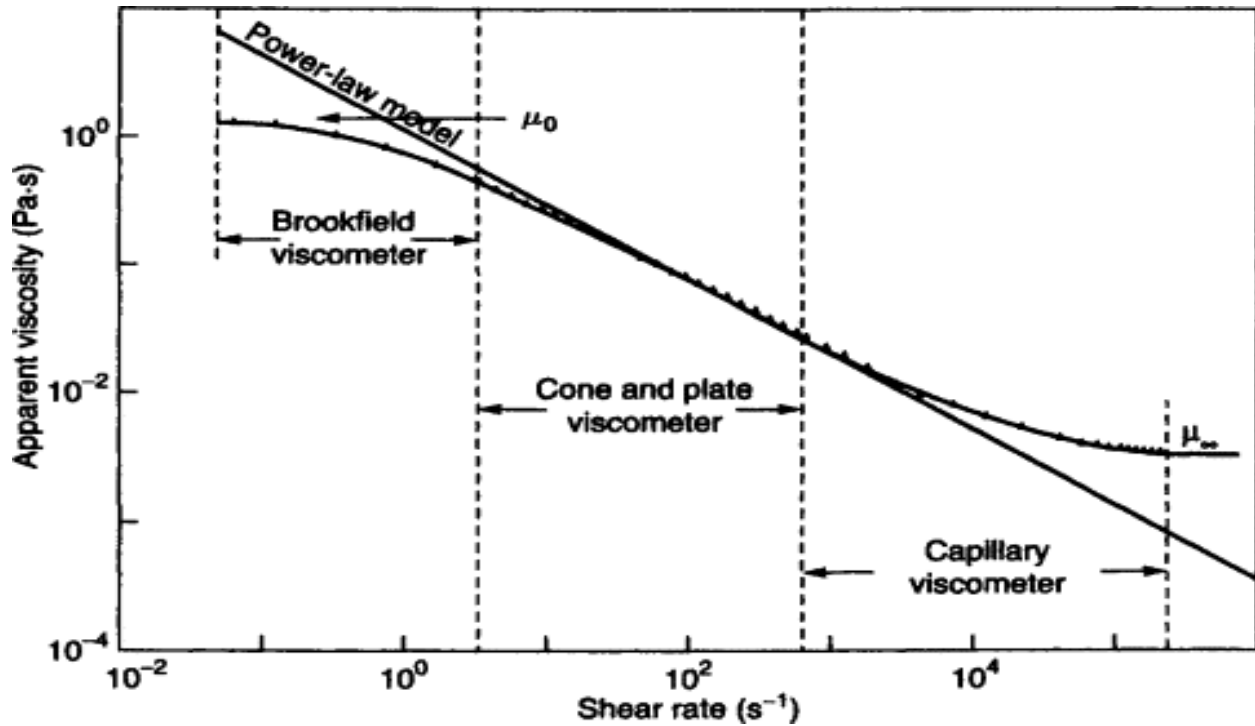
Figure 4: Flow behavior for a typical shear thinning fluid [43]

2.2.2 Shear thickening behavior:

The liquids for which the apparent viscosity increases with an increase in shear rate are known as Shear thickening fluids [44]. This happens due to increased flow resistance as shear rate increases. Generally, such behavior is found in concentrated suspensions at high shear rates whereas some suspensions also exhibit this kind of behavior even at lower shear rates. Some of the examples include concentrated suspensions of titanium oxide, china clay and cornstarch in water etc. There are a lot of explanations that have been given at times to explain the shear thickening behavior. A widely accepted explanation is that at high shear rates, the liquid is incapable of filling the void space and hence unable to lubricate and decrease frictional forces between particles which in turn, is seen as an increase in apparent viscosity [45]. The figure given below depicts the flow behavior of a shear-thickening fluid:
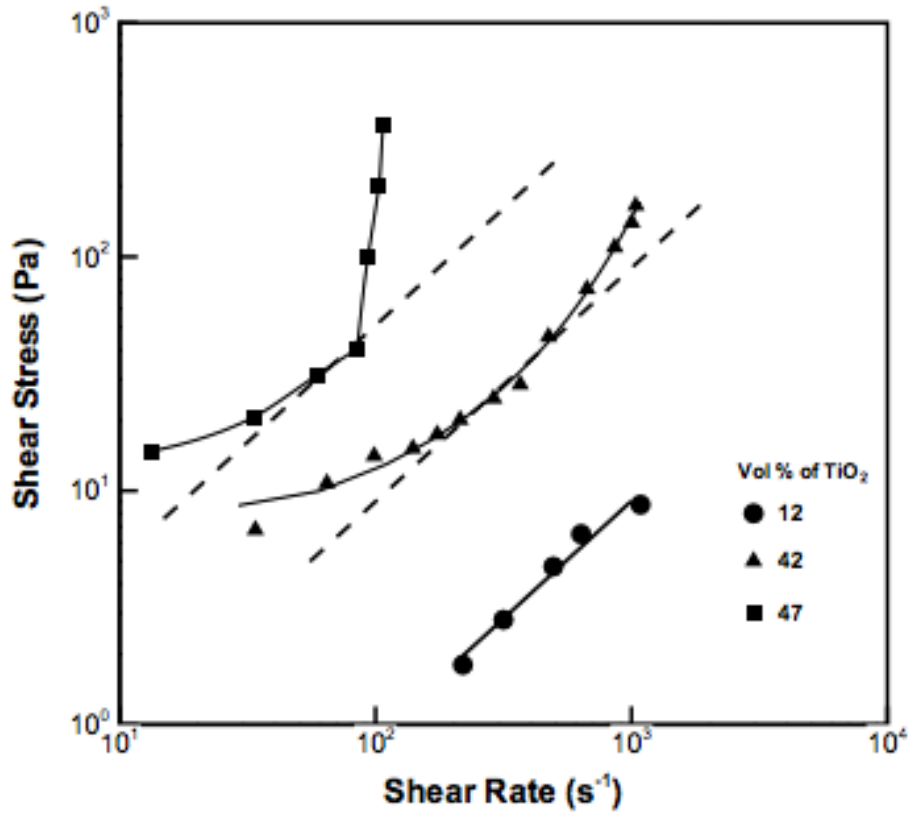
Figure 5: Flow behavior of TiO₂ suspensions at different particle concentrations [46]

To approximate the fluid behavior, various mathematical equations and models have been presented in literature from time to time. One of most popular model used is power law model which is explained as under:

Generally, the relation between shear rate (γ) and shear stress (τ) can be approximated by a power curve and can be written as:

$$\tau = m \, (\gamma)^n \qquad (8)$$

The above relation can be re-written in terms of apparent/shear viscosity and shear rate as:

$$\eta = m(\dot{\gamma})^{n-1} \qquad (9)$$

Where n and m are two empirical parameters called as power-law index and fluid consistency index respectively [47, 48].

Table 1: Power law index values for different fluid flow behavior

Value of n	Fluid behavior
n=1	Newtonian fluid
n<1	Shear-thinning fluid
n>1	Shear-thickening fluid

2.3 Stability of suspended particles: DLVO theory

The stability of suspended systems is important for its applications and various theories have been proposed from time to time to explain and predict particle stability. One of the most popular theory about colloidal stability is DLVO theory which is named after Landau, Derjaguin, Overbeck, and Verwey; the researchers who developed this theory. DLVO theory takes into account two major forces acting between charged particles in a liquid media i.e. Van der Wall forces and electrostatic forces. According to DLVO theory, the net interaction between charged particles may be assumed as an addition of Van der Waal and columbic interactions and both these interactions form the basis of colloidal stability. Both the Van der Waals and electrostatic forces are explained as under:

2.3.1 Van der Waals forces:

All the atoms, be it polar or non-polar in nature, have the presence of dipoles on them. Where polar molecules already have existing dipoles on them due to the difference in electronegativity of atoms on a molecule, even non-polar molecules form instantaneous diploes in an aqueous phase due to the interactions of the electrons surrounding an atom's nucleus. The attractive forces that result from the interaction between these dipoles are known as Van der Waals forces. There are two types of Van der Waals forces: London forces and dipole-dipole forces. Being the most common, London forces come into existence when electron cloud in a neutral atom experiences a momentary fluctuation. This fluctuation causes a dipole on the atom and which in turn induces a dipole in a neighboring atom or molecule. Oppositely charged surfaces of two dipoles attract each other. The presence of permanent dipoles in polar molecules like HCl can also induce temporary dipoles in neighboring molecules. Van der wall forces are weak and are additive in nature i.e. the total Van der Waal interaction of a system can be found by the summation of all the interactions among all the neighboring surfaces. They depend a lot on the geometry of the system. For two particles of spherical shape with Radius equal to R, the Van der Waals force F_A between them is approximated as:

$$F_A = \frac{H*R}{12*L^2} \tag{10}$$

Where H is called as Hamaker constant and L is the distance separating the particles. This expression holds true for a distance between particles to be relatively small w.r.t particle Radius I.e. L<<R. Hamaker constant depends on material properties such as density and polarizability. The presence of a medium also affects the value of Hamaker constant and an increase in Hamaker constant means the particles will have more attractive forces between them [49].

2.3.2 Electrostatic repulsion between particles:

The Van der Waals forces, being attractive in nature for two similar particles, tend to destabilize the suspension. The reason behind it is that if there were only forces of attraction amongst particles, they would have a tendency to aggregate and eventually precipitate. However, this does not happen as there is a presence of repulsive forces because particles in a medium like water, which has high dielectric constant, acquire some charge on them and start repelling each other. Repulsion is electrostatic in nature and is relatively a long-range force. Often, repulsive forces are high enough to negate the Van der Waals forces of attraction and hence stabilize the suspensions. There are two different mechanisms that can cause particles to acquire certain charge in a liquid medium that are:

1. Charged surface developed due to ionization or dissociation of the surface groups, leaving behind a charged surface.
2. Sometimes ions present in solution adsorb on uncharged surfaces and hence the particles acquire charge on them.

The system as a single unit is neutral, so medium should carry an equal charge of opposite sign. This opposite charge is carried by ions in the solution known as counter-ions. The counter-ions are present in solution in such a way that the particle has a distribution of them around itself in the form of layers known as a double layer. The double layer is made up of two sections; Inner part constitutes the ions that are adsorbed onto the particle surface due to chemical interactions whereas the outer part is formed by the ions loosely bound to the particle surface and which are free to move. [50]. The charge on a suspended particle can be measured by knowing the value of zeta potential, which is the potential observed at the shear plane between the colloid and liquid. A typical charge distribution surrounding a colloid is presented in the figure given below:
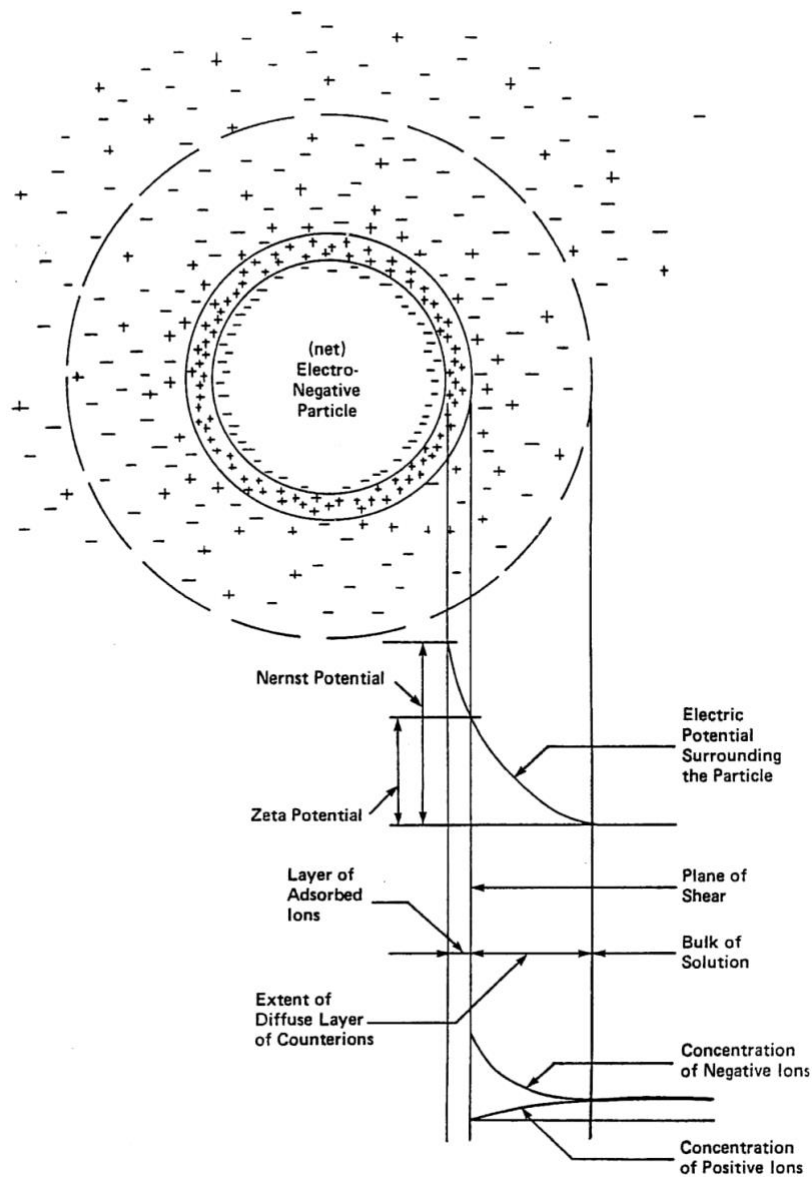
Figure 6: Electrostatic double layer around a particle [51]

The figure given above shows a colloid that acquires a net negative charge due to adsorption of negatively charged ions. As it gains a negative charge, now the particle attracts the positive ions in the solution to counterbalance its negative charge. Electrical potential happens to be maximum at the colloid surface and it keeps on decreasing as we move away from the particle to the bulk of the solution. The inner ions in the double layer can't move as they are tightly bound to the particle surface whereas ions in the other part of double layer i.e. diffuse layer are movable counter-ions.

The potential at the interface of both these layers is known as Zeta potential and the plane separating these two layers is called as shear plane [52]. The value of zeta potential gives us an information about the nature and magnitude of charge on the particle surface which determines the forces between the particles. A non-zero value of Zeta potential implies that the particles would have the presence of charge on their surface. There are some factors that affect the level of particle interaction and hence the value of zeta potential as well. The zeta potential, in general depends on the pH value and the concentration of ions in the medium explained in the sections given below.

2.3.3 Effect of pH:

The pH of the medium can dramatically affect the value of zeta potential. At low pH, zeta potential values tend to be positive in nature whereas in a highly basic medium the zeta potential values tend to be negative indicating negative charge on the particle surface. The increase in pH of the medium causes a decrease in zeta potential value till it becomes zero, for a pH value known as the Iso-electric point. As you increase pH value of medium beyond the Iso-electric point, particles acquire a negative charge and zeta potential value starts increasing on a negative scale. [20]. The reason for having a positive value of zeta potential at low pH values is because of the presence of a lot of H^+ ions at the particle's surface. However, this is not the case for all the materials [54].

2.3.4 Effect of Ionic strength:

When the concentration of ions in a medium is increased by providing ions which do not specifically interact with the surface of the particle, the double layer is compressed and that results in a higher attractive electrostatic force [53]. This in response, causes a decrease in the Zeta potential value and as the ionic strength increases, the Zeta potential value decreases and goes towards zero. However, if the ions can specifically adsorb on the particle surface, the magnitude and even the sign of charge and zeta potential on the particle can change. A presence of such ions can also bring out a change in IEP [54]. According to the DLVO theory, the overall interactions can be found by adding the attractive interactions and repulsive interactions, as shown under:

$$V_T = V_R + V_A \qquad\qquad (11)$$

Where the total Interaction energy V_T is equal to the sum of repulsive interaction energy, V_R due to the electrostatic forces and attractive interaction energy, V_A due to Van der Waals forces. Contrary to the electrostatic interactions, the van der Waals interaction energy does not depend on ionic strength or a change in pH of medium [50].

2.4 Rheology of fumed silica nanoparticle suspensions:

Suspensions have a widespread use in our daily life and are observed commonly as things like ketchup, pharmaceuticals such as a cough syrup, paints and even dust particles in the air. Suspensions are encountered in various stages of petroleum processing and recovery such as sludges in oil filed surface facilities, as drilling fluids and during production and transport [55].

The rheology of fumed silica nanoparticle suspensions has been a topic of continuous interest to researchers due to the widespread use of silica and potential applications that silica nanoparticles have to offer [17-26]. The suspensions prepared by the addition of hydrophilic fumed silica to polar liquids such as water and alcohols are stabilized due to the hydrogen bonding between the liquid molecules and surface silanol groups of particles for low and moderate particle concentrations (e.g. $\phi \leq = 0.15$). Whereas when it comes to hydrophobic fumed silica particles, they can stay well dispersed in organic solvents for a relatively higher particle concentration because of hydrophobic interactions between hydrophobic groups of modified silica particles and dispersing liquids. But, with an increase in particle concentration, the fumed silica suspensions change its state from sol to gel, whether hydrophilic or hydrophobic [63]. Gel formation occurs because attractive forces dominate over repulsive forces which makes aggregates of particle form clusters which grow in size and result in a 3-dimensional network of particles yielding a gel structure.

The rheological behavior of colloidal suspensions depends on a lot of parameters. The most important of them are the methods of preparation, shape, and size of the particle, particles volume fraction, temperature, surfactant concentration & properties of continuous phase [57-59]. It has been observed that fumed silica suspensions show a shear thinning behavior at low shear rates and show shear thickening behavior at high shear rates. So, their apparent viscosity decreases with an increase in shear rate upto a critical point and then starts increasing with a further increase in shear rate beyond this point [50-62]. Madhi H. Et al. reported that for silica suspensions in Poly Ethylene Glycol (PEG), the apparent viscosity vs shear rate plot of silica nanoparticle suspensions shows three different behaviors: shear thinning for low shear rates, following shear thickening transition for shear rates over critical shear rate till a point and then finally shear thinning behavior at very high shear rates [63, 64]. The shear thickening behavior of fumed silica nanoparticle suspensions can be attributed to the formation of hydro clusters, in which hydrodynamic lubrication forces

overcome inter-particle forces. This causes a formation of particle clusters that developsunder strong flows and therefore results in an increase in suspension viscosity [63, 65, and 66].

The apparent viscosity of fumed silica suspensions decreases with an elevation in temperature. Also, with an increase in temperature, critical shear rate increases whereas critical shear stress is independent of temperature. This is due to the increased Brownian motion of silica nanoparticles in suspension [63, 67]. The fumed silica suspensions are acidic in nature because they release H^+ ions in an aqueous phase and their natural pH ranges from 5.6-6.1 [68]. An increase in particle concentration makes the shear thickening effect become stronger and also the onset value of shear thickening behavior changes to a relatively low shear rate [62, 65]. The rheology of a suspension depends on factors like particle interaction, hydrodynamic interactions, and Brownian forces. There are various methods that can be used to tune the rheological behavior of suspensions such as introducing an electrolyte to control the concentration of ions in medium or changing the pH value. It was observed that an increase in salt concentration in medium increases the viscosity of suspensions at any pH value [63, 69].

Through various studies, the Iso-Electric Point of fumed silica suspensions is found to be approximately around pH=2. With an increase in pH, the zeta potential of silica suspensions is found to become increasingly negative and tend to be invariant for high pH values [67, 70, and 71]. For a very low electrolyte concentration such as salt concentration less than 0.01 M, there is no visible effect of electrolyte concentration on zeta potential or Iso-electric point. But a shift in Iso-electric point to relatively high pH value at higher electrolyte concentrations has been reported [69]. Keiko Y. Et al. observed that there was a suppression in the magnitude of zeta potential with electrolyte presence in suspension possibly due to the adsorption of counter-ion on double layer neutralizing some of the charge on particle surface [56].

The particle size of silica nanoparticles observed in suspension is larger than its primary particle size [67], potentially because silica nanoparticles undergo chain-like aggregation in aqueous phase [56, 64]. Even though the primary particle size of fumed silica particles is anywhere between 5-50 nm, the particles form stable aggregates in the suspensions in a size range of 100-500 nm due to the hydrogen bonding. There is not any appreciable effect of pH change observed on particle size for silica nanoparticles [67]. The particle size as reported by DLS increases with the concentration of the sample whereas it is not possible to measure the particle size for higher particle concentration due to the presence of multiple peaks in particle size distribution [10].

2.5 Fluid Flow and friction factor:

Fluid flow can be classified into two major regimes on the basis of the pattern in which fluid flows; Laminar or turbulent. The basic difference between these two types was demonstrated by Reynolds in 1883. He carried out an experiment in which he injected a stream of dye in flowing water in a small glass tube and the flow could be regulated by a valve at the outlet. At low flow rates, he observed that the stream of dye followed a well-defined straight-line path without any mixing of the dye with surrounding water. At very high flow rates, the dye started following an irregular motion and it spread randomly into the tube cross-section. This led to a classification of fluid flow in two major categories defined as under:

- **Laminar flow:** Laminar flow, also called as a streamline or viscous flow is the flow in which layers of fluid slide past each other in parallel layers with no visible mixing across the layers. Laminar flow can be observed at low flow rates.

- **Turbulent flow:** Turbulent flow can be described as a rapid and irregular movement of fluid with the presence of eddies. Properties such as velocity and pressure fluctuate a lot for each location in turbulent flow. Turbulent flow occurs beyond a certain flow rate known as critical flow rate [72].
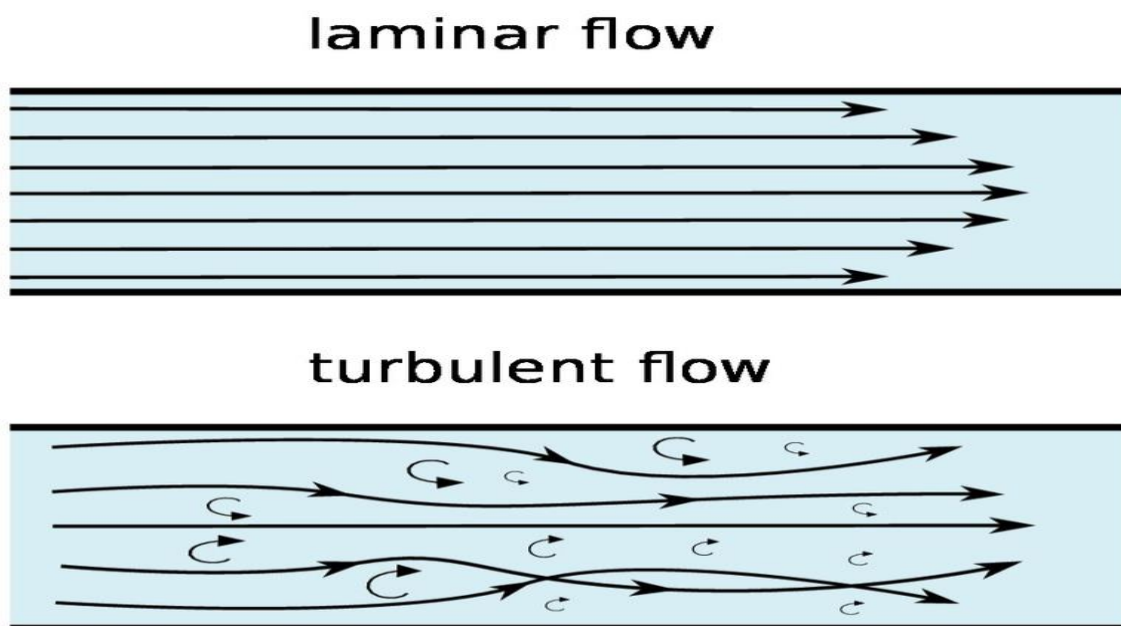
Figure 7: Laminar and turbulent flow in pipes [73]

2.5.1 Reynolds Number (Re):

Osborne Reynolds studies the flow conditions in which the flow of fluid in pipes transitioned from laminar to turbulent flow. He observed that the flow transition depends on the flow velocity, the kinematic viscosity of the fluid and the diameter of the tube. The higher the velocity, & the lesser the viscous the liquid, the more turbulent the flow is. He presented the connection between these quantities in a dimensionless number, called as Reynolds number Re [74]:

$$Re = \frac{\rho * V * D}{\mu} \qquad (12)$$

Where Re is the Reynolds Number, ρ is the fluid's density, D is the Diameter of the pipe, V is the velocity of the fluid, and μ is dynamic viscosity of the fluid. Reynolds number can be understood as a measurement of the ratio of inertial to viscous forces. Inertial forces involve force due to the momentum of the mass of a flowing fluid such as the fluid's resistance to any change in velocity i.e. its magnitude or direction. Whereas viscous forces deal with the friction between different layers of flowing liquid.

2.5.2 Fluid flow in Pipelines:

Fluid flow in circular pipes in commonly encountered in daily life such as the flow of hot and cold water to our homes or the transportation of oil and natural gas. When a fluid flowing at a constant velocity enters the section of a pipe, the layers of fluid next to the walls slow down gradually due to the friction. As a consequence, a boundary layer develops in which effect of fluid deceleration can be felt by the fluid. This boundary layer extends as the fluid flows further downstream and at a certain distance ahead of the entrance, it develops till the pipe center and covers the entire cross -section of the pipe. After this point, the flow conditions remain constant and the flow is called as *fully developed flow*. The flow type depends upon the Reynolds number. It has been found that for a smooth circular pipe, the flow is generally laminar for a value of Reynolds number less than 2000 and turbulent for values of Reynolds number greater than 4000 [75].
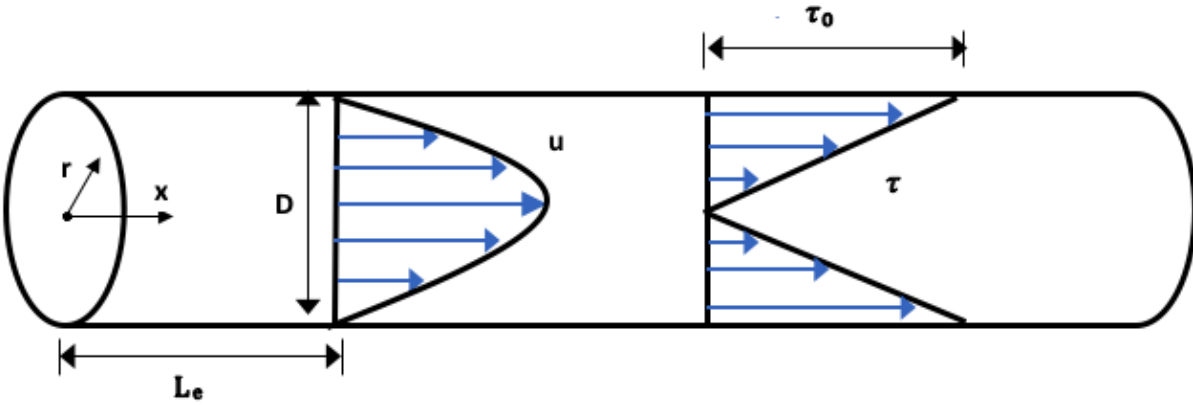
Figure 8: Laminar flow in a smooth circular pipe

The figure given above depicts the velocity distribution and shear stress distribution for a fully developed flow in a smooth circular pipe for laminar flow where D is the diameter of the pipe, L_e is the entrance length, u is the velocity distribution and τ is the shear stress distribution across the cross-section of the pipe. The distance from the entrance to just where boundary layer develops fully to the tube center is called as Entrance length, and is calculated from the relation as under [76]:

$$For\ Laminar\ flow \qquad L_e = 0.065\ (Re * D) \qquad (13)$$

$$For\ Turbulent\ flow \qquad L_e = 0.693\ (Re^{0.25} * D) \qquad (14)$$

The parabolic velocity profile given in the above figure for laminar flow is given by the equation:

$$u = u_{max} * \left(1 - \frac{r^2}{R^2}\right) \qquad (15)$$

where
$$u_{max} = \frac{R^2 * \Delta P}{4 * \mu * L} \qquad (16)$$

Where ΔP is the pressure drop across the entire length of the pipe, R is the radius of the pipe, μ is the dynamic viscosity of the liquid, L is the length of the pipe and u_{max} is the maximum velocity observed at the center of the pipe.

2.5.3 Friction factor & Pressure losses in a pipe:

Whenever a fluid flows in a closed pipe, there is a pressure drop in the flow direction. This pressure drop is due to various factors, majorly due to friction to the flow. So, there is a certain power requirement to maintain the flow. The pressure drop across a pipe of some length varies

proportionally with the flow rate for a laminar type flow whereas for a turbulent flow it increases more sharply as shown in the figure below [77]:
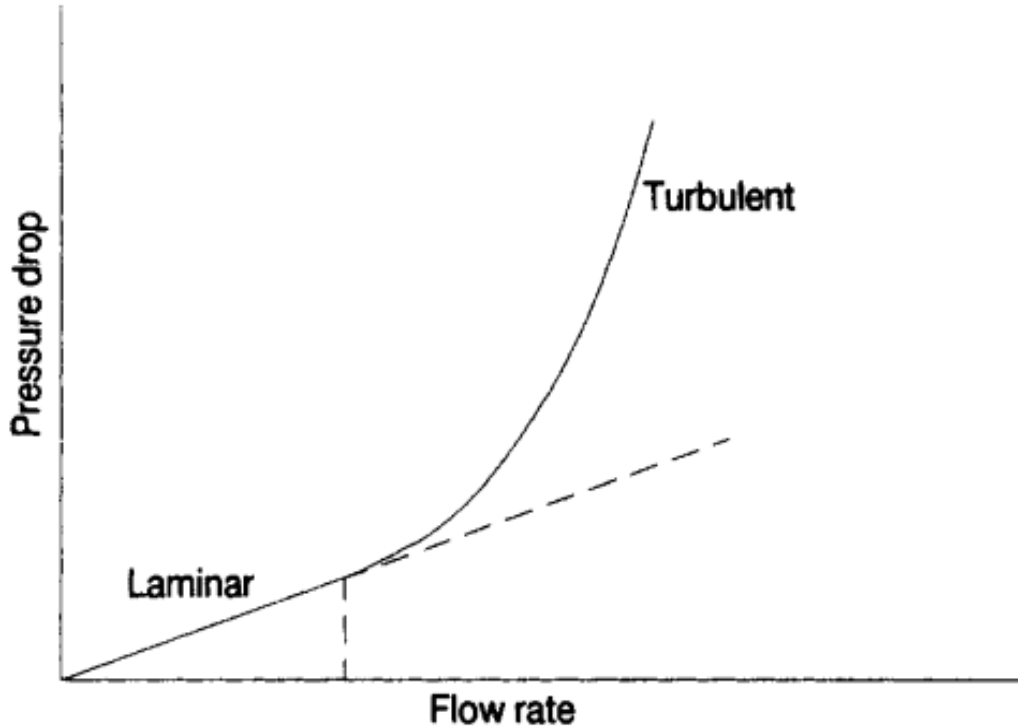
Figure 9: Pressure drop vs flow rate for a fluid flowing in a pipe [6]

As mentioned earlier, the major loss of energy in a pipe is due to the friction forces between the pipe walls and the fluid. This loss of energy is manifested in the form of pressure loss and can be related to the frictional forces present in the pipe. This friction is defined either in the terms of skin friction coefficient, also called as Fanning friction factor or Darcy's friction factor. The fanning friction factor, f is defined as the ratio of the wall shear stress to the product of the density and the velocity head as under [78]:

$$f = \frac{\tau_w}{\frac{\rho * V^2}{2}} \qquad (17)$$

Where V is the flow velocity (averaged) inside a pipeline, τ_w is the shear stress at wall surface and ρ is the density of the fluid. Also, the wall shear stress τ_w in a pipe can be related to the pressure drop due to the friction in a pipe as [77]:

$$\tau_w = \frac{\Delta P * D}{4L} \qquad (18)$$

Now if we substitute the value of wall shear stress from equation 18 in equation 17, we get:

$$f = \frac{\Delta P * D}{2 * L * \rho * V^2} \qquad (19)$$

Now average velocity of the fluid, V is related to the volumetric flow rate of the fluid, Q as:

$$V = \frac{Q}{A} \qquad (20)$$

Where A is the area of cross-section of the pipe and is calculated as:

$$A = \frac{1}{4}\pi D^2 \qquad (21)$$

After substituting the value of Velocity, V in terms of diameter, D and volumetric flow rate, Q, we get:

$$f = \frac{\pi^2 D^5 \Delta P}{32\ \rho L Q^2} \qquad (22)$$

So, knowing the fluid properties, pressure difference, and volumetric flow rate, we can easily calculate the value of friction factor. Also, Reynolds number can be written as:

$$Re = \frac{4\rho Q}{\pi \mu D} \qquad (23)$$

The equation 22 given above is valid for laminar as well as turbulent flow. The pressure drop for a Newtonian fluid in laminar flow in a pipe of a constant cross-sectional area is often given using Hagen-Poiseuille equation as [79]:

$$\Delta P = \frac{128\ \mu L Q}{\pi D^4} \qquad (24)$$

Substituting the value of Pressure drop from equation 24 in equation 22 and simplifying we get friction factor for fully developed laminar flow:

$$f = \frac{16}{Re} \qquad (25)$$

For fully developed Turbulent flow, friction factor doesn't only depend on the value of Reynolds number but also depends upon the value of relative roughness of the pipe wall i.e. $\in/D$. For a smooth pipe with negligible roughness, some empirical equations have been presented for a different range of Reynolds number to approximate the values of friction factor. Most popular of them is Blasius equation which is given as under [77]:

$$f = 0.079\ Re^{-0.25} \qquad (26)$$

Equation number 26 is only valid for a Reynolds number value from 3000 to 10^5. Some other empirical equations for friction factor in smooth pipes are:

Table 2: Empirical equations for calculating friction factor in fully developed turbulent flow

Researchers	Equation	Applicability
Von Karman, Prandtl, Kuradse [80,81]	$f^{-0.5} = 4.0 \, log(Re * f^{0.5}) - 0.40$	$3.1 \times 10^3 <$Re$< 3.2 \times 10^6$
Moody [82]	$f = \dfrac{0.184}{Re^{0.2}}$	$1 \times 10^4 <$Re$<1 \times 10^6$
Colebrook [83]	$f^{-0.5} = 1.8 \, log\left(\dfrac{Re}{6.9}\right)$	$3 \times 10^3 <$Re$< 1 \times 10^8$
Drew [77]	$f = 0.00140 + 0.125 \, Re^{-0.32}$	$3 \times 10^3 <$Re$< 3 \times 10^6$

For rough pipes, Colebrook equation is used to estimate the friction factor in turbulent flow for a value of Reynolds number above 4000 [84]:

$$f^{-0.5} = -2.0 \, log\left(\frac{\epsilon}{D} + \frac{2.51}{Re*\sqrt{f}}\right) \tag{27}$$

Another popular equation given by S.E. Haaland in 1983 is [8]:

$$f^{-0.5} = -3.6 \, log\left(\left(\frac{\frac{\epsilon}{D}}{3.7}\right)^{1.11} + \frac{6.9}{Re}\right) \tag{28}$$

2.6 Turbulent Drag reduction:

Drag reduction is the reduction in the pressure drop of the flow of a turbulent pipe at the same flow rate due to additives. In other words, as Lumley (1969) explained:

"*Drag reduction is the reduction of skin friction in turbulent flow below that of the solvent*".

As the definition implies, drag reduction is applicable to turbulent flows. It allows us to increase the pumping capacity or decrease the pumping requirement Drag reduction occurs with the addition of an additive if the pressure drop decreases at a constant flow rate or the flow rate increases at a constant pressure. It is generally calculated as:

$$\% \, D.R. = \frac{f_0 - f_s}{f_0} \times 100 \tag{29}$$

Where % D.R. is the percentage drag reduction, f_0 and f_s represent the friction factor of solvent and solution respectively. In terms of pressure drop, it is written as:

$$\% \, D.R. = \frac{P_0 - P_S}{P_0} \times 100 \qquad (30)$$

Where P_0 and P_s represent the Pressure drop in a given pipe length obtained for solvent and solution respectively. At first, the phenomenon of drag reduction was observed by Toms [85] in 1948 when he discovered that even a minute amount of long-chain polymer molecules if added to the aqueous phase, reduced the pressure drop in a turbulent pipe flow. Even small amounts of polymers had a dramatic effect in decreasing the pressure drop at the same flow rate. Because Toms discovered it, it is also sometimes referred to Tom's effect [85]. After he discovered it, extensive research was done to understand the mechanism and potential of drag reduction by various researchers. In 1964, Metzner and Park [86] investigated the turbulence flow characteristics of viscoelastic fluids and proposed that the turbulent-drag reduction by polymers is due to their viscoelastic properties. In 1969, Lumley [87] published a condense review about the drag reduction and its research finding till that time in the first volume of Annual Review of fluid mechanics. In 1975, Virk [88] published a review in which he described the fundamentals of drag reduction, presented some empirical equations along with physical explanations by mechanisms. In 1978, Zakin & Huntston [89] published results on a mechanical degradation of polymers in organic solvents. This was followed by a series of conference proceedings about drag reduction initiated by BHRA [85]. Drag reduction still continues to be a topic of interest and a subject of active research these days [90-93].

2.6.1 Drag reduction using nanoparticles:

Recently, the effect of nanoparticles alone or in combination with polymers or surfactants is being investigated for drag reduction characteristics. Nanofluids, for an instance, are a current topic of interest for research. Nanofluids are suspensions which have nanoparticles dispersed in a liquid phase such as water or oil by surfactants or Ultra-sonication. Nanoparticles, because of their unique properties and surface chemistry can be potential candidates for usage as drag reducing additives. Some of the research carried out recently in this area is listed below:

Dai X. and Liu H. used TiO_2-Polyolefin nanocomposite for drag reduction. Polyolefin is conventionally used as a drag reducing additive in oil pipelines. It was observed that its use as a drag reducing additive in turbulent flows has some limitations i.e. it gets mechanically degraded

at high shear rates. Under high shear rates, its long polymer chains would break and lose their drag reducing properties. It was observed that a surface modified TiO_2 with organic chains along with Polyolefin shows improved drag reduction properties and more resistance to shear degradation. The TiO_2 nanoparticles used were modified with a Silane-coupling agent and then used to create the nanocomposite [94].

Yanuar, Sealtial M., Kurniawan T.W., Okky A.P. and Rifqi H. discovered the drag reduction characteristics of alumina (Al_2O_3) Nanofluid by using a spiral pipe setup in turbulent flow conditions. Alumina nanoparticles were dispersed in water at different concentrations with different mixing times. It was observed that the long mixing time and an increase in nanoparticle concentration both had an increasing effect on the drag reduction capabilities. Also, the spiral pipe provides better results than a circular pipe under the same conditions. A maximum of 38 % drag reduction was observed at a Reynold number value of 20,000 with a concentration of 300 ppm of nanoparticles and a mixing time of 120 minutes [95].

Adam S., Ilker S.B., and Eric L. observed the drag reducing characteristics of Carbon Nano-tube (CNT) additives. They found that though CNT additives alone do not show any drag reducing performance but when coupled with polymers, they enhance the polymer's drag reduction performance. A 55 to 45 wt. % water-glycerine solution was used as a baseline fluid and the polymer used was (PEO) Polyethylene glycol. It was observed that a 100-ppm concentration of CNT's mixed with 300-ppm PEO solution improved the drag reduction performance as compared to what could have been achieved using PEO alone. It was also observed that CNT additives do not produce any substantial drag reduction with degraded PEO polymer [96].

Pouranfard A.R., Mowla D. & Esmaeilzadeh F. had an experimental study on drag reduction properties of nano-SiO_2 particles in a slug flow of water and air in horizontal pipeline flow. They also discovered that drag reduction performance was better for a pipe of smaller diameter than performance for larger diameter pipe. They prepared homogeneous suspensions by dispersing the silica nanoparticles into a solution of a surfactant prepared in a base fluid. These suspensions with different concentration of silica nanoparticles were used as Nano-fluids for drag reduction studies. The surfactant used in study was Sodium dodecyl sulfate (SDS). The results show that the amount of drag reduction increases with the increase in Nanofluid concentration up to a critical concentration value (0.75 %) after which there is no increment in the performance of drag reduction. Also, the injection of nanoparticles increased the performance of the surfactant

significantly with maximum drag reduction achieved equal to 66.8 % for 0.75 % mass concentration of silica [97].

Drzazga M., Gierczycki A., Grzegorz D. & Marcin L. investigated the impact of non-ionic surfactant on drag reduction effect of metal oxide in water Nanofluid. They prepared the Cu (II) oxide Nanofluid and used Tri-ammonium citrate to stabilize the Nanosuspension. Two different non-ionic surfactants were used i.e. Rokanol K7 and Rokacet O7 for investigation. The results obtained show that the Rockacet O7 surfactant with Nanofluid shows better drag reduction performance at low Reynolds number but shows very less drag reduction at low Reynolds number. On the other hand, Rockanol K7 show better drag reduction at higher Reynolds number. Overall, the Nano Fluid-Surfactant combination shows less friction factor hence better drag reduction performance than pure Nano fluid alone [98].

Another experiment was done by Yanuar, Talahatu M.A., Mau S., Waskito K.T. and Wulandari W. on the drag reducing characteristics of Calcium carbonate i.e. $CaCO_3$. The working fluid was prepared by mixing the Nanoparticle in water at different concentrations and then circulated into a spiral and a circular pipe. The highest drag reduction observed was 35 % at a Reynolds number value equal to 40000 for a 500-ppm concentration for the spiral pipe whereas the circular pipe experienced a maximum of 26 % drag reduction. Thus $CaCO_3$, an inexpensive and an environmentally friendly material is a potential additive for drag reduction applications [99].

Budi K., Samsul K., Suhanan and Yanuar conducted experiments to investigate drag reduction performance of Titania TiO_2 Nanofluids in a circular pipe using three base fluids i.e. distilled water, ethylene glycol-distilled water and propylene glycol-distilled water mixture. The TiO_2-distilled water system showed a shear thinning behavior. The results show that friction factor values obtained for TiO_2/distilled water combination were less than friction factor for water in turbulent flow regime indicating that the TiO_2-distilled water combination has drag reduction characteristics [100].

Chapter 3: Materials and methods

3.1 Materials:

The experimental grade silica nanoparticles were provided by Wacker Chemicals Pvt. Ltd. Three different types of silica particles i.e. HDK N20, HDK T30 and HDK S13 were used for the study. All three grades of silica particles used for the study were hydrophilic in nature. Hydrochloric acid and Sodium hydroxide were obtained from Sigma-Aldrich Co. LLC.

3.2 Preparation of silica nanoparticle suspensions:

For preparing suspensions of a particular concentration, the calculated amount of nanoparticles was weighed and added to 500 ml water. For suspensions that required an electrolyte presence, the required amount in ml of the 1M stock solution of NaCl was added to maintain 0.1 M NaCl concentration. The mixture was then homogenized at room temperature (~22 °C) initial temperature with a homogenizer (GIFFORD WOOD, model 1L). After adding the nanoparticles, the mixing was carried out for at least 40 minutes or more if required to make a stable suspension. While mixing, the temperature of the suspension could rise due to the friction between the agitator shaft and the suspension. For maintaining a pH value of 4 or 7, small quantities of dilute stock solutions of NaOH or HCl were added to the suspensions. Whereas for maintaining very low pH values i.e. 1 or 2, a few drops of concentrated HCl stock solution were added instead of dilute HCl stock solution to avoid unnecessary dilution of suspensions.

3.3 Viscosity measurements of dilute silica nanoparticle suspensions:

For a dilute suspension with particles that are non-interacting and are of spherical shape, the relative viscosity of the suspension can be related to the volume fraction of particles using Einstein equation as [101]:

$$\eta_r = 1 + B\phi \tag{31}$$

where η_r is the relative viscosity of the suspension which is the ratio of the viscosity observed by suspension to the viscosity of the continuous phase (medium), φ being the volume fraction of the particles i.e. a ratio of volume occupied by the particles to the total volume of the suspension and B is called as "Einstein coefficient" with a value equal to 2.5 for hard spheres. The relative viscosity of low concentration silica nanoparticle suspensions was measured by using CANNON® Ubbelohde viscometer at a room temperature of 22 °C.

3.4 Rheological measurements & flow behavior:

The entire experimental work was divided into two parts; Bench-scale experiments and Pipeline flow studies:

3.4.1 Bench-scale experiments & equipment:

Bench-scale experiments were done to investigate the rheological behavior of the suspensions. After the preparation, suspensions were maintained at the desired pH values. The effect of temperature and change in shear rate was investigated for different particle concentration samples of suspensions using Fann and Haake viscometers. The particle size measurements were performed using ''Dynamic Light Scattering'' method using DLS Zetasizer Nano zs90 manufactured by Malvern Instruments Ltd. The version of software used for measurements was Zetasizer 6.20. The samples were tested in ZEN0112, low volume disposable sizing cuvette at the standard 25 °C temperature with an equilibration time of 120 seconds for the sample analysis. There was no delay between different measurements. Also, the Zeta potential measurements were done with the same instrument using an electrode cuvette. Some of the equipment used for Bench-scale studies are:

1. **Fann Viscometer:** The shear viscosity of concentrated suspensions was measured using Fann viscometer model no. 35A which is a coaxial cylindrical viscometer. When the outer cylinder of Fann viscometer is rotated at a known velocity, it exerts a drag force on the fluid contained between both cylinders. This effect can be felt as torque on the bob which can be measured and is deflected as a Dial reading. The dial reading can be related to shear stress and hence viscosity can be measured as the shear rate is known for a given rpm. The shear rate could be increased up to 1020 s^{-1}. Further information about calibration and equipment specification can be found in Appendix A and B respectively.

2. **Haake Viscometer:** For experiments at elevated temperatures, the shear viscosity was measured using Haake viscometer Rotovisco® RV 12 which is a coaxial type cylindrical viscometer. A fluid of unknown viscosity is placed between the cylindrical annular space. The inner cylinder is a bob that rotates at a set speed, which can be controlled by changing the rpm. The inner rotating cylinder imparts momentum to the adjacent fluid and the flow resistance of the fluid can be estimated using the torque experienced by it. The torque required to keep the bob running is proportional to the viscosity and hence the information required on viscosity, shear rate and shear stress can be calculated using the magnitude of the torque, the set speed and the geometry of the bob. The results are displayed digitally. The viscometer is equipped

with an inline temperature measurement and control system, so shear viscosity of suspensions can be measured at different operating temperatures. The shear rate could be varied as high up to approximately 1198 s^{-1} which correspond to an rpm value of 512. The viscometer is equipped with different bobs and the system used for measurements was MV I. Further information about calibration and equipment specification can be found in Appendix A and B respectively. The figure given below presents the Haake viscometer used for measurements:

Figure 10: The Haake coaxial viscometer setup.

3. **PH meter:** All the pH measurements of nanoparticle suspensions were done by the Fisher Scientific accumet AE150 pH Benchtop meter. The pH meter is equipped with pH electrode and temperature electrode to measure pH and temperature readings respectively. The newly installed pH meter measures a reading as precisely as 0.01 units for pH and 0.1 ℃ for temperature. It measures the voltage and converts it into a pH value that is displayed on the system. To measure the pH value, the electrode sensor has to be dipped in tot the solution. To electrode has to be kept vertically straight while doing measurements. For this reason, the

system has been equipped with an electrode arm to keep electrode straight while taking measurements. The figure given below shows the pH meter setup:

Figure 11: The digital Fisher scientific accumet AE 150 pH meter

3.4.2 Pipeline flow behavior of silica nanoparticle suspensions:

The experiments were performed in a pipeline flow loop setup. Figure 12 is a graphical representation of the system used to observe the pipeline flow behavior whereas Figure 13 includes some pictures of some sections of the experimental setup.

A concentrated suspension 18 percent by wt. of silica S13 nanoparticles was prepared in the lab and then was diluted in the large mixing tank to achieve the desired concentration for flow loop studies. The mixing tank has a jacket and a thermal controller for temperature maintenance during experiments. The tank has been provided with a powerful agitator which runs on a motor. For pumping and circulating the fluid in the flow loop, the system is equipped with two centrifugal

pumps. The flow data was collected from three pipes of different nominal diameters i.e. 0.5-inch, 1-inch, and 1.5-inch. The test section for all the three pipes was chosen such that it would accommodate the entrance length and so that the pressure taps would measure pressure for a fully developed fluid flow. The test section of the pipes is connected to a pressure transducer system that can measure pressure drop of the flowing liquid over a certain length. The pressure transducer system is flexible and is configured in such a manner that the pressure drop for the test section can be measured by the transducer by connecting to the respective taps for the test section. The whole setup is equipped with a data acquisition system which displays pressure variations and readings on the attached computer (Figure 13c) with the help of the LABVIEW software.
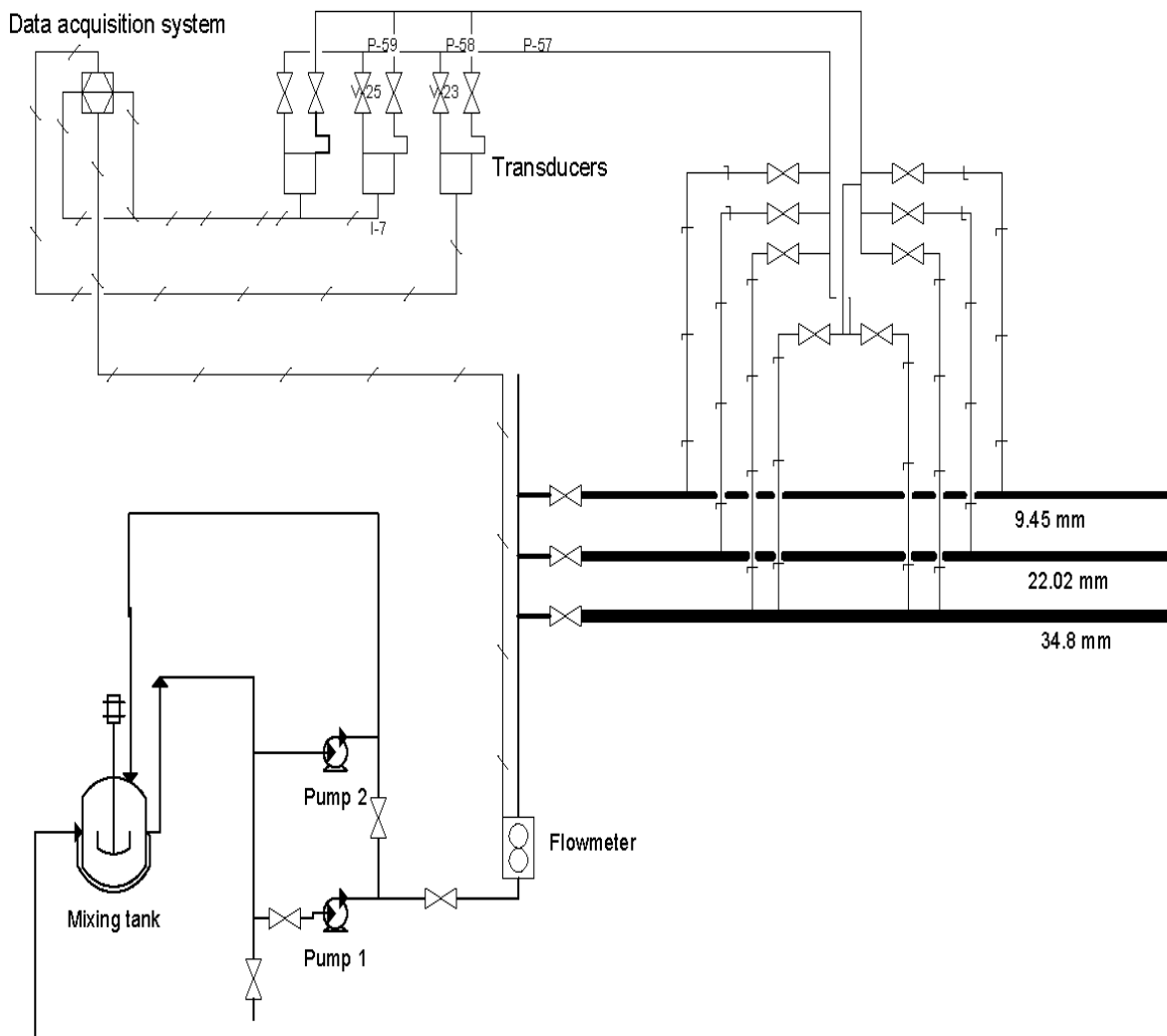
Figure 12: Schematic diagram of the experimental setup for flow loop measurements [102]

Figure 13: Different sections of the pipeline flow loop system (a) Control panel; (b) Different diameter pipelines; (c) Computer terminal of data acquisition system; (d) Mixing tank

As shown in the above picture, the flow loop is equipped with three horizontal pipes of different diameters and the table given below provides information about their dimensions and tapping locations:

Table 3: Important information about the flow loop pipelines.

Pipeline number	Nominal diameter (inch)	Inside diameter (mm)	Entrance length (mm)	Test section length (m)
1	0.5	9.45	91.44	1.219
2	1	22.02	154.2	3.048
3	1.5	34.8	154.2	3.048

Also, the system is equipped with three pressure transducers. The pressure transducers are set up in such a way that they can be connected independently to the pipeline in use and to the tapping locations we want to measure the pressure drop across. This could be achieved easily by opening the valves that are connected to the respective tapping locations without disturbing the whole system. The pressure transducers were calibrated by Dr. Ali Mohsenipour [102] during installation of the pipeline flow loop system. The calibration equation for each pressure transducer relates the digital voltage readings and the pressure drop observed by the transducer as given below:

Table 4: Calibration equations for pressure transducer system [102]

Transducer No.	Corresponding voltage Reading (mV)	Measurement Range (psi)	Calibration equation for pressure drop (psi)
1	V_2	0-0.5	$\Delta P = 0.1221 * V_2 - 0.102$
2	V_3	0-5.0	$\Delta P = 1.2581 * V_3 - 1.2823$
3	V_0	0-10	$\Delta P = 2.5297 * V_2 - 2.5573$

3.4.2.1 Calibration of the flow meter and pipeline test section:

The flow rate is measured by a Coriolis digital flowmeter which is installed in the flow loop system. To calibrate the flowmeter, the average flow rate of liquid passing through the flow meter was measured by manually weighing the collected water in a certain time. These flow rate readings were then plotted on a vertical axis with the corresponding voltage readings on a horizontal axis to get the calibration curve. Figure 14 shows the calibration equation obtained by plotting flow rate vs voltage as shown below:
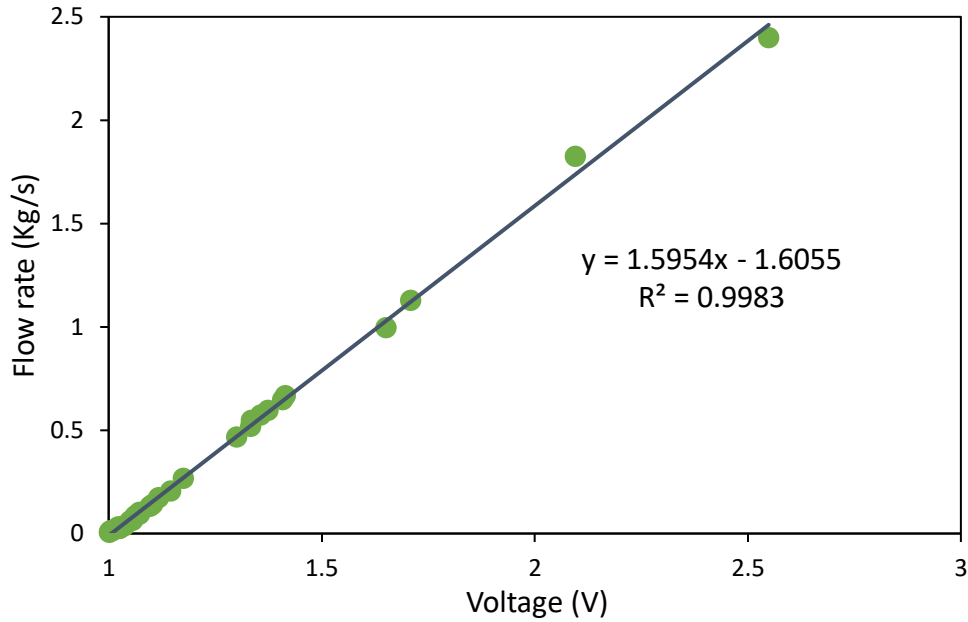
Figure 14: Calibration curve for Coriolis flow meter

As shown in the figure above, the calibration equation obtained is:

$$y = 1.5954\,x - 1.6055 \qquad (32)$$

The pipeline test section was also calibrated using water before doing any experiments. The voltage readings were obtained for different flow rates of water in pipelines. These voltage readings can be used to obtain the pressure drop. So, the voltage readings were converted to corresponding pressure drop values using equations given in table 4 above. Also, the voltage readings can be used to estimate the flow rate from the calibration equation of Coriolis flowmeter i.e. equation number 32. Then, this data was used to plot friction factor vs Reynolds number in the pipes and was compared with the Blasius equation for flow in smooth pipes. Figure 15 shows a comparison between experimental data obtained for water and the Blasius equation for 1-inch nominal diameter pipe. The Blasius equation for calculating friction factor for a given Reynolds number for a Newtonian fluid flow in a smooth pipe is:

$$f = \frac{0.079}{Re^{0.25}} \qquad (33)$$
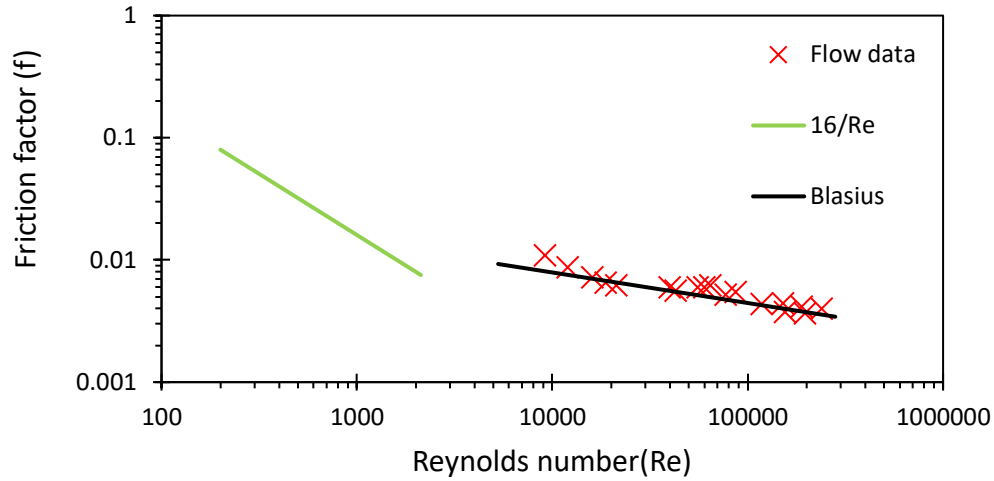
Figure 15: Comparison between Blasius equation and experimental results from the pipeline flow of water in a 1-inch pipe

As it can be observed from the figure given above, the pipeline flow results for water are in a nice agreement with the Blasius equation. In this research, the water line was used as a reference line for comparison of friction factor of suspensions. Other information about calibration of flow loop & pipeline test section is available in Appendix A.

Chapter 4: Results and Discussion

The various results obtained for particle size distribution, zeta potential, the relative viscosity for dilute suspensions, the shear viscosity for concentrated suspensions, effect of temperature, pH and presence of electrolyte on rheology are explained as under:

4.1 Size distribution of different grades of silica nanoparticles:

The size distribution of silica nanoparticles for different particle concentrations was analyzed by Zetasizer Nano zs90 using Dynamic Light Scattering method. Figure 16 summarizes the Intensity distribution peaks observed and Figure 17 summarizes the Number distribution peaks observed for three grades of silica nanoparticles i.e. HDK S13, T30 and N20, all hydrophilic in nature. It was observed that with an increase in particle concentration, peaks move toward the higher particle size which indicates that the increase in particle concentration leads to the formation of bigger aggregates in suspension.
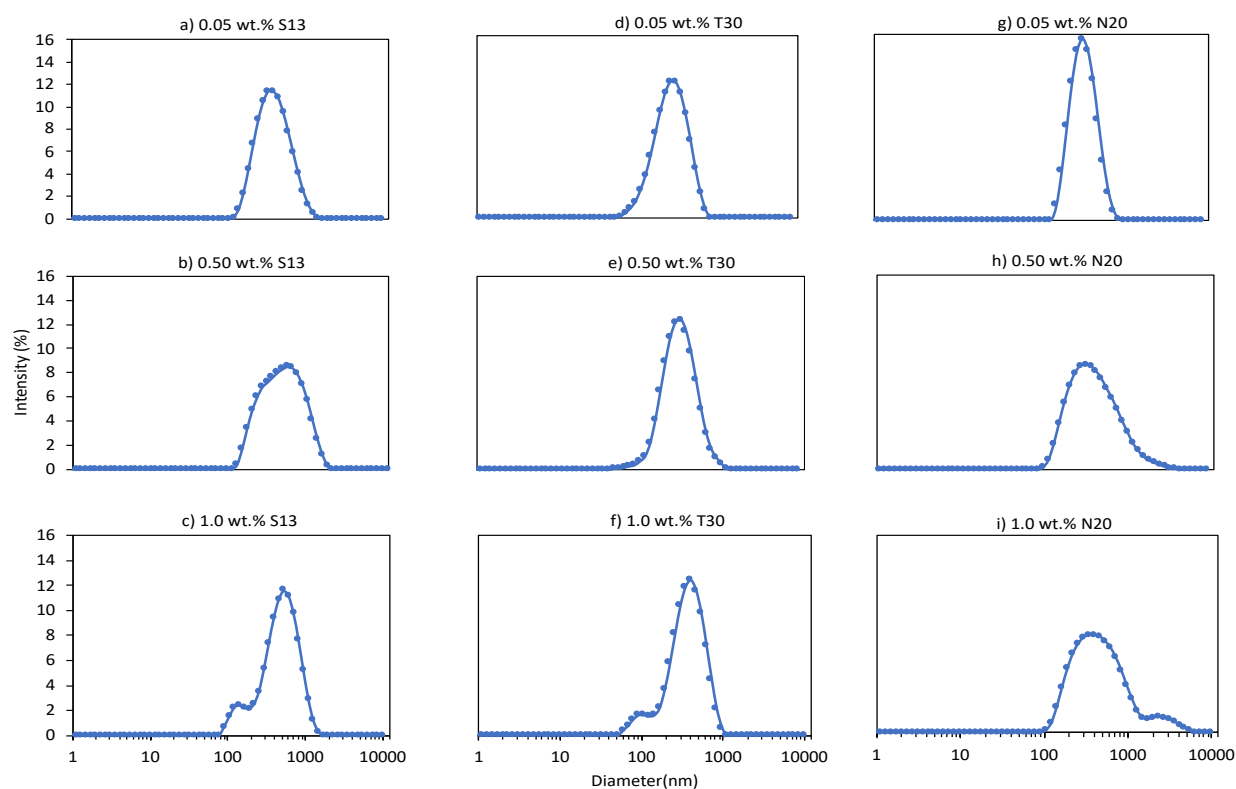
Figure 16: Size distribution plots (Intensity %) of S13, T30, and N20 silica nanoparticles
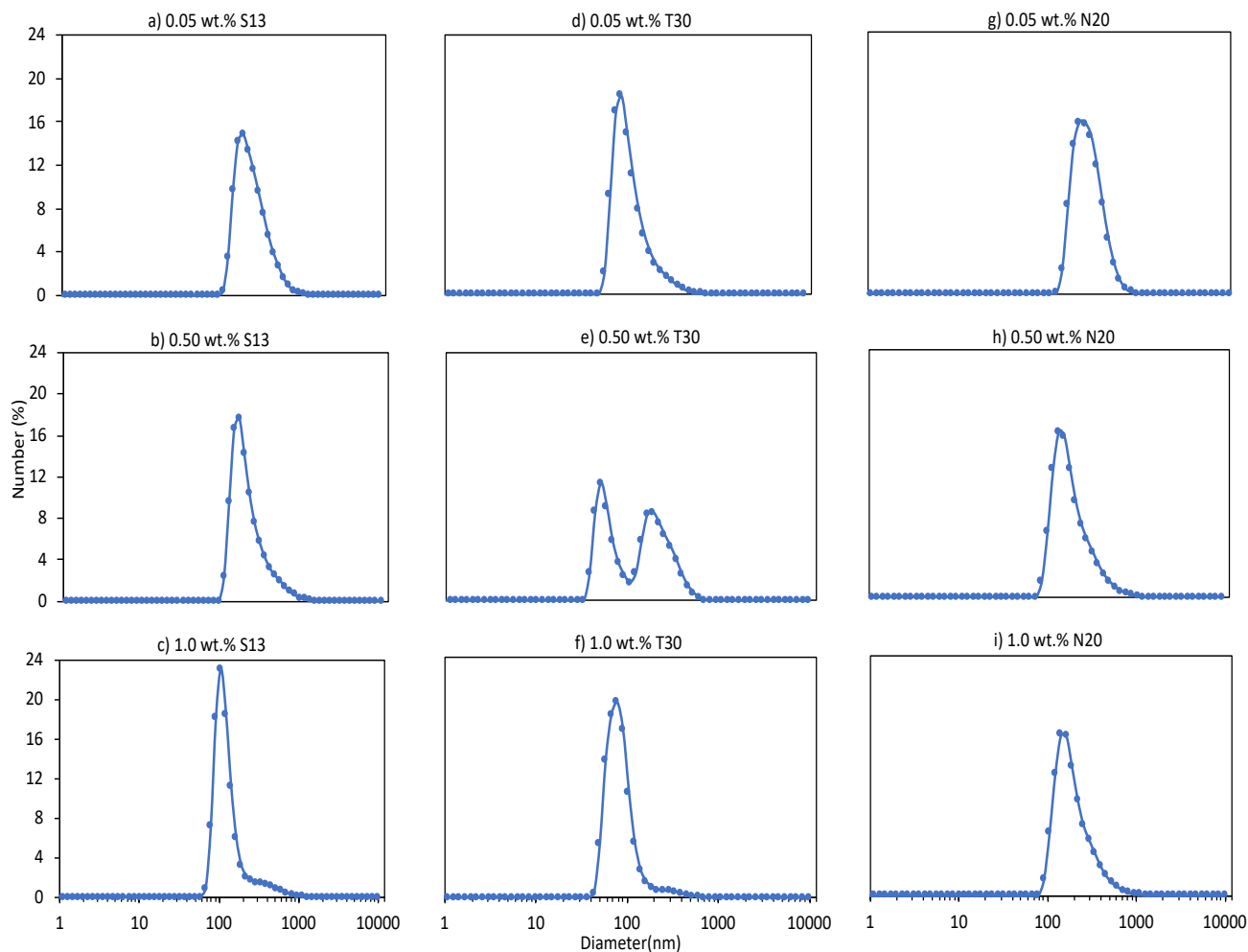
Figure 17: Size distribution plots (Number %) of S13, T30, and N20 silica nanoparticles

4.1.1 Effect of pH on Size distribution:

To observe the effect of pH, samples were maintained at different pH values and were analyzed for particle size distribution using Dynamic Light Scattering method. These experiments were done for dilute samples i.e. for 0.50, 0.75 and 1 wt. % particle concentrations. Figure 18 shows the results obtained for these experiments. Though results show slightly higher peak values at low pH, there is no specific pattern observed with respect to the pH of the suspensions for all samples.
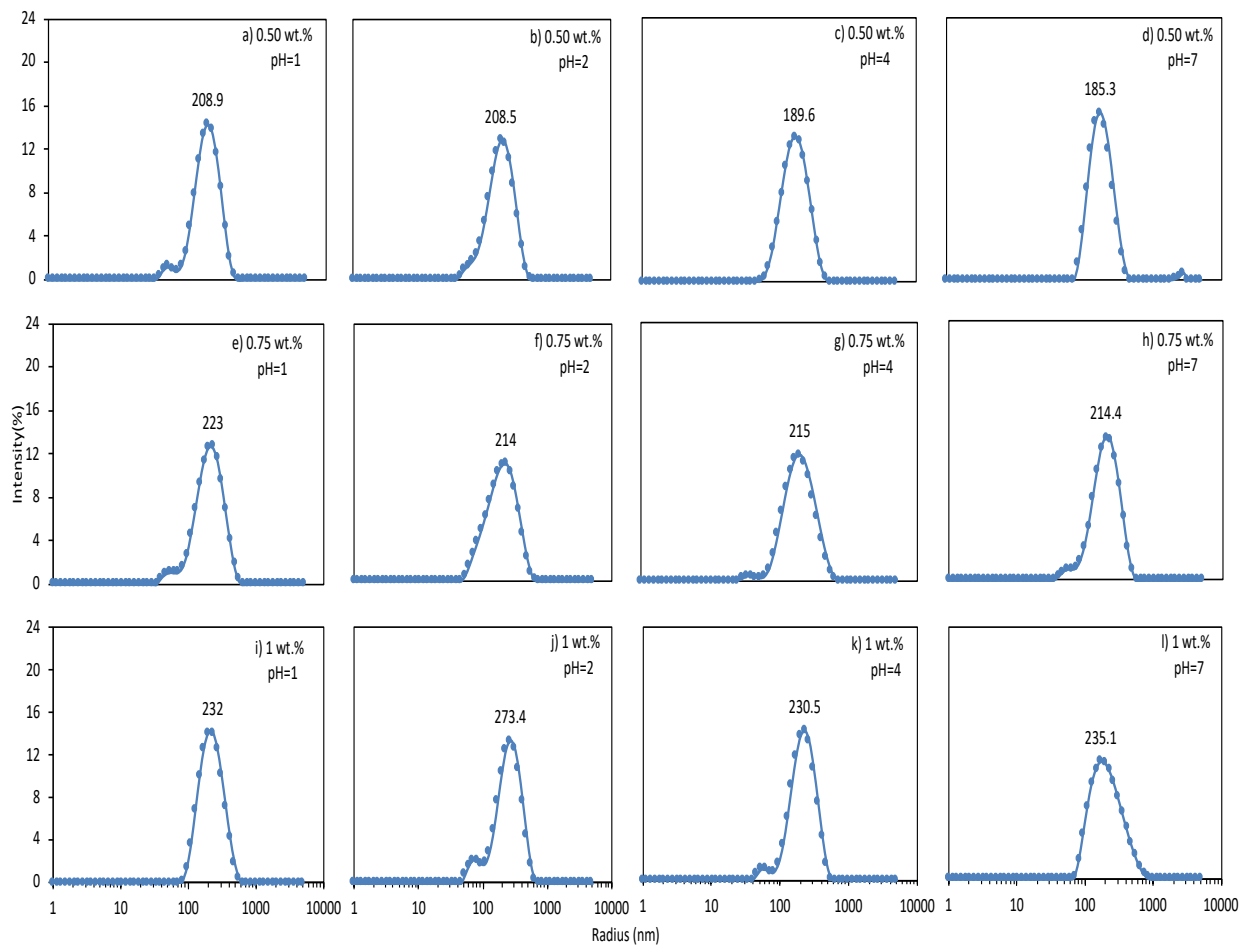
Figure 18: Size distribution plots (Intensity %) of S13 silica nanoparticles at different pH values

4.1.2 Effect of Electrolyte addition on Size distribution:

To investigate the effect of electrolyte presence on size distribution, suspensions were prepared at different pH values in the presence of 0.1 M NaCl. The results from Dynamic Light Scattering show that on the addition of electrolyte at the given concentration, the size of aggregates in the suspensions increases. This can also be seen in the figure given below; the peaks obtained for the samples with electrolyte presence move toward a higher particle size irrespective of the pH value or the particle concentration of the sample.
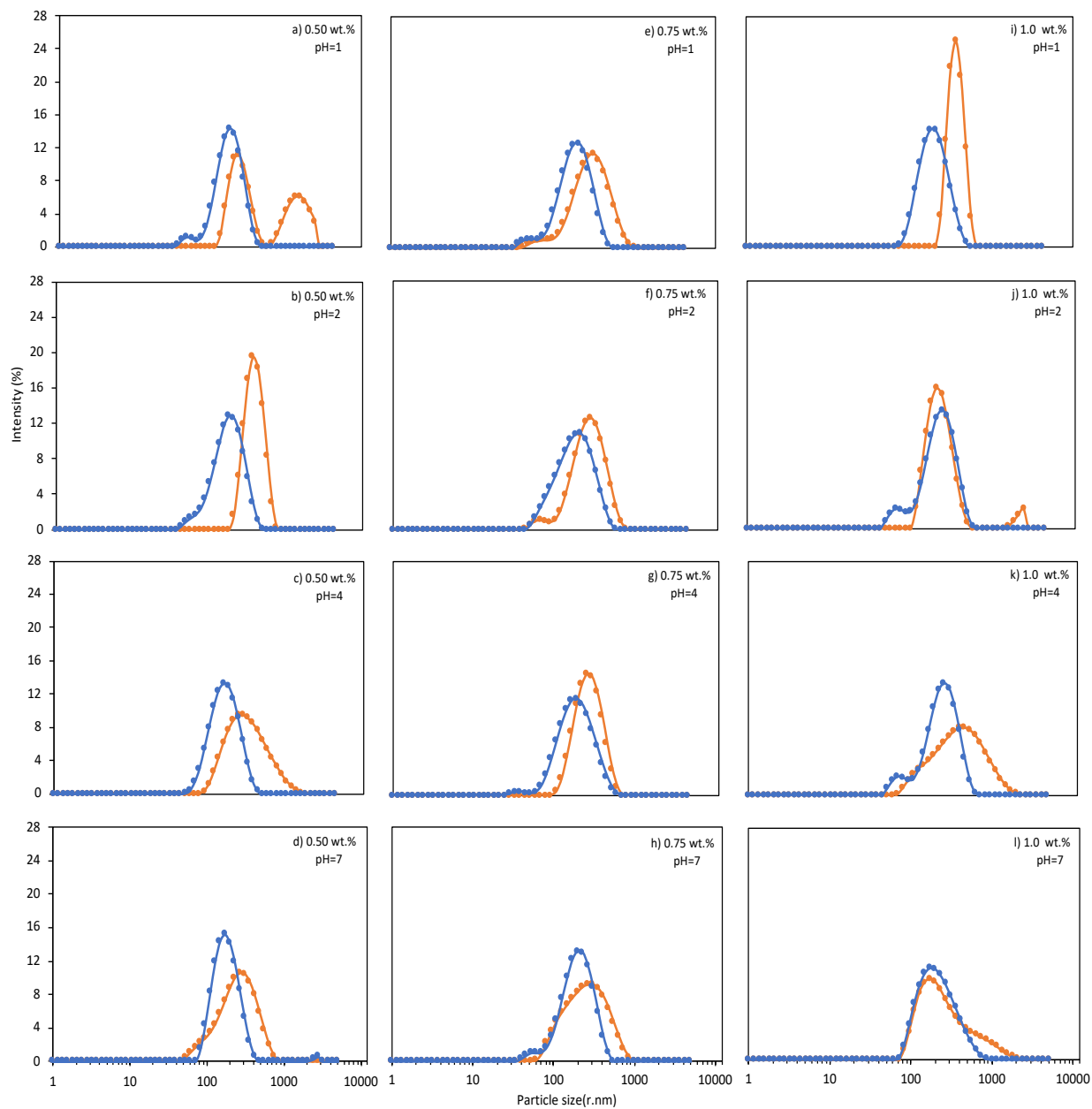
Figure 19: Size distribution (Intensity %) of S13 silica nanoparticles in the presence (orange fill and marker) and absence of electrolyte (blue fill and marker)

The effect of electrolyte addition on size distribution can also be seen in figure 20 given below as the Intensity mean diameter of particle in suspension increases sharply in the presence of an electrolyte.
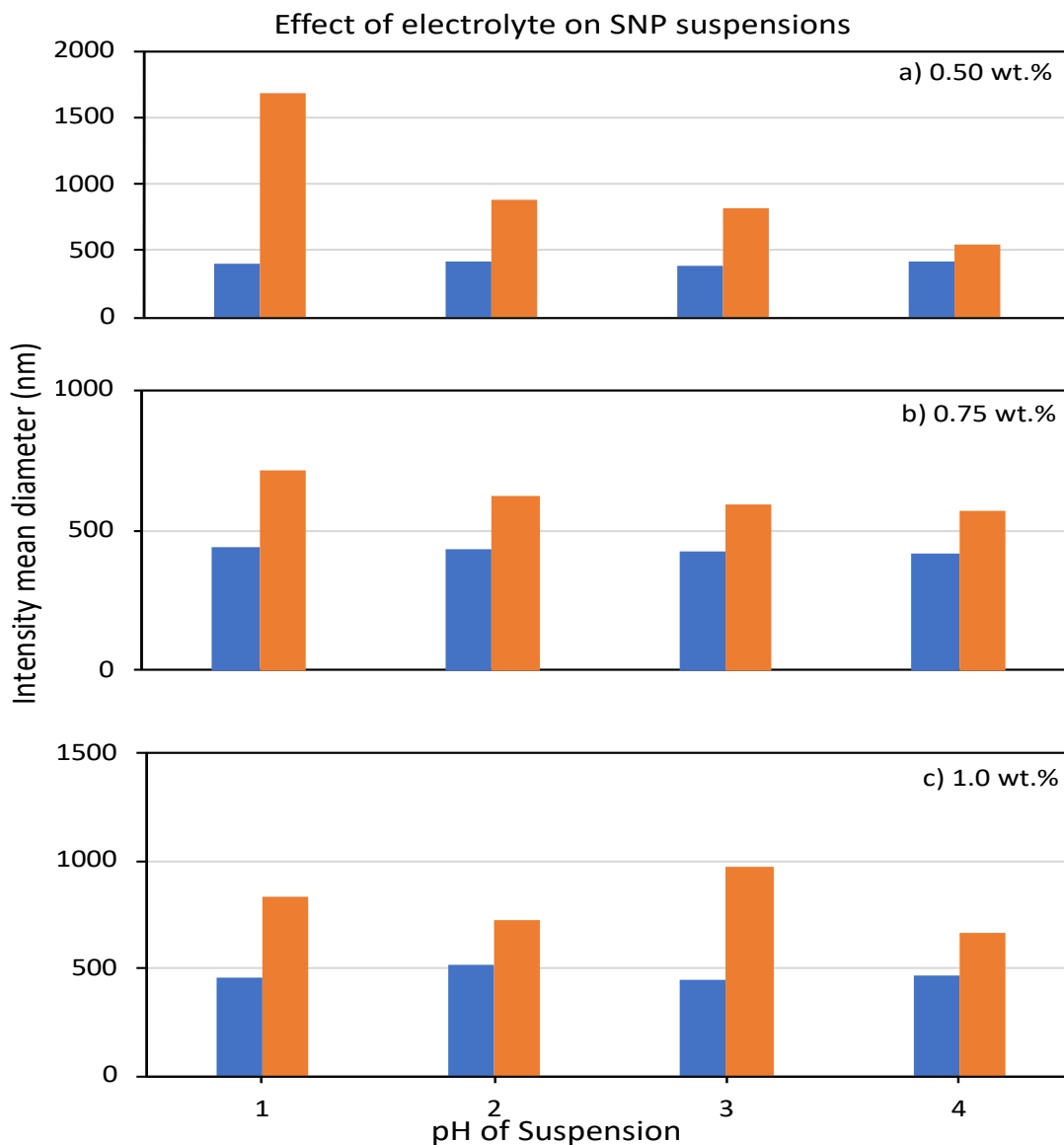
Figure 20: Intensity mean diameter for dilute S13 silica nanoparticles in the presence (orange bar) and absence (blue bar) of an electrolyte.

4.2 Relative viscosity of dilute Silica nanoparticle suspensions:

The volume fraction of solute particles has a useful role in determining the viscosity of a suspension. The relative viscosity of dilute silica nanoparticle suspensions was measured using Ubbelohde viscometer and plotted as a function of volume fraction of silica nanoparticles in suspension. Figure 21 shows the relative viscosity vs volume fraction for S13, T30 and N20 grades of silica. The plot presents a nearly linear relationship, though it lies way above the Einstein

equation for relative viscosity of hard spheres. Also, the relative viscosity of N20 silica suspensions increases more sharply than the S13 and T30 silica nanoparticle suspensions.
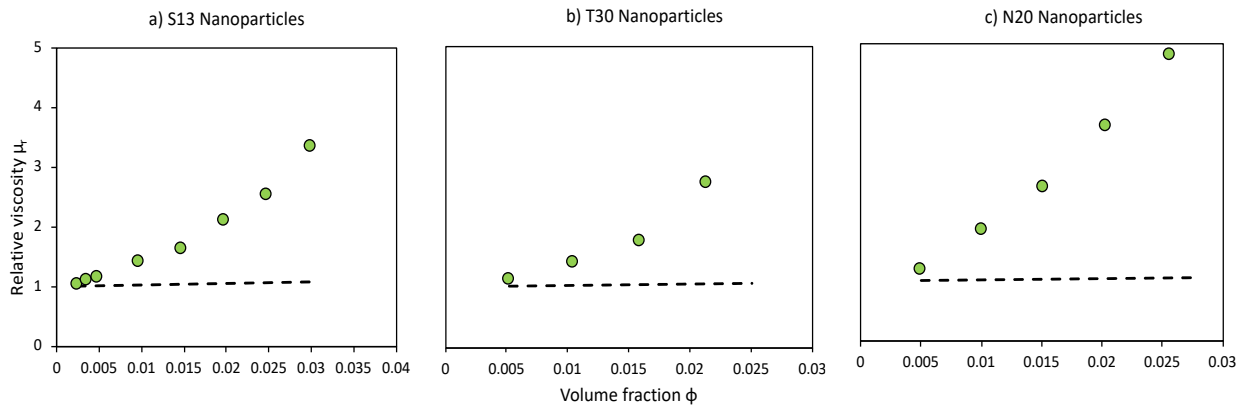
Figure 21: Viscosity of dilute silica nanoparticle suspensions; where green dot marker represents the experimental data and dashed line represents the Einstein equation data.

4.2.1 Effect of pH on relative viscosity:

A change in pH can control the concentration of positive and negative ions in the solution which in turn can manipulate the charge on the double layer. This change results in decrease or increase in inter-particle forces and can have a significant effect on relative viscosity of suspensions. The relative viscosity of S13 silica nanoparticles was studied as a function of pH and the effect of elevation in temperature was also investigated. Figure 22 and 23 show the results obtained:
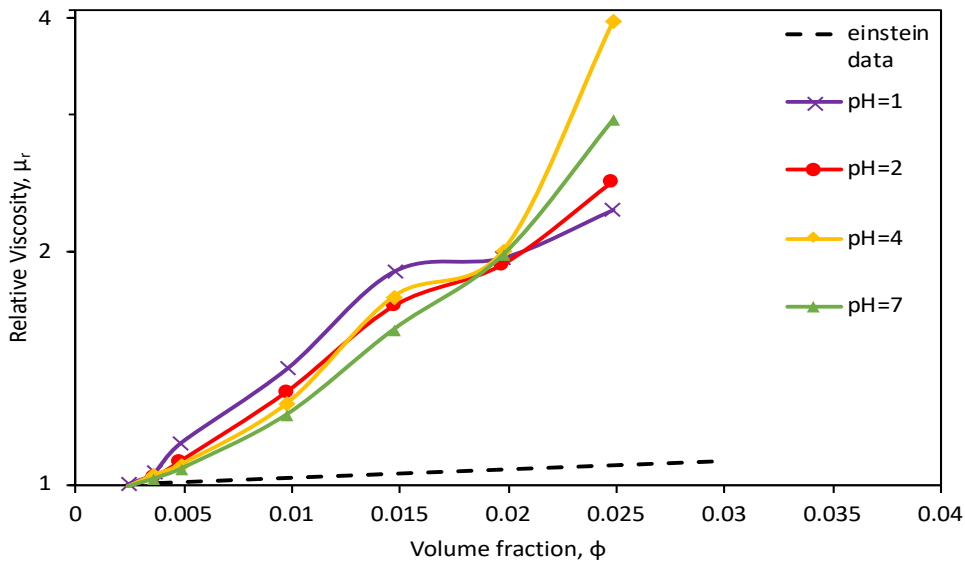
Figure 22: Relative viscosity vs volume fraction at different pH for dilute silica suspensions
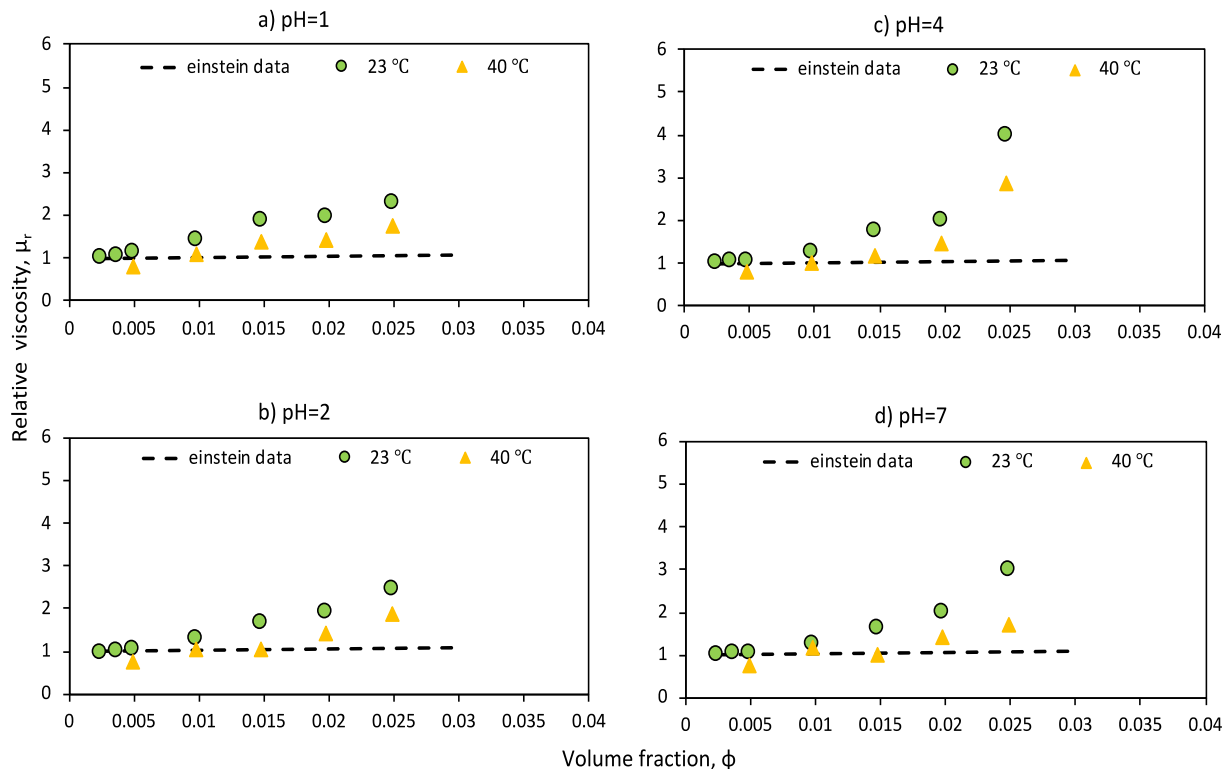
Figure 23: Effect of temperature on relative viscosity of S13 silica nanoparticle suspensions

It can be observed from the Figure 22 that at very low particle concentration, the relative viscosity for low pH values is slightly greater than at higher pH values but at relatively higher particle concentration (5 wt.%), the reverse happens; the relative viscosity is higher for suspensions at higher pH values. In Figure 23, it can be observed that with an increase in temperature, the relative viscosity of suspensions decreases irrespective of pH value of the suspension.

4.2.2 Effect of electrolyte presence on relative viscosity:

The presence of electrolyte can dramatically affect the viscosity of nanoparticle suspensions. Electrolyte presence diminishes the charge on double layer and hence also diminishes the repulsive forces of interaction between the particles in a suspension which can cause particle aggregation and an increase in viscosity. Figure 24 given below shows the comparison between the relative viscosity of suspensions in the presence of electrolyte and suspensions without any electrolyte presence.
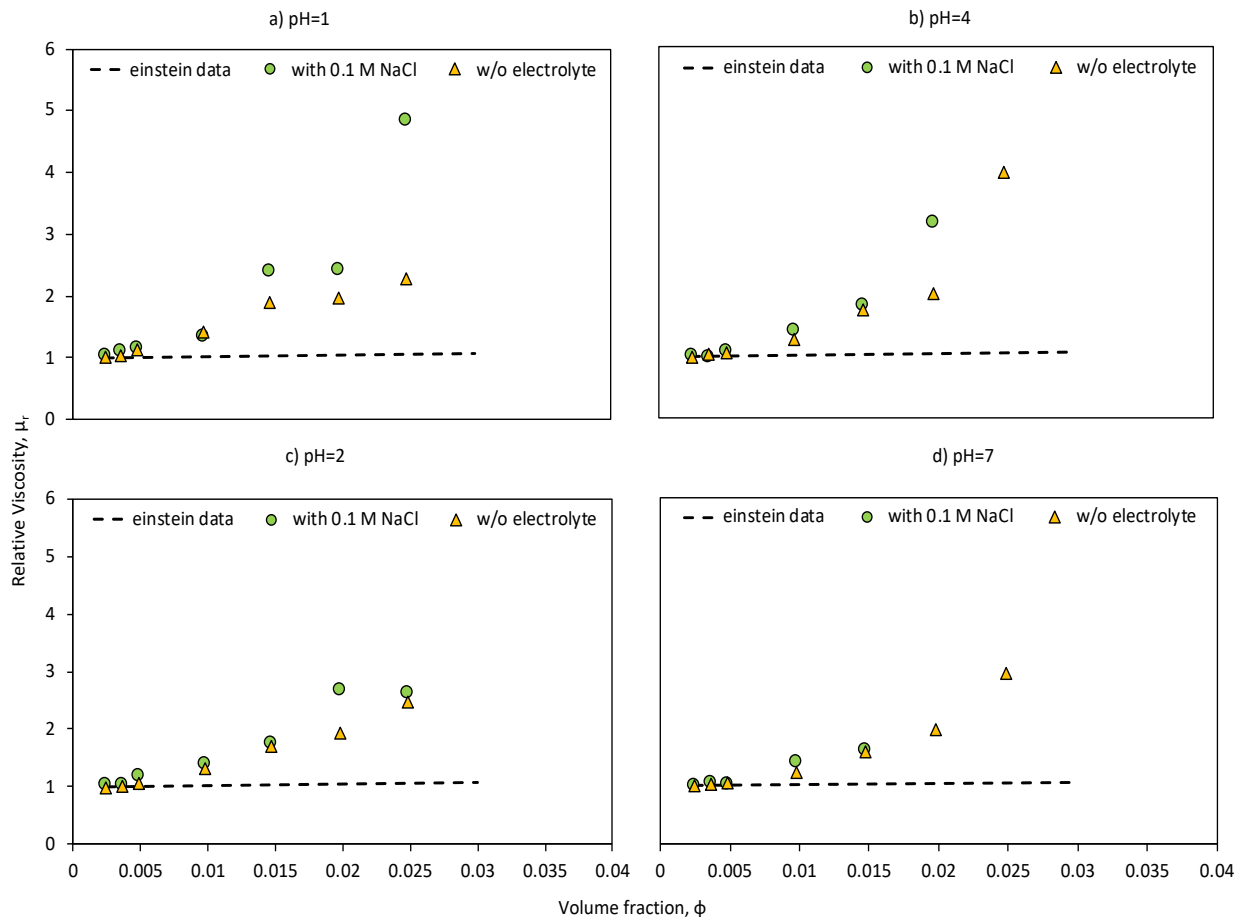
Figure 24: The effect of electrolyte on relative viscosity of silica nanoparticle suspensions

It was observed that the addition of electrolyte had an increasing effect on the viscosity of silica suspensions even for very low particle concentration samples. Though suspensions with low particle concentrations had a slight increase in relative viscosity irrespective of their pH whereas the viscosity of suspensions at pH=4 and pH=7 increased very sharply for relatively higher particle concentration values. The viscosity of 5 wt. % suspensions at pH=4 and 7 and 4 & 5 wt. % suspensions at pH=7 could not be measured using Capillary viscometer as their viscosity was too high for that viscometer. The effect of temperature was also investigated on relative viscosity of suspensions as shown in figure 25; it was observed that the relative viscosity decreases with increase in temperature of suspensions.
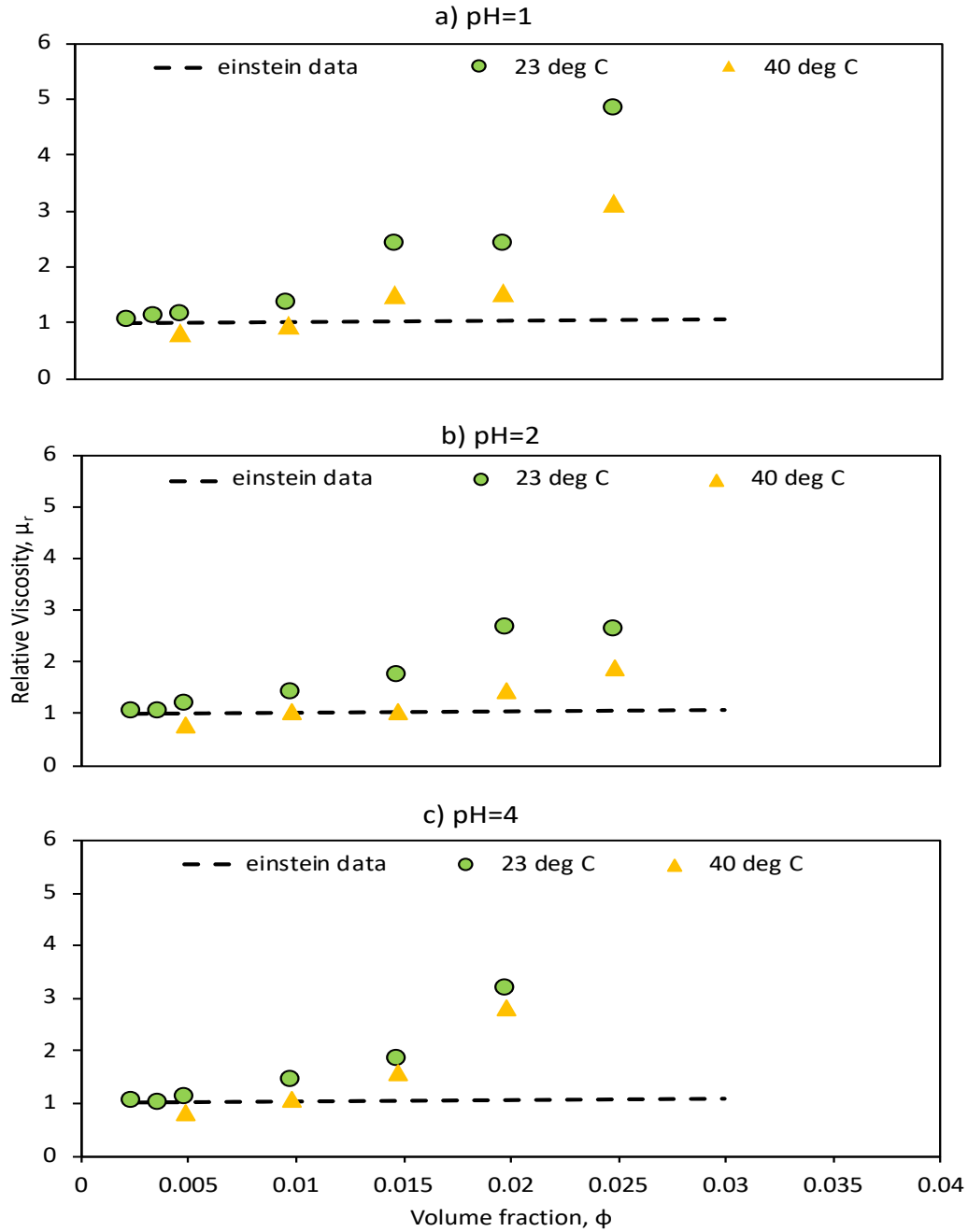
Figure 25: Effect of temperature on relative viscosity of suspensions with electrolyte presence

4.3 Rheology of concentrated suspensions:

The rheology of non-dilute silica suspensions was determined using Fann viscometer model 35 for room temperature experiments & Haake viscometer Rotovisco® RV 12 with system MV I system for elevated temperature experiments. The effect of temperature change and concentration on the rheology of suspensions was determined.

4.3.1 Effect of temperature:

Shear viscosity vs shear rate was investigated at different temperatures for S13, T30, N20 silica suspensions. The resulting plots, as shown in Figure 26, show that the suspensions behave as a shear thinning fluid for the given shear rates as the apparent viscosity of suspensions decreases with an increase in shear rate.
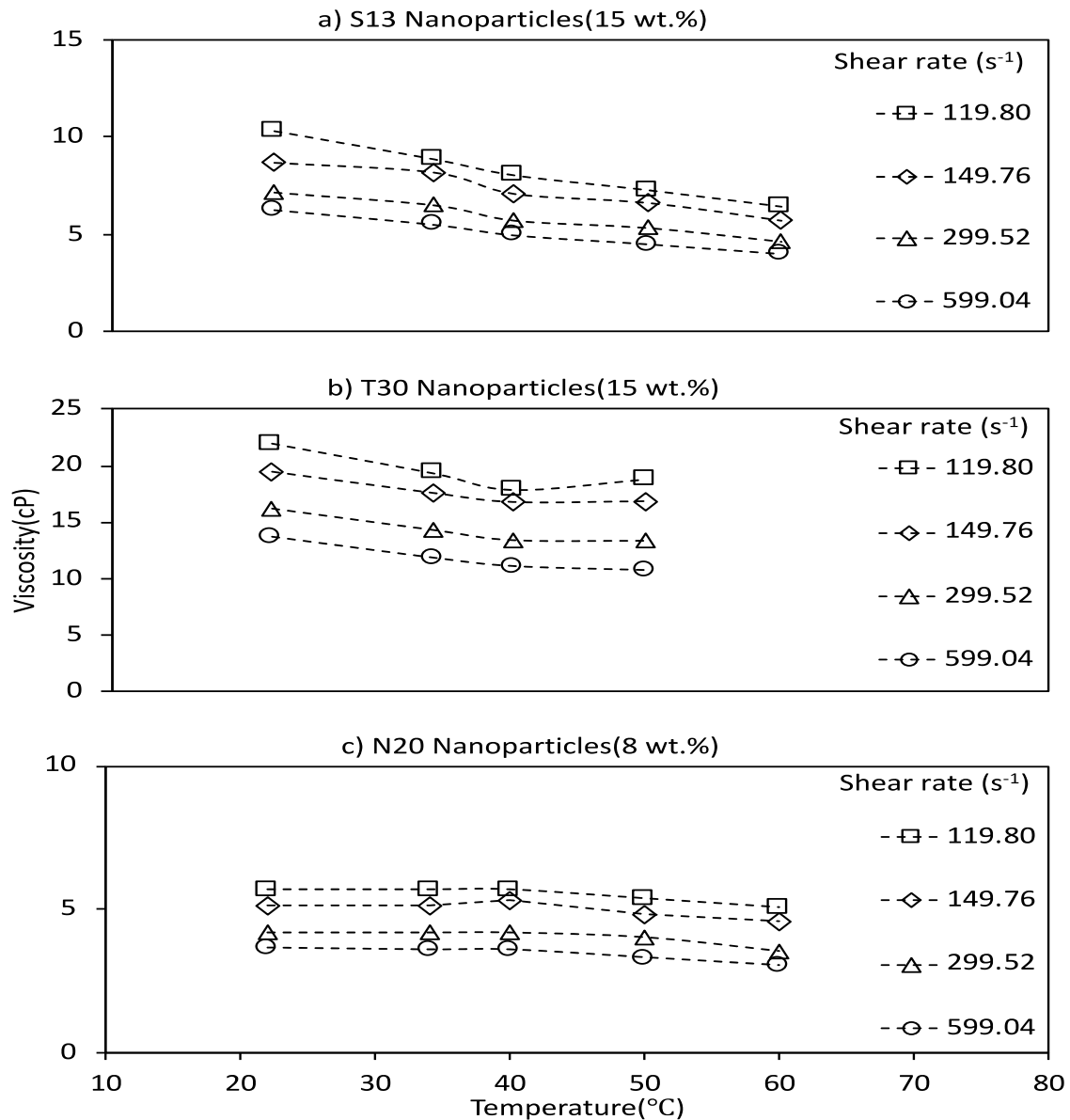
Figure 26: Viscosity vs shear rate behavior of S13, T30 and N20 silica nanoparticle suspensions at different operating temperatures

4.3.2 Effect of particle concentration:

The Shear viscosity of the hydrophilic grades of silica i.e. S13, N20 and T30 were measured as a function of shear rate for particle concentration samples. All the measurements were taken at room temperature of 22 °C. The flow was of shear thinning nature for the given shear rates. With an increase in particle concentration, the apparent viscosity increases for a fixed shear rate. The flow curves of fumed silica suspension can be fitted to a power law model as:

$$\mu = k\,\gamma^{-n} \tag{34}$$

Where μ is the apparent viscosity, γ is the shear rate, k is a consistency index representing the suspension's viscosity at a unit shear rate and n is the shear thinning index. The above equation can also be written as:

$$\log(\mu) = \log(k) - n\,log(\gamma) \tag{35}$$

The plots are given in Figure 27. It can be observed that all the hydrophilic grades of silica under investigation show a shear thinning nature. The values of k and n from power law curve fitting are mentioned in Table 5 as below:

Table 5: Values of shear-thinning index and consistency index for fumed silica suspensions

S13							
Concentration (wt. %)	6	7	8	9	10	15	20
n	0.281	0.247	0.248	0.257	0.319	0.406	0.415
k	19.50	18.76	22.99	25.52	40.78	181.62	341.39

T30						
Concentration (wt. %)	5	6	7	8	9	10
n	0.251	0.327	0.462	0.420	0.400	0.471
k	19.54	43.83	128.40	156.48	144.52	331.82

N20					
Concentration (wt. %)	6	7	8	9	10
n	0.356	0.350	0.358	0.380	0.389
k	43.67	49.04	68.77	92.32	185.67
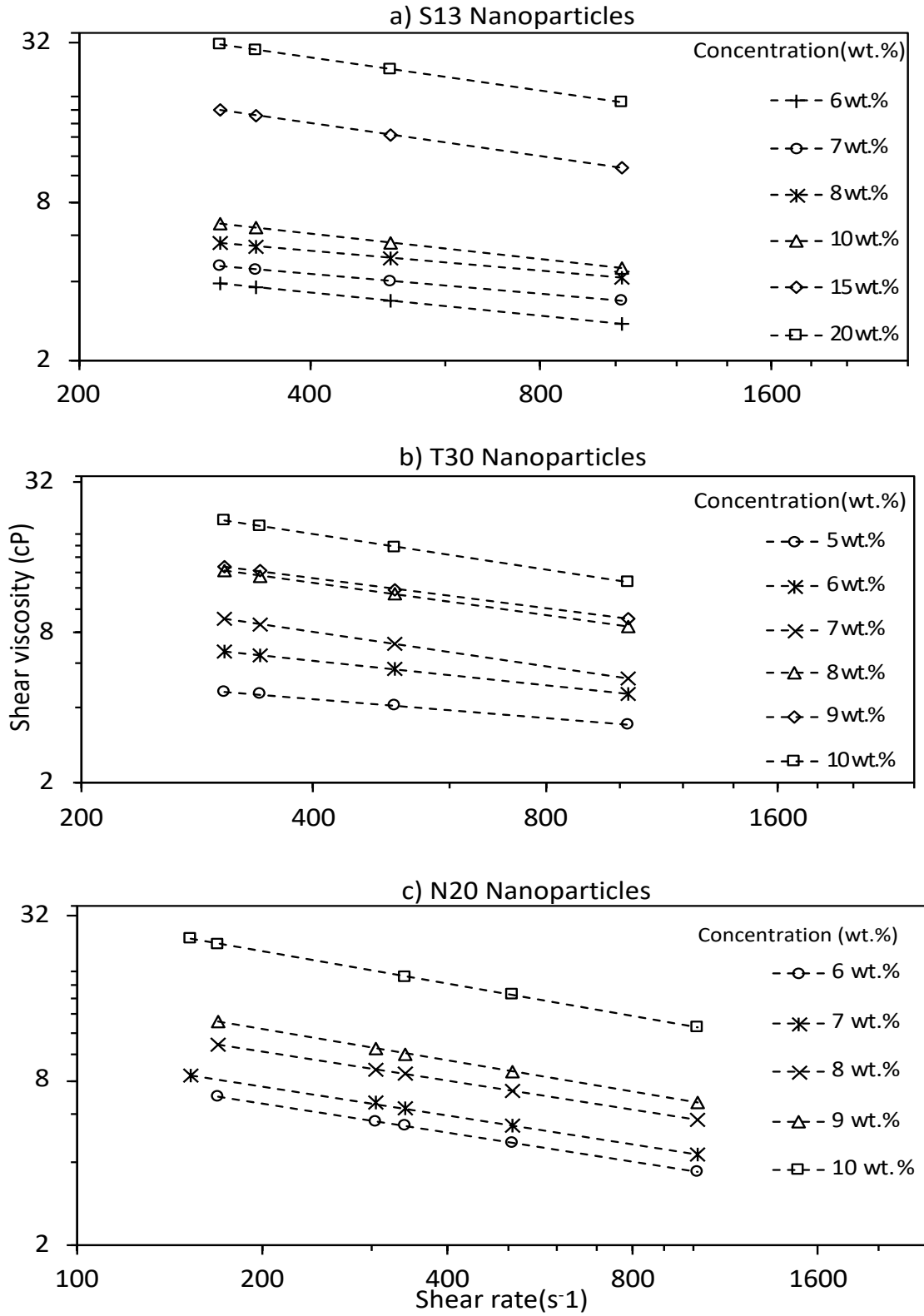
Figure 27: Apparent viscosity vs shear rate behavior of silica nanoparticle suspensions

4.4 Zeta Potential of fumed silica suspensions:

The zeta potential values give us an information about the charge on particles in suspensions. It also decides the stability of a colloidal system. A low or zero zeta potential value can diminish the repulsive forces between particles and can lead to precipitation. The effect of pH and electrolyte presence on zeta potential is explained in the sections below:

4.4.1 Zeta Potential of original silica suspensions:

Hydrophilic silica nanoparticles in aqueous state acquire negative charge due to the presence of silanol groups on them and hence their zeta potential values are negative. Table 6 summarizes the mean Zeta potential values for the three hydrophilic grades of silica. The Zeta Potential of all the three silica nanoparticles is negative indicating that the particles acquire negative charge in an aqueous phase. The magnitude of zeta potential decreases with an increase in particle concentration. High values of zeta potential indicate that suspensions are electrochemically stable.

Table 6: Mean Zeta Potential values for different concentrations of silica suspensions

Mean Zeta Potential(mV)			
Concentration (wt. %)	**S13**	**T30**	**N20**
0.05	-30	-24.2	-37.3
1	-38.5	-34.1	-36.7
5	-26.5	-20.8	-34.4

4.4.2 Effect of pH on Zeta potential:

A change in pH can change the concentration of H^+ and OH^- ions in solution and which can change the charge on double layer; hence changing the zeta potential of particles in suspension. The zeta potential of different fumed silica suspensions was measured for a set of pH values. Table 7 summarizes all the results obtained. Also, the zeta potential is plotted against the pH of the suspension in Figure 28. It can be observed from the results that zeta potential becomes increasingly negative with an increase in pH of the suspension. The I.E.P. of S13 fumed silica suspensions was found to be very close to 1.98 with zeta potential being 0.0319 mV at that pH. A shift in P.Z.C. is observed with an increase in particle concentration. This can be attributed to an increase in particle interaction due to an increase in particle concentration.

Table 7: Mean Zeta Potential values of silica nanoparticle suspensions at different pH values.

Mean Zeta Potential (mV)							
Particle conc. (wt. %)	0.5	0.75	1	2	3	4	5
pH=1	0.719	2.09	0.322	2.9	1.47	2.94	0.827
pH=2	-0.18	-0.085	-0.231	-0.425	0.199	0.084	0.108
pH=4	-13	-12.9	-11.1	-7.23	-3.53	-5.92	-13.9
pH=7	-48.2	-43.2	-35.7	-34.4	-32.9	-36.2	-37.5
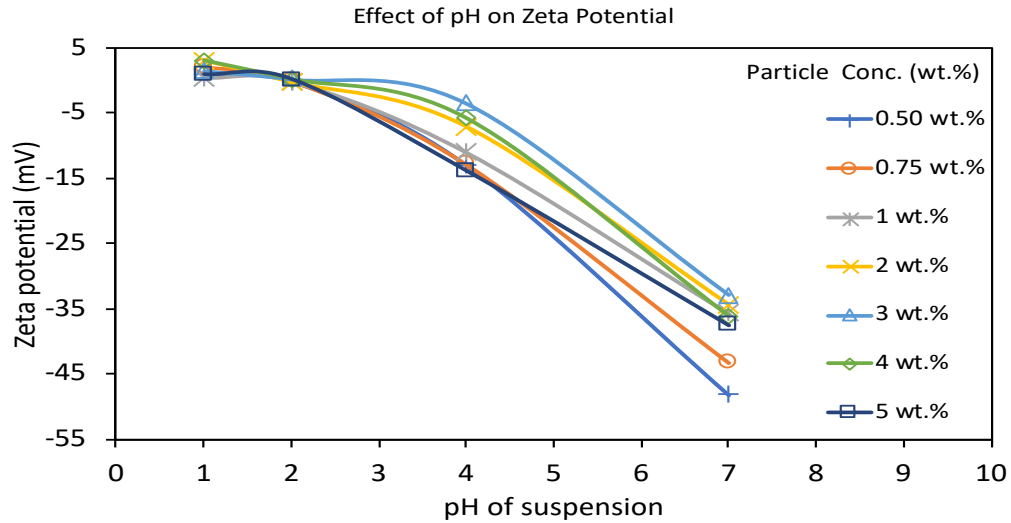
Figure 28: Effect of pH on zeta potential for S13 silica nanoparticle suspensions

4.4.3 Effect of electrolyte addition on Zeta potential:

To investigate the effect of electrolyte, suspensions prepared in the presence of 0.1 M NaCl were examined for zeta potential. Table 8 summarizes the mean zeta potential values obtained for S13 grade fumed silica suspensions in the presence of an electrolyte.

Table 8: Mean zeta potential values for fumed silica S13 suspensions with 0.1 M NaCl.

Mean Zeta Potential(mV)							
Particle conc. (wt.%)	0.5	0.75	1	2	3	4	5
pH=1	-1.8	-0.889	-1.63	-2.98	-1.13	-0.536	-1.51
pH=2	1.04	1.1	1.29	0.811	1.37	1.01	0.773
pH=4	-0.523	-1.23	-0.695	-0.107	-0.629	-0.629	-0.586
pH=7	-23.8	-23.7	-23.6	-23.8	-29.3	-28.7	--

It can be observed from the results obtained that the magnitude of zeta potential values for a pH value of 4 and 7 decreased with the addition of an electrolyte. This can be attributed to the compression of the double layer in the presence of electrolyte which partially neutralizes the charge

on the double layer due to the excess ions provided by the electrolyte. This is in an agreement with the DLVO theory. This can be easily noticed in figure 29. The zeta potential values show an anomalous behavior turning negative with a decrease in pH value from 2 to 1. Knowing that in the presence of an electrolyte, the point of zero charge shifts to a value between pH=2 and pH=4, getting a negative value of Zeta potential below pH=2 is an interesting observation. This might be due to specific adsorption of Cl$^-$ ions at very low pH providing a negative charge to the particle due to charge reversal phenomena.
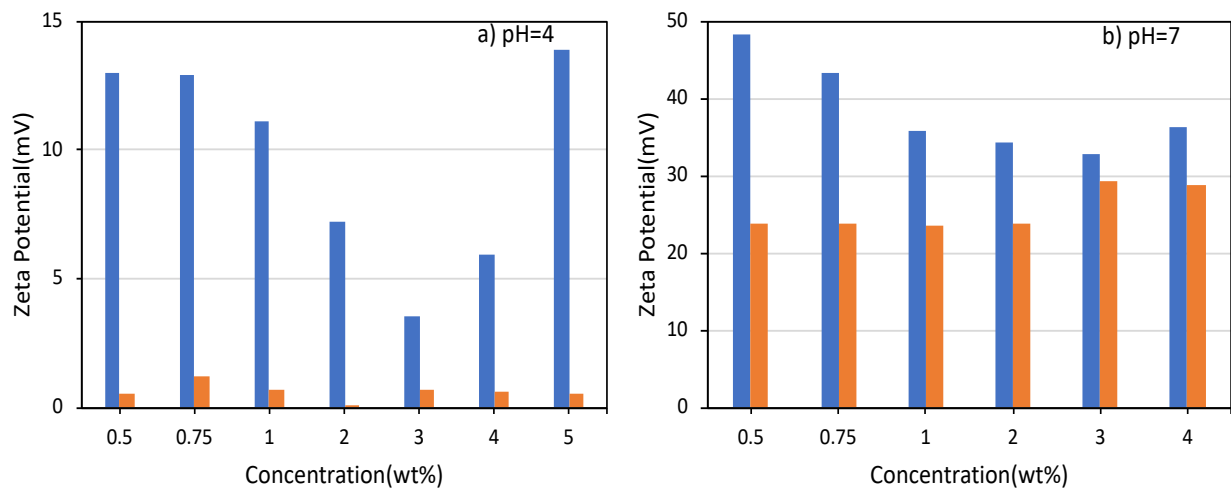
Figure 29: Effect of electrolyte presence on Zeta potential, the blue and orange bars represent the suspensions with and without the presence of 0.1 M NaCl respectively

4.5 Pipeline flow behavior of fumed silica suspensions:

Pipeline flow studies were conducted for low concentration S13 silica suspensions to investigate that if they have drag reducing characteristics or not. Flow loop experiments were conducted in 1, 1.5 and 0.5-inch nominal diameter pipelines. The drag reduction can be examined by comparing the experimental data of friction factor and the Blasius line. Figure 30 shows the fanning friction factor of 0.5, 0.75 1 and 2 wt.% S13 silica suspensions as compared to friction factor without their presence. As observed from the figure, friction factor line for 1 and 2 wt. % S13 suspensions fall close to water line whereas 0.75 and 0.50 wt. % S13 suspensions fall below the reference line showing drag reduction characteristics.
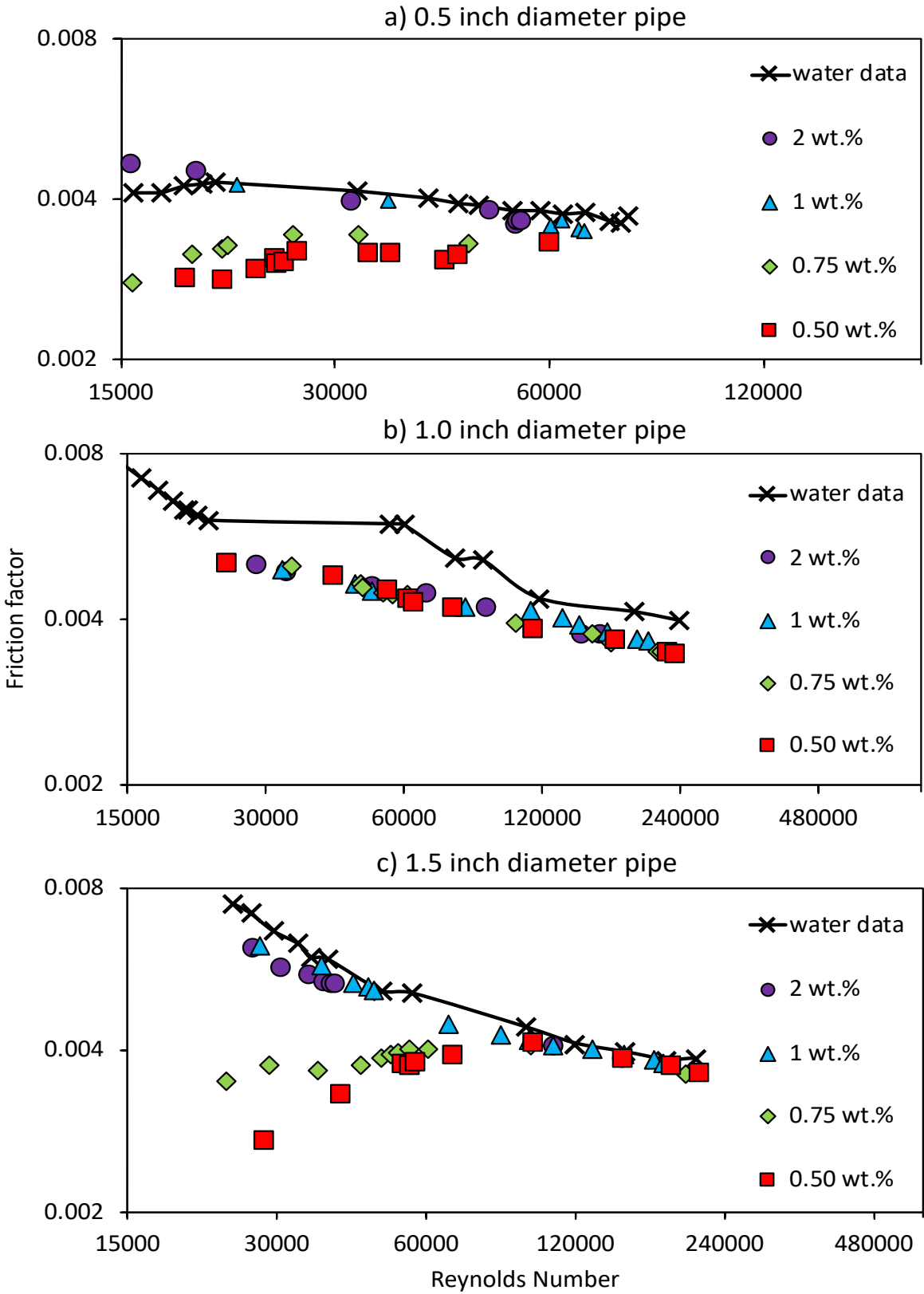
Figure 30: Friction factor vs. Reynolds number for S13 nanoparticle suspensions

Chapter 5: Conclusions

Owing to their unique properties, silica nanoparticles have a lot of potential applications in a number of industries. After a careful examination of rheological behavior, particle size distribution, zeta potential and pipeline flow behavior results, following conclusions can be made:

1. All the grades of silica nanoparticle suspensions show shear-thinning behavior showing a decrease in apparent viscosity with an increase in shear rate. Also, the shear viscosity of suspensions decreases with an increase in temperature for all the particle concentrations irrespective of pH and presence of an electrolyte.

2. The relative viscosity of suspensions increases more rapidly than what is predicted by the Einstein equation for hard spheres. Also, the relative viscosity of suspensions with very low particle concentration is slightly higher at low pH values whereas with an increase in particle concentration, suspensions show higher viscosity at high pH values.

3. The presence of electrolyte has an increasing effect on the viscosity of suspensions and the effect is more pronounced at high pH values and higher particle concentrations, with the suspensions becoming highly viscous for higher particle concentration.

4. Size distribution results do not show any specific pattern with a change in pH in absence of an electrolyte whereas in the presence of electrolyte, peaks show higher particle size indicating the bigger aggregates in the presence of an electrolyte.

5. Zeta potential results show that particles acquire negative charge in an aqueous phase and zeta potential values decrease in magnitude with increase in particle concentration indicating the increase in particle interaction at higher particle concentrations. The highly negative zeta potential values indicate that the suspensions are electrochemically stable at low particle concentrations.

6. In the absence of an electrolyte, zeta potential results show that the Iso-electric point lies close to 1.98. Also, the zeta potential results indicate that the P.Z.C. (Point of zero charge) shifts with an increase in particle concentration due to the increase in interaction between particles at higher concentration. In the presence of an electrolyte, zeta potential values become smaller indicating the compression of double layer whereas the sign of zeta potential values shows an anomalous behavior which could probably happen due to the specific interaction of co-ion at low pH values.

7. Pipeline flow results show that suspensions with low particle concentration (0.50 and 0.75 wt. %) have drag reduction properties as the friction factor vs Reynolds number line falls slightly below the water line (reference line) whereas a little increase in particle concentration loses the drag reduction properties of the suspension as confirmed by the closeness of the friction factor vs Reynolds number line with the water line (reference line) for 1 and 2 wt. % suspensions.

Bibliography

1. Xue, X.Y., J.F. Stebbins, M. Kanzaki, P.F. McMillan, & Poe, B. (1991). Pressure-Induced Silicon Coordination and Tetrahedral Structural-Changes in Alkali Oxide-Silica Melts up to 12 GPA: NMR, Raman, and Infrared-Spectroscopy. *American Mineralogist*, 76(1-2), 8-26.

2. Ronhovde, C. J. (2017). Biomedical applications of mesoporous silica particles (Order No. 10282376). (Doctoral dissertation, University of Iowa, USA).

3. Liu, X., Lu, X., Wen, P., Shu, X., & Chi, F. (2017). Synthesis of ultra-small silica nanoparticles for application as deep-ultraviolet antireflection coatings. *Applied Surface Science*, 420, 180–185.

4. Fedorenko, S. V., Jilkin, M. E., Gryaznova, T. V., Iurko, E. O., Bochkova, O. D., Mukhametshina, A. R., Budnikova, Y. H. (2017). Silica Nano spheres Coated by Ultra small Ag^0 Nanoparticles for Oxidative Catalytic Application. *Colloid and Interface Science Communications*, 21, 1-5.

5. Nanda, D., Varshney, P., Satapathy, M., Mohapatra, S. S., & Kumar, A. (2017). Self-assembled monolayer of functionalized silica micro particles for self-cleaning applications. *Colloids and Surfaces A: Physicochemical and Engineering Aspects*, 529, 231–238.

6. Ojeda-Mendoza, G. J., Contreras-Tello, H., & Rojas-Ochoa, L. F. (2018). Refractive index matching of large poly disperse silica spheres in aqueous suspensions. *Colloids and Surfaces A: Physicochemical and Engineering Aspects*, 538, 320–326.

7. Kummel, A. C., Liberman, A., Mendez, N., & Trogler, W. C. (2014). Synthesis and surface functionalization of silica nanoparticles for nanomedicine. *Surface Science Reports*, 69, 132–158.

8. Martin, K. R. (2013). Silicon: The health benefits of a metalloid. *Metal Ions in Life Sciences*, 13, 451–473.

9. Kang, T. J., Kim, C. Y., & Hong, K. H. (2012). Rheological behavior of concentrated silica suspension and its application to soft armor. *Journal of Applied Polymer Science*, 124(2), 1534–1541.

10. Kawaguchi, M. (2017). Suspension stabilities and rheological properties of fumed silica suspensions. *Journal of Suspension Science and Technology*, 38(5), 642–660.

11. White, L., & Duffy, G. (1959). Vapor-Phase Production of Colloidal Silica. *Industrial Engineering Chemistry*, 51(3), 232–238.

12. Ertl, G., Knozinger, H., & Weitkamp, J. (1999). Flame Hydrolysis. In *Preparation of Solid Catalysts,* 99–109.

13. Barthel, H. (1999). Particle Sizes of Fumed Silica. In *Particle & Particle Systems Characterization*, 16(4), 169–176.

14. Zhuravlev, L. T. (2000). The surface chemistry of amorphous silica: Zhuravlev model. *Colloids and Surfaces A: Physicochemical and Engineering Aspects*, 173, 1-38.

15. Barthel, H. (1995). Surface interactions of dimethylsiloxy group-modified fumed silica. *Colloids and Surfaces A: Physicochemical and Engineering Aspects*, 101(2–3), 217–226.

16. Frahn, S., Ettlinger, M., Ladwig, T., & Mendel, W. (2001). Surface modified fumed silicas. *European Coatings Journal*, (3), 98–105.

17. Raghavan, S. R., Riley, M. W., Fedkiw, P. S., & Khan, S. A. (1998). Composite Polymer Electrolytes Based on Poly (ethylene glycol) and Hydrophobic Fumed Silica: Dynamic Rheology and Microstructure. *Chemistry of Materials*, *10*(1), 244–251.

18. Yu, Y., Wu, R., & Clark, M. (2010). Phosphate removal by hydrothermally modified fumed silica and pulverized oyster shell. *Journal of Colloid and Interface Science*, *350*(2), 538–543.

19. Yu, Y., Wang, J., & Parr, J. F. (2012). Preparation and properties of TiO_2/fumed silica composite photocatalytic materials. In *Procedia Engineering,* 27, 448–456.

20. Carolin, C. F., Kumar, P. S., Saravanan, A., Joshiba, G. J., & Naushad, M. (2017). Efficient techniques for the removal of toxic heavy metals from aquatic environment: A review. *Journal of Environmental Chemical Engineering*, 5(3), 2782-2799.

21. Caprarescu, S., Purcar, V., & Vaireanu, D. I. (2012). Separation of Copper Ions from Synthetically Prepared Electroplating Wastewater at Different Operating Conditions using Electro dialysis. *Separation Science and Technology (Philadelphia)*, 47(16), 2273–2280.

22. Caprarescu, S., Radu, A. L., Purcar, V., Ianchis, R., Sarbu, A., Ghiurea, M., Ebrasu, D. I. (2015). Adsorbents/ion exchangers-PVA blend membranes: Preparation, characterization and performance for the removal of Zn^{2+} by Electro dialysis. *Applied Surface Science*, 329, 65–75.

23. Petcu, C., Purcar, V., Radu, A. L., Ianchis, R., Elvira, A., Sarbu, A., Ciobotaru, A. I. (2015). Removal of zinc ions from model wastewater system using bi copolymer membranes with fumed silica. *Journal of Water Process Engineering*, 8, 1–10.

24. Christ, U., & Bittner, A. (1994). Rheology control of organic coatings with new hydrophobic silica's. *Progress in Organic Coatings*, *24*(1–4), 29–41.

25. Cheraghian, G. (2016). Application of Nano-fumed silica in heavy oil recovery. *Petroleum Science and Technology*, 34(1), 12–18.

26. Lee, D. W., & Yoo, B. R. (2016). Advanced silica/polymer composites: Materials and applications. *Journal of Industrial and Engineering Chemistry*, 38, 1-12.

27. Botti, A., Pyckhout-Hintzen, W., Richter, D., Urban, V., Straube, E., & Kohlbrecher, J. (2003). Silica filled elastomers: Polymer chain and filler characterization in the un deformed state by a SANS-SAXS approach. *Polymer*, 44(24), 7505–7512.

28. Ma, M., Hill, R. M., & Minglin, M. and Randal, M. H. (2006). Super hydrophobic Surfaces. *Current Opinion in Colloid and Interface Science*, 11, 193–202.

29. Eight, C., Bazaka, K., Bazaka, O., Crawford, R. J., Ivanova, E. P., Gervinskas, G., Ivanova, E.P. (2015). The Design of Super Hydrophobic Surfaces. In *Super Hydrophobic Surfaces*, 27–49.

30. Nanda, D., Varshney, P., Satapathy, M., Mohapatra, S. S., & Kumar, A. (2017). Self-assembled monolayer of functionalized silica micro particles for self-cleaning applications. *Colloids and Surfaces A: Physicochemical and Engineering Aspects*, *529*, 231–238.

31. Veluswamy, H. P., Prasad, P. S. R., & Linga, P. (2016). Mechanism of methane hydrate formation in the presence of hollow silica. *Korean Journal of Chemical Engineering*, *33*(7), 2050–2062.

32. Veluswamy, H. P., Kumar, A., Kumar, R., & Linga, P. (2017). An innovative approach to enhance methane hydrate formation kinetics with leucine for energy storage application. *Applied Energy*, *188*, 190–199.

33. Chari, V. D., Sharma, D. V. S. G. K., Prasad, P. S. R., & Murthy, S. R. (2013). Methane hydrates formation and dissociation in Nano silica suspension. *Journal of Natural Gas Science and Engineering*, *11*, 7–11.

34. Mang, T., & Dresel, W. (2007). Solid lubrication. In *Lubricants and Lubrication: Second Edition*,1–850. John Wiley and Sons.

35. Reghan, J. H. (2005). Suspension Acoustics: An introduction to the Physics of suspensions. *Journal of Fluids and Structures*, 23(1), 157-158. Cambridge University Press.

36. Wagner, J. R., Mount, E. M., & Giles, H. F. (2014). Polymer rheology. *Extrusion: The Definitive Processing Guide and Handbook: Second Edition*,233-240, William Andrew Publishing.

37. Strivens, T.A. (1999). An introduction to rheology. In Woodhead Publishing Series in Metals and Surface Engineering. *Paint and Surface Coatings* (Second Edition), 550–574.

38. Irgens, F. (2014). Classification of Fluids. In *Rheology and Non-Newtonian Fluids*. Springer Cham, 1-16.

39. Chhabra, R. P., & Richardson, J. F. (1999). Non-Newtonian fluid behavior. In *Non-Newtonian Flow in the Process Industries*, 1-36. Elsevier.

40. Bird, R. B., Stewart, W. E., & Lightfoot, E. N. (2007). Viscosity and the Mechanisms of Momentum transport. *Transport Phenomena*, *55*(1), 3–17.

41. Chhabra, R. P. (2010). Non-Newtonian fluids: An introduction. In *Rheology of Complex Fluids,* 3–34. Springer New York.

42. Morrison, F. A. (2001). How much do I need to learn about rheology? In *Understanding Rheology*, 1-9. Oxford University Press.

43. Boger, D. V. (1977). Demonstration of upper and lower Newtonian fluid behavior in a pseudo plastic fluid. *Nature,265, 126-128*.

44. Barnes, H. A., & Hutton, J. F. (1989). Viscosity. In *An Introduction to Rheology*,23. Elsevier.

45. Chhabra, R. P., & Richardson, J. F. (2008). Non-Newtonian fluid behavior. *In Non-Newtonian Flow and Applied Rheology, 1-55*.

46. Metzner, A. B., & Whitlock, M. (1958). Flow Behavior of Concentrated (Dilatant) Suspensions. *Transactions of the Society of Rheology*, *2*(1), 239–254.

47. Rehm, B., Haghshenas, A., Paknejad, A., Al-Yami, A., Hughes, J., & Schubert, J. (2012). Flow Drilling: Underbalance Drilling with liquid single-phase systems. In *Underbalanced Drilling: Limits and Extremes*, 39–108.

48. Tornberg, E. (2017). Influence of Fibers and particle size distribution on food rheology. In *Advances in Food Rheology and its Applications*, 177–208.

49. Francis, L. F., Stadler, B. J. H., & Roberts, C. C. (2016). Dispersion and Solution processes. In *Materials Processing: A Unified Approach to Processing of Metals, Ceramics and Polymers,* 1–597. Elsevier Inc.

50. Bowen, W. R., & Hilal, N. (2009). Measurement of particle and surface interactions using Force Microscopy. *Atomic Force Microscopy in Process Engineering, 31-80.* Elsevier Ltd.

51. Ranade, M. B. (1987). Adhesion and removal of fine particles on surfaces. *Aerosol Science and Technology*, *7*(2), 161–176.

52. Kern, W. (1993). *Handbook of semiconductor wafer cleaning technology. New Jersey: Noyes Publication*, 111–196. William Andrew Inc.

53. Reinhardt, K., & Kern, W. (2008). Handbook of Silicon Wafer Cleaning Technology (Second Edition). *William Andrew Inc*.

54. Olsson, U., Holmberg, K., & Olsson, U. (2002). Surface chemistry in dispersion, flocculation and flotation. *Handbook of Applied Surface and Colloid Chemistry*, 219-249.

55. Schramm, L. L. (1996). Suspensions: Basic principles. In *Suspensions: Fundamentals and Applications in the Petroleum Industry* (Vol. 251, pp. 3–44).

56. Yokoyama, K., Koike, Y., Masuda, A., & Kawaguchi, M. (2007). Rheological properties of fumed silica suspensions in the presence of potassium chloride. *Japanese Journal of Applied Physics, 46*(1), 328–332.

57. Kalman, D. P., Merrill, R. L., Wagner, N. J., & Wetzel, E. D. (2009). Effect of particle hardness on the penetration behavior of fabrics intercalated with dry particles and concentrated particle-fluid suspensions. *ACS Applied Materials and Interfaces*, *1*(11), 2602–2612.

58. Maranzano, B. J., & Wagner, N. J. (2001). The effects of particle-size on reversible shear thickening of concentrated colloidal dispersions. *Journal Of Chemical Physics*, *114*(23), 10514–10527.

59. Maranzano, B. J., & Wagner, N. J. (2001). The effects of inter particle interactions and particle size on reversible shear thickening: Hard-sphere colloidal dispersions. *Journal of Rheology*, *45*(5), 1205–1222.

60. Warren, J., Offenberger, S., Toghiani, H., Pittman, C. U., Lacy, T. E., & Kundu, S. (2015). Effect of Temperature on the Shear-Thickening Behavior of Fumed Silica Suspensions. *ACS Applied Materials and Interfaces*, *7*(33), 18650–18661.

61. Kawaguchi, M., Yamamoto, T., & Kato, T. (1996). Rheological Studies of Hydrophilic and Hydrophobic Silica Suspensions in the Presence of Adsorbed Poly (N -isopropyl acrylamide). *Langmuir*, *12*(26), 6184–6187.

62. Khandavalli, S., & Rothstein, J. P. (2014). Extensional rheology of shear-thickening fumed silica nanoparticles dispersed in an aqueous polyethylene oxide solution. *Journal of Rheology*, *58*(2), 411–431.

63. Hasanzadeh, M., Mottaghitalab, V., & Rezaei, M. (2015). Rheological and viscoelastic behavior of concentrated colloidal suspensions of silica nanoparticles: A response surface methodology approach. *Advanced Powder Technology*, *26*(6), 1570–1577.

64. Raghavan, S. R., & Khan, S. A. (1997). Shear-thickening response of fumed silica suspensions under steady and oscillatory shear. *Journal of Colloid and Interface Science*, *185*(1), 57–67.

65. Wagner, N. J., & Brady, J. F. (2009). Shear thickening in colloidal dispersions. *Physics Today*, *62*(10), 27–32.

66. Maranzano, B. J., & Wagner, N. J. (2002). Flow-small angle neutron scattering measurements of colloidal dispersion microstructure evolution through the shear thickening transition. *Journal of Chemical Physics*, *117*(22), 10291–10302.

67. Shan, L., Tian, Y., Jiang, J., Zhang, X., & Meng, Y. (2015). Effects of pH on shear thinning and thickening behaviors of fumed silica suspensions. *Colloids and Surfaces A: Physicochemical and Engineering Aspects*, *464*, 1–7.

68. Chen, S., Oye, G., & Sjoblom, J. (2006). Rheological Properties of Aqueous Silica Particle Suspensions. *Journal of Dispersion Science and Technology*, *26*, 495–501.

69. Amiri, A., Oye, G., & Sjoblom, J. (2009). Influence of pH, high salinity and particle concentration on stability and rheological properties of aqueous suspensions of fumed silica. *Colloids and Surfaces A: Physicochemical and Engineering Aspects*, *349*(1–3), 43–54.

70. Hartley, P. G., Larson, I., & Scales, P. J. (1997). Electrokinetic and Direct Force Measurements between Silica and Mica Surfaces in Dilute Electrolyte Solutions. *Langmuir*, *13*(8), 2207–2214.

71. Taran, E., Donose, B. C., Vakarelski, I. U., & Higashitani, K. (2006). PH dependence of friction forces between silica surfaces in solutions. *Journal of Colloid and Interface Science*, *297*(1), 199–203.

72. Kundu, P., Cohen, I., & Dowling, D. (2012). Introduction. In *Fluid Mechanics (fifth edition)*. Elsevier Inc.

73. Laminar vs. Turbulent flow. https://www.cfdsupport.com/OpenFOAM-Training-by-CFD-Support/node275.html. Accessed March 5, 2018.

74. Arnold, K. & Stewart, M. (1999). Choosing a Process. In *Surface Production Operations: Design of Oil-Handling Systems and Facilities*, 26–57.

75. Richardson, J. F., Harker, J. H., & Backhurst, J. R. (1991). Coulson and Richardson's Chemical Engineering – Fluid Flow, Heat Transfer and Mass Transfer, 1(6). *Chemical Engineering Science*.

76. Nakayama, Y. & Boucher, R. F. (1998). Flow in pipes. In *Introduction to Fluid Mechanics*, 111–135.

77. Holland, F. A., & Bragg, R. (1995). Fluids in motion. In *Fluid Flow for Chemical Engineers (Second edition)*, Butterworth-Heinemann, Oxford, 1–69.

78. Ratcliff, G. A. (1957). Unit operations of chemical engineering. *Chemical Engineering Science*, *6*(6), 287.

79. Peker, S. M., Helvaci, S. S., Helvacı, Ş. Ş., Yener, H. B., İkizler, B., & Alparslan, A. (2008). Non-Newtonian Behavior of Solid–Liquid Suspension. *Solid-Liquid Two Phase Flow*, 71–165.

80. Taler, D. (2016). Determining velocity and friction factor for turbulent flow in smooth tubes. *International Journal of Thermal Sciences*, *105*, 109–122.

81. Karman, V.T., Turbulence and Skin Friction (1934). *Journal of the Aeronautical Sciences*, 1(1), 1-20.

82. Moody, L. F. (1944). Friction factors for pipe flow. *Transaction of the ASME*, *66*, 671–684.

83. Colebrook, C. F. (1939). Turbulent flow in pipes, with particular reference to the transition region between the smooth and rough pipe laws. *Journal of the Institution of Civil Engineers*, *11*(4), 133–156.

84. Menon, E. S. (2015). Fluid flow in pipes. In *Transmission Pipeline Calculations and Simulations Manual*, 149–234. Elsevier Inc.

85. Toms, B.A. (1948). Some observations on the flow of linear polymer solutions through strait tubes at large Reynolds numbers. North Holland, Amsterdam, Proceedings in 1st International Congress on Rheology 2, 135–141.

86. Metzner, A., & Park, M. (1964). Turbulent flow characteristics of viscoelastic fluids. *Journal of Fluid Mechanics*, *20*(2), 291-303.

87. Lumley, J. L. (1969). Drag reduction by additives. *Annual Review of Fluid Mechanics*, *1*(1), 367–384.

88. Virk, P. S. (1975). Drag reduction fundamentals. *AIChE Journal, 21(4), 625-656*.

89. Zakin, J. L., & Hunston, D. L. (1978). Effects of solvent nature on the mechanical degradation of high polymer solutions. *Journal of Applied Polymer Science*.

90. Mohsenipour, A. A., & Pal, R. (2013). Synergistic effects of anionic surfactant and nonionic polymer additives on drag reduction. *Chemical Engineering Communications*, *200*(7), 935–958.

91. Eskin, D. (2017). Modeling an effect of pipe diameter on turbulent drag reduction. *Chemical Engineering Science*, *162*, 66–68.

92. Lim, G. H., Choi, H. J., Renou, F., & Roy, A. N. (2017). Effects of hydrophobic modification of xanthan gum on its turbulent drag reduction characteristics. *Journal of Industrial and Engineering Chemistry*, *54*, 146–150.

93. Pal, R. (2007). Mechanism of turbulent drag reduction in emulsions and bubbly suspensions. *Industrial and Engineering Chemistry Research*, *46*(2), 618–622.

94. Dai, X., Liu, H., Zhang, Y., & Li, J. (2016). Influence of TiO_2 on drag reduction and shear degradation resistance of polyolefin in diesel: Proceedings of the International Conference on Materials Science, Energy Technology and Environmental Engineering, 397-400.

95. Yanuar, Mau, S., Waskito, K. T., Putra, O. A., & Hanif, R. (2017). Drag reduction of alumina nanofluid in spiral pipe with turbulent flow conditions. In *AIP Conference Proceedings*, 1826. American Institute of Physics Inc.

96. Steele, A., Bayer, I. S., & Loth, E. (2014). Pipe flow drag reduction effects from carbon nanotube additives. *Carbon*, *77*, 1183–1186.

97. Pouranfard, A. R., Mowla, D., & Esmaeilzadeh, F. (2015). An experimental study of drag reduction by nanofluids in slug two-phase flow of air and water through horizontal pipes. *Chinese Journal of Chemical Engineering*, *23*(3), 471–475.

98. Drzazga, M., Gierczycki, A., Dzido, G., & Lemanowicz, M. (2013). Influence of nonionic surfactant addition on drag reduction of water based nanofluid in a small diameter pipe. *Chinese Journal of Chemical Engineering*, *21*(1), 104–108.

99. Yanuar., Talahatu M.A., Mau, S., Waskito, K.T. Wulandari, W., (2017). The Effect of Calcium Carbonate ($CaCO_3$) Nanoparticles on the flow through a Pentagon Spiral Pipe. International Journal of Technology, Volume 8 (7), 1258-1265

100. Budi, K. & Samsul, K., Yanuar & Suhanan. (2015). A Modified Power Law Approach for Rheological Titania Nano fluids Flow Behavior in a Circular Conduit. Journal of Nanofluids. 4(2), 187-195.

101. Einstein, A. (1906). A new determination of molecular dimensions. *Annalen Der Physik, 19, 289-306.*

102. Mohsenipour, A.A. (2011). Turbulent drag reduction by polymers, surfactants and their mixtures in pipeline flow (Doctoral dissertation, University of Waterloo, Canada).

Appendix A: Experimental Data

6.1 Flow loop data:

Flow loop experiments included the calibration of the pipeline test section and experiments with dilute suspensions as mentioned under:

6.1.1 Calibration of flow loop:

As mentioned earlier, pipeline flow loop was calibrated with water as a flowing liquid. Flow rate in pipes could be estimated by the Calibration equation (equation no. 32) of Coriolis digital flowmeter by using V_1 (mV) voltage. The corresponding pressure drop in the pipeline were obtained using voltage readings V_2, V_3 and V_0 of channels 2, 3 and 0 respectively using the equations given in Table 4. The flow rate and pressure drop values thus measured were used to calculate and plot friction factor vs Reynolds number and this plot was compared with the standard Blasius line to check if data meets the theoretically expected values for water. The data (Table A1) showed good agreement with theoretical Blasius line. The table listing the calibration data obtained is given below:

Table A1: Flow data for water in pipeline system

Pipe Dia.	V_1 (mV)	$\dot{M}$ (kg/h)	Q (m³/sec)	Re	V (mV)	Channel	ΔP (Pa)	f
	1.136	744.74	0.0002072	11967.95	1.686	2	715.89	0.008737
	1.162	894.07	0.0002488	14367.64	1.923	2	915.35	0.007751
	1.18	997.45	0.0002776	16028.97	2.098	2	1062.64	0.007230
	1.196	1089.35	0.0003032	17505.71	2.239	2	1181.31	0.006738
	1.21	1169.76	0.0003255	187097.85	2.41	2	1325.22	0.006556
	1.222	1238.68	0.0003447	19905.40	2.544	2	1438.00	0.006344
1 inch	1.225	1225.91	0.0003495	20182.29	2.59	2	1476.71	0.006337
	1.237	1324.83	0.0003687	21289.84	2.747	2	1608.85	0.006205
	1.251	1405.24	0.0003911	22581.98	2.936	2	1767.91	0.006060
	1.608	3455.65	0.0009618	55531.64	2.105	2	1068.53	0.005971
	1.655	3725.59	0.0010369	59869.55	2.305	2	1236.85	0.005946
	1.704	4007.02	0.0011152	64392.05	2.605	2	1489.34	0.006190
	1.843	4805.36	0.0013374	77221.18	2.963	2	1790.64	0.005175

	1.947	5402.67	0.0015037	86819.96	3.688	2	2400.81	0.005489
	1.970	5534.77	0.0015405	88942.77	3.443	2	2194.61	0.004781
	1.971	5540.52	0.0015421	89035.06	3.637	2	2357.89	0.005126
	2.286	7349.70	0.0020456	118108.3	1.427	3	3536.09	0.004368
	3.059	11789.38	0.0032810	189453.1	2.011	3	8600.48	0.004129
	3.597	14879.35	0.0041410	239108.3	2.541	3	13196.60	0.003978
1.5 inch	1.426	2410.34	0.0006708	24509.12	1.616	2	656.98	0.007546
	1.461	2611.36	0.0007268	26553.16	1.714	2	739.46	0.007236
	1.511	2898.53	0.0008067	29473.21	1.839	2	844.66	0.006708
	1.574	3260.37	0.0009074	33152.48	2.035	2	1009.62	0.006337
	1.608	3455.65	0.0009618	35138.12	2.105	2	1068.53	0.005971
	1.655	3725.59	0.0010369	37882.97	2.305	2	1236.85	0.005946
	1.704	4007.02	0.0011152	40744.62	2.605	2	1489.34	0.006189
	1.843	4805.35	0.0013374	48862.36	2.963	2	1790.64	0.005174
	1.971	5540.52	0.0015421	56377.70	3.637	2	2357.89	0.005125
	2.286	7349.70	0.0020456	74734.03	1.427	3	3536.09	0.004368
	2.670	9555.18	0.0026595	97160.04	1.689	3	5808.13	0.004245
	3.059	11789.38	0.0032813	119878.05	2.011	3	8600.48	0.004129
	3.252	12897.86	0.0035899	131149.45	2.243	3	10612.36	0.004256
	3.597	14879.35	0.0041414	151297.81	2.541	3	13196.59	0.003977
	3.961	16969.96	0.0047233	172555.80	3.033	3	17463.17	0.004046
	4.138	17986.55	0.0050062	182892.78	3.172	3	18668.56	0.003850
	4.604	20662.99	0.0057512	210107.68	3.876	3	24773.58	0.003871
0.5 inch	1.079	417.37	0.0001161	15628.56	4.279	2	2898.21	0.004099
	1.086	457.57	0.0001273	17134.01	4.973	2	3482.29	0.004098
	1.092	492.03	0.0001369	18424.40	1.498	3	4151.80	0.004225
	1.097	520.75	0.0001449	19499.72	1.559	3	4680.78	0.004253
	1.101	543.72	0.0001513	20359.98	1.614	3	5157.74	0.004298
	1.103	555.21	0.0001545	20790.11	1.636	3	5348.52	0.004275
	1.195	1083.61	0.0003016	40576.01	3.226	3	19136.85	0.004015

	1.215	1198.48	0.0003335	44877.30	3.658	3	22883.11	0.003925
	1.229	1278.88	0.0003559	47888.19	4.002	3	25866.25	0.003896
	1.254	1422.47	0.0003959	53264.80	4.608	3	31121.42	0.003789
	1.278	1560.31	0.0004342	58426.34	3.173	0	37700.05	0.003815
	1.299	1680.92	0.0004678	62942.69	3.474	0	42948.55	0.003745
	1.321	1807.28	0.0005030	67674.10	3.876	0	49958.17	0.003768
	1.346	1950.87	0.0005429	73050.71	4.238	0	56270.31	0.003643
	1.359	2025.53	0.0005637	75846.54	4.445	0	59879.74	0.003596
	1.366	2065.73	0.0005749	77351.99	4.703	0	64378.45	0.003717

Where V_1 is the voltage reading of channel 1, $\dot{M}$ is the mass flow rate of liquid, Q is the volumetric flow rate of fluid, Re is the Reynolds number, V is the voltage reading used to find pressure drop, ΔP is the pressure drop across the pipeline test section and f is the fanning friction factor.

6.1.2 Dilute suspension flow data:

The flow loop experiments were done with three different concentrations of Silica nanoparticle suspensions i.e. 0.50, 0.75 and 1 wt.% respectively. Flow rate could be obtained by using the calibration equation 32 for Coriolis flowmeter. The corresponding pressure drop in the pipeline were obtained using voltage readings V_2, V_3 and V_0 of channels 2, 3 and 0 respectively using the equations given in Table 4. The flow rate and pressure drop values thus measured were used to calculate and plot friction factor vs Reynolds number and this plot was compared with the water line to see if the suspension has drag reduction properties or not. A detailed data processing approach has been given in the next section. The table no A2, A3, A4 and A5 given below list down the flow data obtained for 0.50, 0.75,1 and 2 wt.% suspensions:

Table A2: Flow data for 0.50 wt.% suspensions

Pipe Dia.	V_1 (mV)	$\dot{M}$ (kg/h)	Q (m³/sec)	Re	V (mV)	Channel	ΔP (Pa)	f
1 inch	1.284	1594.77	0.0004437	24881.31	3.086	2	24881.31	0.005043
	1.479	2714.74	0.0007553	42354.81	1.621	3	42354.81	0.004794
	1.624	3547.54	0.0009870	55347.93	1.985	3	55347.93	0.004506
	1.693	3943.84	0.0010972	61530.86	2.171	3	61530.86	0.004348
	1.711	4047.22	0.001126	63143.80	2.214	3	63143.80	0.004283

	1.869	4954.68	0.0013785	77301.82	2.765	3	77301.82	0.004175
	2.292	7384.16	0.0020544	115205.89	4.572	3	115205.89	0.003826
	2.953	11180.57	0.0031106	174436.58	4.887	0	174436.58	0.003661
	3.534	14517.51	0.0040391	226498.66	7.203	0	226498.66	0.003469
	3.618	14999.96	0.0041733	234025.71	7.572	0	234025.71	0.003443
1.5 inch	1.509	2887.05	0.0008032	28501.37	1.237	2	338.00	0.002707
	1.719	4093.17	0.0011388	40408.38	1.824	2	832.03	0.003315
	1.959	5471.59	0.0015223	54016.39	2.843	2	1689.64	0.0037676
	1.996	5684.10	0.0015814	56114.30	2.980	2	1804.94	0.003729
	2.018	5810.46	0.0016166	57361.70	3.114	2	1917.72	0.003791
	2.208	6901.71	0.0019202	68134.71	4.151	2	2790.48	0.003910
	2.761	10077.83	0.002803	99489.84	1.743	3	6276.41	0.004125
	3.659	15235.44	0.0042388	150406.48	2.570	3	13448.08	0.003867
	4.312	18985.91	0.0052823	187431.62	3.355	3	20255.52	0.003751
	4.799	21782.96	0.0060605	215044.54	4.002	3	25866.24	0.003639
0.5 inch	1.075	394.39	0.0010973	14338.16	2.585	2	1472.51	0.002333
	1.095	509.26	0.0001416	18514.17	4.373	2	2988.32	0.002829
	1.107	578.18	0.0001608	21019.77	1.459	3	3813.59	0.002811
	1.118	641.36	0.0001784	23316.57	1.587	3	4923.60	0.002950
	1.125	681.57	0.0001896	24778.17	1.687	3	5790.79	0.003072
	1.126	687.31	0.0001912	24986.97	1.682	3	5747.43	0.002998
	1.129	704.54	0.0001960	25613.37	1.725	3	6120.32	0.003039
	1.134	733.26	0.0002040	26657.37	1.818	3	6926.80	0.003175
	1.167	922.79	0.0002567	33547.78	2.276	3	10898.54	0.003154
	1.179	991.71	0.0002759	36053.38	2.470	3	12580.89	0.003152
	1.212	1181.24	0.0003286	42943.79	3.007	3	17237.70	0.003044
	1.221	1232.94	0.0003430	44822.99	3.236	3	19223.56	0.003116
	1.295	1657.95	0.0004612	60274.21	3.116	0	36706.15	0.003291

Table A3: Flow data for 0.75 wt.% suspensions

Pipe Dia.	V_1 (mV)	$\dot{M}$ (kg/h)	Q (m³/sec)	Re	V (mV)	Channel	ΔP (Pa)	f
1 inch	1.413	2335.68	0.0006482	34121.75	1.482	3	4013.05	0.004993
	1.580	3294.83	0.0009145	48133.95	1.878	3	7447.12	0.004656
	1.585	3323.55	0.0009224	48553.48	1.88	3	7464.46	0.004586
	1.651	3702.61	0.0010276	54091.23	2.059	3	9016.73	0.004464
	1.678	3857.69	0.0010707	56356.68	2.145	3	9762.52	0.004452
	1.735	4185.06	0.0011615	61139.29	2.34	3	11453.54	0.004438
	2.26	7200.37	0.0019985	105189.62	4.481	3	30020.08	0.003930
	2.851	10594.74	0.0029406	154777.72	4.58	0	62233.71	0.003763
	3.024	11588.36	0.0032164	169293.35	5.139	0	71980.92	0.003638
	3.548	14597.92	0.0040517	213259.78	7.318	0	109975.84	0.003503
	3.606	14931.04	0.0041441	218126.30	7.608	0	115032.53	0.003502
1.5 inch	1.452	2559.67	0.0007104	23661.41	1.244	2	343.90	0.003512
	1.553	3139.76	0.0008714	29023.69	1.493	2	553.46	0.003756
	1.69	3926.61	0.0010898	36297.27	1.842	2	847.18	0.003676
	1.836	4765.15	0.0013225	44048.69	2.352	2	1276.41	0.003761
	1.923	5264.83	0.0014612	48667.68	2.753	2	1613.90	0.003896
	1.966	5511.80	0.0015298	50950.63	2.971	2	1797.37	0.003959
	1.997	5689.84	0.0015792	52596.48	3.124	2	1926.14	0.003981
	2.05	5994.252	0.0016637	55410.35	3.407	2	2164.32	0.004030
	2.145	6539.87	0.0018151	60454.07	3.9	2	2579.23	0.004035
	2.834	10497.10	0.0029135	97034.37	1.799	3	6762.04	0.004106
	4.788	21719.79	0.0060284	200775.88	3.963	3	25528.04	0.003621
0.5 inch	1.08	423.11	0.0001174	14403.29	3.216	2	2003.57	0.002765
	1.086	457.57	0.0001270	15576.37	3.636	2	2357.05	0.002781
	1.103	555.21	0.0001541	18900.09	1.471	3	3917.65	0.003139
	1.113	612.64	0.0001700	20855.22	1.584	3	4897.58	0.003223
	1.115	624.13	0.0001732	21246.25	1.615	3	5166.41	0.003276

	1.14	767.72	0.0002130	26134.07	1.965	3	8201.57	0.003438
	1.172	951.51	0.0002640	32390.48	2.467	3	12554.87	0.003426
	1.243	1359.29	0.0003772	46271.90	3.872	3	24738.9	0.003308

Table A4: Flow data for 1 wt.% suspensions

Pipe Dia.	V$_1$ (mV)	$\dot{M}$ (kg/h)	Q (m^3/sec)	Re	V (mV)	Channel	ΔP (Pa)	f
1 inch	1.407	2301.22	0.000636	32438.72	1.462	3	3839.61	0.004938
	1.584	3317.80	0.000917	46768.88	1.888	3	7533.84	0.004661
	1.637	3622.21	0.001001	51059.84	2.023	3	8704.55	0.004518
	2.01	5764.51	0.001594	81258.42	3.398	3	20628.41	0.004228
	2.41	8061.89	0.002230	113642.96	3.292	0	39775.04	0.004168
	2.645	9411.59	0.002603	132668.88	4.03	0	52643.44	0.004047
	2.787	10227.16	0.002828	144165.39	4.467	0	60263.35	0.003924
	3.056	11772.15	0.003256	165944.00	5.446	0	77334.03	0.003800
	3.381	13638.77	0.003772	192256.44	6.774	0	100490.18	0.003679
	3.538	14540.49	0.004022	204967.37	7.519	0	113480.64	0.003655
1.5 inch	1.545	3093.81	0.000855	27595.48	1.9	2	896.00	0.006285
	1.727	4139.12	0.001144	36919.16	2.587	2	1474.19	0.005777
	1.841	4793.87	0.001326	42759.26	3.014	2	1833.56	0.005357
	1.901	5138.47	0.001421	45833.00	3.298	2	2072.58	0.005270
	1.927	5287.80	0.001462	47164.96	3.397	2	2155.90	0.005177
	2.303	7447.34	0.002060	66427.06	1.446	3	3700.86	0.004480
	2.66	9497.75	0.002627	84715.81	1.686	3	5782.11	0.004303
	2.886	10795.76	0.002986	96293.56	1.86	3	7291.02	0.004200
	3.109	12076.55	0.003340	107717.63	2.049	3	8930.01	0.004111
	3.526	14471.56	0.004003	129080.12	2.471	3	12589.56	0.004036
	3.94	16849.35	0.004660	150288.92	2.947	3	16717.38	0.003953
	4.365	19290.31	0.005336	172061.25	3.491	3	21434.90	0.003867
	4.526	20215.00	0.005591	180309.12	3.693	3	23186.62	0.003809
	1.055	279.52	7.732E-05	9181.59	2.388	2	1306.71	0.004145

Pipe Dia.	V_1 (mV)	$\dot{M}$ (kg/h)	Q (m³/sec)	Re	V (mV)	Channel	ΔP (Pa)	f
	1.068	354.19	9.797E-05	11634.08	3.255	2	2036.39	0.004024
	1.122	664.33	0.000183	21821.33	1.892	3	7568.53	0.004251
0.5	1.195	1083.61	0.0002997	35592.99	3.183	3	18763.95	0.003961
inch	1.326	1836.00	0.0005078	60306.51	3.798	0	48598.09	0.003574
	1.339	1910.66	0.0005285	62758.99	4.086	0	53619.90	0.003641
	1.356	2008.30	0.0005555	65966.09	4.283	0	57054.96	0.003506
	1.363	2048.50	0.0005666	67286.66	4.403	0	59147.39	0.003494

Table A5: Flow data for 2 wt.% suspensions

Pipe Dia.	V_1 (mV)	$\dot{M}$ (kg/h)	Q (m³/sec)	Re	V (mV)	Channel	ΔP (Pa)	f
	1.444	2513.72	0.0006927	28771.43	1.551	3	4611.41	0.004989
	1.517	2932.99	0.0008082	33570.30	1.722	3	6094.30	0.004843
	1.793	4518.18	0.0012450	51713.94	2.597	3	13682.22	0.004582
1	2.038	5925.33	0.0016328	67819.72	3.651	3	22822.40	0.004444
inch	2.389	7941.27	0.0021884	90893.70	3.231	0	38711.39	0.004196
	3.241	12834.68	0.0035368	146902.35	6.169	0	89940.88	0.003732
	3.473	14167.16	0.0039040	162153.54	7.312	0	109871.21	0.003742
	1.325	1830.258	0.0005043	13255.42	1.387	2	464.25	0.009340
	1.654	3719.84	0.0010250	26940.57	2.34	2	1266.31	0.006168
	1.742	4225.27	0.0011643	30601.04	2.625	2	1506.17	0.005686
	1.846	4822.59	0.0013289	34927.04	3.098	2	1904.26	0.005518
1.5	1.906	5167.19	0.0014239	37422.81	3.357	2	2122.23	0.005357
inch	1.941	5368.21	0.0014793	38878.68	3.532	2	2269.52	0.005307
	1.959	5471.59	0.0015078	39627.41	3.638	2	2358.73	0.005310
	3.628	15057.40	0.0041494	109051.46	2.592	3	13638.86	0.004054
	4.618	20743.40	0.0057163	150231.69	3.861	3	24643.50	0.003860
	1.075	394.39	0.0001097	14338.16	2.585	2	1472.51	0.002333
0.5	1.095	509.26	0.0001416	18514.16	4.373	2	2977.32	0.002829
inch	1.107	578.18	0.0001608	21019.76	1.459	3	3813.59	0.002811
	1.118	641.36	0.0001784	23316.57	1.587	3	4923.60	0.002950

	1.125	681.57	0.0001896	24778.17	1.687	3		5790.79	0.003072
	1.126	687.31	0.0001912	24986.97	1.682	3		5747.43	0.002998
	1.129	704.54	0.0001960	25613.37	1.725	3		6120.32	0.003039
	1.134	733.26	0.0002040	26657.37	1.818	3		6926.80	0.003175
	1.167	922.79	0.0002567	33547.78	2.276	3		10898.54	0.003154
	1.179	991.71	0.0002759	36053.38	2.47	3		12580.89	0.003152
	1.212	1181.24	0.0003286	42943.78	3.007	3		17237.70	0.003044
	1.221	1232.94	0.0003430	44822.99	3.236	3		19223.56	0.003116

6.1.3 Calculation approach:

The Voltage V_1 represents the voltage signal from Channel 1 that is used to estimate the flow rate, Voltage V_2 represent the voltage signal of 0-0.5 psi pressure transducer, V_3 represent the voltage signal of 0-5 psi pressure transducer and V_0 represent the voltage signal of 0-10 psi pressure transducer. The voltage signals V_2, V_3 and V_0 are used to estimate the pressure drop across the test section of the pipelines. For measuring the flow rate (kg/s), we use the Voltage V_1 (mV) and substitute in the following equation:

$$y = 1.5954\, x - 1.6055$$

The flow rate thus obtained has units of kg/s and is multiplied by a factor of 3600 to convert the units to kg/h and hence obtain and then is divided by the density of the flowing fluid to get the volumetric flow rate, Q. To calculate the pressure drop (psi), following equations are used:

For measuring the pressure drop (psi) using Voltage reading given from channel 2, we use:

$$\Delta P = 0.1221 * V_2 - 0.102$$

For measuring the pressure drop (psi) using voltage reading given from channel 3, we use:

$$\Delta P = 1.2581 * V_3 - 1.2823$$

For measuring the pressure drop (psi) using voltage reading given from channel 0, we use:

$$\Delta P = 2.5297 * V_2 - 2.5573$$

To calculate the Reynolds number, we use the following equation:

$$Re = \frac{4\rho Q}{\pi \mu D}$$

Where ρ and μ are the density and dynamic viscosity of the flowing fluid, D is the diameter of the pipe and Q is the volumetric flow rate. To find the Fanning friction factor f, we use:

$$f = \frac{\Delta P * D}{2 * L * \rho * V^2}$$

Where L is length of the pipeline and V is the velocity of the fluid, ρ, ΔP and D as stated above.

6.2 Density and volume fraction data:

The density and volume fraction of dilute silica suspensions was obtained as under:

6.2.1 Measurement of density:

The density of dilute suspensions was measured using a basic weight and volume measurement technique. A conical volumetric flask was used for this process. The weight W_1 of empty conical flask was measured before filling it with the dilute suspension. Then, another measurement W_2 was taken after filling the flask precisely to 50 ml marking with the suspension. The difference between these two measurements would give the actual weight of 50 ml volume of suspension.

$$Density, \rho \left(\frac{g}{ml}\right) = \frac{W_2 - W_1}{50}$$

The density results obtained for S13, T30 and N20 Silica nanoparticle suspensions are:

Table A6: Density of silica nanoparticle suspensions

S13							
Concentration (wt.%)	0.50	0.75	1	2	3	4	5	6
Density (g/cm³)	0.998	1.0008	1.0042	1.008	1.0132	1.0196	1.025	1.0296

T30			
Concentration (wt.%)	1	2	3	4
Density (g/cm³)	1.0012	1.0061	1.0113	1.0194

N20				
Concentration (wt.%)	1	2	3	4	5
Density (g/cm³)	1.0010	1.0068	1.0107	1.0178	1.0268

6.2.2 Conversion of weight fraction to volume fraction:

The volume fraction, ϕ of particles in suspension can be obtained from weight fraction, x, density of suspension $\rho_{suspension}$ and density of nanoparticles ρ_{np} using the following formula:

$$\phi = \frac{x \times \rho_{suspension}}{\rho_{np}}$$

Where ρ_{np} was obtained as follows:

The total volume of suspension, V_T can be written as sum of volume occupied by Nanoparticles (V_{np}) and the continuous phase (V_C) as:

$$V_T = V_{np} + V_C$$

In terms of Volume and density, this can also be written as:

$$\frac{M_{susp}}{\rho_{susp}} = \frac{M_{np}}{\rho_{np}} + \frac{M_C}{\rho_C}$$

Where M_{susp}, M_{np} and M_C are the mass of suspension, nanoparticles and continuous phase respectively and ρ_{susp}, ρ_{np} and ρ_C are the density of suspension, nanoparticle and continuous phase respectively. Dividing the above equation by M_{susp}, we get:

$$\frac{1}{\rho_{susp}} = \frac{x}{\rho_{np}} + \frac{1-x}{\rho_C}$$

Where x is the mass fraction of silica nanoparticles in the suspension. Rearranging, we get:

$$\rho_C = \rho_{np}\left[1 + \frac{1}{x}\left(\frac{\rho_C}{\rho_{susp}} - 1\right)\right]$$

So ρ_{np} can be obtained by finding slope of the above given line. The continuous phase for silica suspensions was water and hence, ρ_C is 0.998 g/ml. Also, the values of ρ_{np} thus obtained are:

Table A7: Density of silica nanoparticles

Silica grade	S13	T30	N20
ρ_{np} (g/ml)	2.062	1.905	2.005

Using these density values given in Table A7, the volume fraction obtained for particles is

Table A8: Volume fraction of silica nanoparticle suspensions

S13							
Weight fraction	0.0050	0.0075	0.01	0.02	0.03	0.04	0.05	0.06
Volume fraction	0.00241	0.00363	0.00486	0.00977	0.0147	0.0197	0.02484	0.0299

T30				
Weight fraction	0.01	0.02	0.03	0.04
Volume fraction	0.005253	0.01055	0.01592	0.02139

N20					
Weight fraction	0.01	0.02	0.03	0.04	0.05
Volume fraction	0.00499	0.01004	0.001512	0.02030	0.02560

6.3 Viscosity of dilute silica suspensions:

The viscosity of dilute silica suspensions was measured by CANNON Ubbelhoode viscometer. The experimental results are shown below in the table:

Table A9: Viscosity (cP) of different grades of silica nanoparticle suspensions

S13								
Concentration (wt.%)	0.50	0.75	1	2	3	4	5	6
Viscosity (cP)	1.03	1.10	1.14	1.404	1.597	2.062	2.467	3.238

T30				
Concentration (wt.%)	1	2	3	4
Viscosity (cP)	1.13	1.396	1.745	2.685

N20					
Concentration (wt.%)	1	2	3	4	5
Viscosity (cP)	1.201	1.854	2.566	3.562	4.70

Table A10: Viscosity (cP) of S13 silica nanoparticle suspensions at room temperature

Viscosity (cP)								
Concentration	Without electrolyte presence				With electrolyte (0.1 M NaCl)			
	pH=1	pH=2	pH=4	pH=7	pH=1	pH=2	pH=4	pH=7
0.50 wt. %	1.0047	0.9960	0.9960	0.9982	1.0330	1.0461	1.0243	1.0025
0.75 wt. %	1.0399	1.0224	1.0312	1.0224	1.1185	1.0486	0.9831	1.0486

1 wt. %	1.1355	1.0741	1.0632	1.0522	1.1574	1.1925	1.0960	1.0434
2 wt. %	1.4170	1.3202	1.2762	1.2366	1.3510	1.4038	1.4303	1.4170
3 wt. %	1.8933	1.7030	1.7561	1.5925	2.4064	1.7517	1.8269	1.6234
4 wt. %	1.9720	1.9275	2.0121	1.9854	2.4172	2.6709	3.1739	--
5 wt. %	2.2733	2.4658	3.9828	2.9625	4.8443	2.6224	--	--

Table A11: Viscosity (cP) of S13 silica nanoparticle suspensions at 40 ℃

Viscosity (cP)								
	Without electrolyte presence				In the presence of an electrolyte (0.1 M NaCl)			
Concentration	pH=1	pH=2	pH=4	pH=7	pH=1	pH=2	pH=4	pH=7
1 wt. %	0.7891	0.7847	0.7804	0.7453	0.8198	0.8461	0.8111	--
2 wt. %	1.0785	1.0610	0.9996	1.1486	0.9645	0.9601	1.082	--
3 wt. %	1.3898	1.0610	1.1618	1.0040	1.5082	1.4731	1.5695	--
4 wt. %	1.4205	1.4555	1.4687	1.4029	1.5564	1.4073	2.8059	--
5 wt. %	1.7361	1.8984	2.8761	1.7142	3.1479	1.7318	--	--

6.4   Rheological data:

The Rheology data was measured using Fann model 35 viscometer and Haake Rotovisco RV 12 viscometers. The room temperature experiments were done with Fann viscometer and the experiments with elevated temperatures were done with Haake as mentioned under:

6.4.1 Calibration of Haake viscometer:

According to the equipment manual, shear stress, shear rate and apparent viscosity can be measured using the following formulas:

$$Shear\ rate = M \times n$$

$$Viscosity = \frac{G \times S}{n}$$

$$Shear\ stress = A \times S$$

Where n is rpm of the rotor bob, S is the digital reading, G is the instrument factor, A is the shear stress factor and M is the shear rate factor. Before using HAAKE for temperature experiments, it was calibrated with standard fluid of viscosity, μ=97.5 cP and the following data was obtained:

Table A12: Calibration data of Haake viscometer

n (rpm)	Shear rate (s⁻¹)	μ*n	S, Digital reading
16	37.44	1560	4.81
25.6	59.904	2496	7.783
32	74.88	3120	9.516
51.2	119.808	4992	15.38
64	149.76	6240	18.967
128	299.52	12480	38.55
256	599.04	24960	77.25

The value of M is constant and is given as 2.34 (minute/sec). The value of G was obtained by finding the slope for a linear regression of μ*N (on vertical axis) vs S value (on horizontal axis). The value of A was obtained by using the following formula:

$$A = 0.001 \times G \times M$$

After the calibration, the values of parameters G, A and M obtained are given below:

Table A13: Values of different constants of HAAKE viscometer

Parameter	G (mPa*s/Scale grad*min)	A (Pa/Scale grade)	M (minute/sec)
Value	323.7	0.757	2.34

6.4.2 Rheological data obtained with Haake viscometer:

The rheological data obtained with Haake viscometer for temperature experiments is:

Table A14: Shear stress vs shear rate for S13 (15 wt. %) at different temperatures

Temperature	n (RPM)	S (Digital output)	Viscosity (cP)	Shear rate (s⁻¹)	Shear stress (mPa)
22°C	25.6	1.083	13.694	59.904	819.83

	32	1.13	11.430	74.88	855.41
	51.2	1.63	10.305	119.808	1233.91
	64	1.716	8.679	149.76	1299.01
	128	2.83	7.156	299.52	2142.31
	256	4.96	6.271	599.04	3754.72
34°C	25.6	0.9166	11.589	59.904	693.866
	32	0.966	9.771	74.88	731.26
	51.2	1.4	8.851	119.808	1059.8
	64	1.616	8.173	149.76	1223.3
	128	2.566	6.489	299.52	1942.46
	256	4.35	5.500	599.04	3292.95
40°C	25.6	0.916	11.582	59.904	693.41
	32	0.8833	8.93	74.88	668.65
	51.2	1.27	8.029	119.808	961.39
	64	1.4	7.08	149.76	1059.8
	128	2.25	5.6900	299.52	1703.25
	256	3.916	4.951	599.04	2964.41
50°C	25.6	0.8	10.115	59.904	605.6
	32	0.866	8.760	74.88	655.56
	51.2	1.15	7.270	119.808	870.55
	64	1.31	6.625	149.76	991.67

Temperature	n (RPM)	S (Digital output)	Viscosity (cP)	Shear rate (s⁻¹)	Shear stress (mPa)
	128	2.1	5.310	299.52	1589.7
	256	3.55	4.488	599.04	2687.35
60°C	25.6	0.67	8.471	59.904	507.19
	32	0.7	7.080	74.88	529.9
	51.2	1.016	6.423	119.808	769.11
	64	1.13	5.715	149.76	855.41
	128	1.816	4.594	299.52	1375.16
	256	3.15	3.983	599.04	2384.55

Table A15: Shear stress vs shear rate for T30 (15 wt. %) at different temperatures

Temperature	n (RPM)	S (Digital output)	Viscosity (cP)	Shear rate (s⁻¹)	Shear stress (mPa)
22°C	25.6	2.116	26.755	59.90	1601.81
	32	2.35	23.771	74.88	1778.95
	51.2	3.483	22.020	119.80	2636.63
	64	3.86	19.523	149.76	2922.02
	128	6.38	16.134	299.52	4829.66
	256	10.81	13.668	599.04	8183.17
34°C	25.6	1.93	24.403	59.904	1461.01
	32	2.13	21.546	74.88	1612.41
	51.2	3.066	19.384	119.80	2320.96
	64	3.48	17.601	149.76	2634.36
	128	5.65	14.288	299.52	4277.05

	256	9.366	11.842	599.04	7090.06
40°C	25.6	1.783	22.545	59.904	1349.73
	32	2.066	20.898	74.88	1563.96
	51.2	2.83	17.892	119.80	2142.31
	64	3.316	16.771	149.76	2510.21
	128	5.3	13.403	299.52	4012.1
	256	8.78	11.101	599.04	6646.46
50°C	25.6	1.9	24.024	59.904	1438.3
	32	2.01	20.393	74.88	1526.11
	51.2	2.98	18.840	119.80	2255.86
	64	3.33	16.842	149.76	2520.81
	128	5.28	13.352	299.52	3996.96
	256	8.5	10.747	599.04	6434.5

Table A16: Shear stress vs shear rate for N20 (8 wt. %) at different temperatures

Temperature	n (RPM)	S (Digital output)	Viscosity (cP)	Shear rate (s⁻¹)	Shear stress (mPa)
22°C	25.6	0.6333	8.008	59.90	479.43
	32	0.65	6.575	74.88	492.05
	51.2	0.9	5.690	119.80	681.3
	64	1.016	5.142	149.76	769.61
	128	1.666	4.214	299.52	1261.66
	256	2.883	3.645	599.04	2182.68

	25.6	0.633	8.008	59.90	479.43
	32	0.65	6.575	74.88	492.05
34°C	51.2	0.9	5.690	119.80	681.3
	64	1.016	5.142	149.76	769.61
	128	1.666	4.214	299.52	1261.66
	256	2.833	3.582	599.04	2144.83
	25.6	0.7	8.851	59.904	529.9
	32	0.716	7.249	74.88	542.51
40°C	51.2	0.9	5.690	119.80	681.3
	64	1.05	5.310	149.76	794.85
	128	1.666	4.214	299.52	1261.66
	256	2.833	3.582	599.04	2144.83
	25.6	0.666	8.429	59.90	504.66
	32	0.683	6.912	74.88	517.28
50°C	51.2	0.85	5.373	119.808	643.45
	64	0.95	4.804	149.76	719.15
	128	1.6	4.046	299.52	1211.2
	256	2.616	3.308	599.04	1980.81
	25.6	0.616	7.797	59.904	466.81
60°C	32	0.633	6.406	74.88	479.43
	51.2	0.8	5.057	119.808	605.6

	64	0.9	4.552	149.76	681.3
	128	1.4	3.540	299.52	1059.8
	256	2.4	3.034	599.04	1816.8

6.4.3 Calibration of Fann viscometer:

Before using Fann viscometer, it was calibrated with standard fluids of viscosity 9.8 cP and 97.5 cP. The readings obtained for calibration are as follows:

Table A17: Calibration data of Fann viscometer

Standard fluid	N (RPM)	Shear rate (s⁻¹)	Dial Reading	Shear stress (mPa)
97.5 cP	6	10.2	12	994.5
	30	51	56	4972.5
	60	102	110	9945
	90	153	165	14917.5
	100	170	180	16575
9.8 cP	90	153	18	1499.4
	100	170	21	1666
	180	306	34	2998.8
	200	340	38	3332
	300	510	56	4998

The Shear rate and shear stress could be measured using the following formulas:

$$Shear\ rate = k \times RPM$$

$$Shear\ stress = \mu \times Shear\ rate$$

Where μ is the dynamic viscosity of the standard fluid used and k is spring constant which is a constant for the given geometry i.e. k=1.7. Also, the calibration equation of Fann viscometer was found by a linear regression of Shear stress data vs Dial reading and the equation obtained was:

$$Shear\ stress\ (mPa) = 92.509\ \times (Dial\ Reading) - 175.23$$

6.4.4 Rheological data obtained with Haake viscometer:

The rheological data for S13, T30 and N20 suspensions is given in the tables 13, 14 and 15 below:

Table A18: Rheological data for S13 suspensions at Room Temperature (22°C)

Concentration (wt. %)	RPM	Dial Reading	Shear rate (s^{-1})	Shear stress (mPa)	Viscosity (cP)
6 wt.%	180	15	306	1212.405	3.962
	200	16	340	1304.914	3.837
	300	20	510	1674.95	3.2842
	600	33	1020	2877.567	2.821
7 wt.%	180	17	306	1397.42	4.566
	200	18	340	1489.93	4.382
	300	24	510	2044.98	4.009
	600	39	1020	3432.62	3.365
8 wt. %	180	20	306	1674.95	5.473
	200	22	340	1859.96	5.470
	300	29	510	2507.53	4.916
	600	47	1020	4172.69	4.090
9 wt.%	100	15	170	1212.40	7.131

	RPM	Dial Reading	Shear rate (s⁻¹)	Shear stress (mPa)	Viscosity (cP)
	180	21	306	1767.46	5.776
	200	23	340	1952.47	5.742
	300	30	510	2600.04	5.098
	600	49	1020	4357.71	4.272
10 wt. %	100	16	170	1304.91	7.675
	180	24	306	2044.98	6.682
	200	25	340	2137.49	6.286
	300	32	510	2785.05	5.460
	600	52	1020	4635.23	4.544
15 wt.%	100	44	170	3895.16	22.912
	180	61	306	5467.81	17.868
	200	64	340	5745.34	16.898
	300	80	510	7225.49	14.167
	600	123	1020	11203.37	10.983
20 wt. %	100	76	170	6855.45	40.326
	180	106	306	9630.72	31.472
	200	112	340	10185.77	29.958
	300	140	510	12776.03	25.051
	600	220	1020	20176.75	19.781

Table A19: Rheological data for T30 suspensions at room temperature (22°C)

Concentration (wt. %)	RPM	Dial Reading	Shear rate (s⁻¹)	Shear stress (mPa)	Viscosity (cP)

	180	17	306	1397.42	4.566
	200	19	340	1582.44	4.654
5 wt.%	300	24	510	2044.98	4.009
	600	40	1020	3525.13	3.456
	180	24	306	2044.98	6.682
	200	26	340	2230.00	6.558
6 wt.%	300	33	510	2877.56	5.642
	600	52	1020	4635.23	4.544
	180	32	306	2785.05	9.101
	200	34	340	2970.07	8.735
7 wt.%	300	41	510	3617.63	7.093
	600	60	1020	5375.31	5.269
	100	35	170	3062.6	18.015
	180	49	306	4357.71	14.240
8 wt.%	200	51	340	4542.73	13.360
	300	64	510	5745.34	11.265
	100	36	170	3155.09	18.559
	180	51	306	4542.73	14.845
9 wt.%	200	53	340	4727.74	13.905
	300	68	510	6115.38	11.990
	600	102	1020	9260.68	9.079

	100	52	170	4635.24	27.266
	180	76	306	6855.45	22.403
10 wt.%	200	77	340	6947.96	20.435
	300	98	510	8890.65	17.432
	600	156	1020	14256.17	13.976

Table A20: Rheological data for N20 suspensions at room temperature (22°C)

Concentration (wt. %)	RPM	Dial Reading	Shear rate (s^{-1})	Shear stress (mPa)	Viscosity (cP)
	100	15	170	1212.40	7.131
	180	20	306	1674.95	5.473
6 wt.%	200	22	340	1859.96	5.470
	300	28	510	2415.022	4.735
	600	44	1020	3895.16	3.818
	90	16	153	1304.91	8.528
	180	24	306	2044.98	6.683
7 wt.%	200	25	340	2137.49	6.286
	300	32	510	2785.05	5.460
	600	50	1020	4450.22	4.363
	100	22	170	1859.96	10.941
	180	31	306	2692.55	8.799
8 wt.%	200	33	340	2877.56	8.463
	300	42	510	3710.14	7.274

	600	66	1020	5930.36	5.814
	100	26	170	2230.00	13.117
	180	37	306	3247.60	10.613
9 wt.%	200	38	340	3340.11	9.823
	300	48	510	4265.20	8.3631
	600	77	1020	6947.96	6.811
	100	49	170	4357.71	25.633
	180	73	306	6577.93	21.496
10 wt.%	200	72	340	6485.42	19.074
	300	88	510	7965.56	15.618
	600	148	1020	13516.10	13.251

6.5   Size distribution results:

The raw data of Intensity and Number distribution of 0.05, 0.50 and 1 wt.% silica nanoparticles are given:

Table A21: Intensity % data for silica nanoparticles

Size	Mean Intensity %								
	S13			T30			N20		
(d.nm)	0.05 wt.%	0.50 wt.%	1.0 wt.%	0.05 wt.%	0.50 wt.%	1.0 wt.%	0.05 wt.%	0.50 wt.%	1.0 wt.%
0.4	0	0	0	0	0	0	0	0	0
0.4632	0	0	0	0	0	0	0	0	0
0.5365	0	0	0	0	0	0	0	0	0
0.6213	0	0	0	0	0	0	0	0	0
0.7195	0	0	0	0	0	0	0	0	0
0.8332	0	0	0	0	0	0	0	0	0

0.9649	0	0	0	0	0	0	0	0	0
1.117	0	0	0	0	0	0	0	0	0
1.294	0	0	0	0	0	0	0	0	0
1.499	0	0	0	0	0	0	0	0	0
1.736	0	0	0	0	0	0	0	0	0
2.01	0	0	0	0	0	0	0	0	0
2.328	0	0	0	0	0	0	0	0	0
2.696	0	0	0	0	0	0	0	0	0
3.122	0	0	0	0	0	0	0	0	0
3.615	0	0	0	0	0	0	0	0	0
4.187	0	0	0	0	0	0	0	0	0
4.849	0	0	0	0	0	0	0	0	0
5.615	0	0	0	0	0	0	0	0	0
6.503	0	0	0	0	0	0	0	0	0
7.531	0	0	0	0	0	0	0	0	0
8.721	0	0	0	0	0	0	0	0	0
10.1	0	0	0	0	0	0	0	0	0
11.7	0	0	0	0	0	0	0	0	0
13.54	0	0	0	0	0	0	0	0	0
15.69	0	0	0	0	0	0	0	0	0
18.17	0	0	0	0	0	0	0	0	0
21.04	0	0	0	0	0	0	0	0	0
24.36	0	0	0	0	0	0	0	0	0
28.21	0	0	0	0	0	0	0	0	0
32.67	0	0	0	0	0	0	0	0	0
37.84	0	0	0	0	0	0	0	0	0
43.82	0	0	0	0	0	0	0	0	0
50.75	0	0	0	0	0.1	0	0	0	0
58.77	0	0	0	0	0.2	0.4	0	0	0
68.06	0	0	0	0.1	0.2	0.8	0	0	0

78.82	0	0	0	0.4	0.3	1.3	0	0	0
91.28	0	0	0.7	0.8	0.4	1.6	0	0	0
105.7	0	0	1.5	1.4	0.7	1.6	0	0.2	0.2
122.4	0.1	0.4	2.2	2.4	1.1	1.5	0	0.8	0.8
141.8	0.8	1.7	2.4	3.7	2.2	1.6	0	2.1	2.1
164.2	2.3	3.4	2.2	5.4	4.1	2.2	1.3	3.8	3.7
190.1	4.4	4.9	2.1	7.4	6.5	3.7	4.2	5.5	5.2
220.2	6.7	6	2.5	9.4	8.9	5.8	8.1	6.9	6.4
255	8.9	6.8	3.5	11	11	8.2	11.9	7.9	7.2
295.3	10.5	7.2	5.3	11.9	12.2	10.4	14.6	8.5	7.7
342	11.4	7.6	7.4	11.9	12.4	11.9	15.6	8.6	7.9
396.1	11.4	8	9.4	10.9	11.5	12.4	14.6	8.5	7.9
458.7	10.8	8.3	10.9	9.1	9.7	11.6	12.1	8.1	7.8
531.2	9.5	8.5	11.6	6.8	7.4	9.8	8.6	7.5	7.4
615.1	7.8	8.4	11.2	4.3	5	7.2	5.1	6.7	6.9
712.4	5.9	7.9	9.8	2.2	3	4.5	2.4	5.9	6.1
825	4.1	7	7.7	0.7	1.7	2.1	0.8	5	5.1
955.4	2.5	5.7	5.2	0	1	0.6	0.1	4	3.9
1106	1.3	4.1	2.9	0	0.5	0	0	3.1	2.8
1281	0.5	2.5	1.2	0	0.1	0	0	2.2	1.8
1484	0.1	1.2	0.3	0	0	0	0	1.6	1.2
1718	0	0.3	0	0	0	0	0	1.1	1.1
1990	0	0	0	0	0	0	0	0.8	1.2
2305	0	0	0	0	0	0	0	0.6	1.3
2669	0	0	0	0	0	0	0	0.4	1.2
3091	0	0	0	0	0	0	0	0.3	1.1
3580	0	0	0	0	0	0	0	0.1	0.9
4145	0	0	0	0	0	0	0	0.1	0.6
4801	0	0	0	0	0	0	0.2	0	0.4
5560	0	0	0	0	0	0	0.4	0	0.2

6439	0	0	0	0	0	0	0	0	0
7456	0	0	0	0	0	0	0	0	0
8635	0	0	0	0	0	0	0	0	0
1.00E+04	0	0	0	0	0	0	0	0	0

Table A22: Number % data for silica nanoparticles

Size (d.nm)	Mean Number %								
	S13			T30			N20		
	0.05 wt.%	0.50 wt.%	1.0 wt.%	0.05 wt.%	0.50 wt.%	1.0 wt.%	0.05 wt.%	0.50 wt.%	1.0 wt.%
0.4	0	0	0	0	0	0	0	0	0
0.4632	0	0	0	0	0	0	0	0	0
0.5365	0	0	0	0	0	0	0	0	0
0.6213	0	0	0	0	0	0	0	0	0
0.7195	0	0	0	0	0	0	0	0	0
0.8332	0	0	0	0	0	0	0	0	0
0.9649	0	0	0	0	0	0	0	0	0
1.117	0	0	0	0	0	0	0	0	0
1.294	0	0	0	0	0	0	0	0	0
1.499	0	0	0	0	0	0	0	0	0
1.736	0	0	0	0	0	0	0	0	0
2.01	0	0	0	0	0	0	0	0	0
2.328	0	0	0	0	0	0	0	0	0
2.696	0	0	0	0	0	0	0	0	0
3.122	0	0	0	0	0	0	0	0	0
3.615	0	0	0	0	0	0	0	0	0
4.187	0	0	0	0	0	0	0	0	0
4.849	0	0	0	0	0	0	0	0	0
5.615	0	0	0	0	0	0	0	0	0
6.503	0	0	0	0	0	0	0	0	0
7.531	0	0	0	0	0	0	0	0	0

8.721	0	0	0	0	0	0	0	0	0
10.1	0	0	0	0	0	0	0	0	0
11.7	0	0	0	0	0	0	0	0	0
13.54	0	0	0	0	0	0	0	0	0
15.69	0	0	0	0	0	0	0	0	0
18.17	0	0	0	0	0	0	0	0	0
21.04	0	0	0	0	0	0	0	0	0
24.36	0	0	0	0	0	0	0	0	0
28.21	0	0	0	0	0	0	0	0	0
32.67	0	0	0	0	0	0	0	0	0
37.84	0	0	0	0	0	0	0	0	0
43.82	0	0	0	0	0	0	0	0	0
50.75	0	0	0	0	0	0	0	0	0
58.77	0	0	0	0	0	0	0	0	0
68.06	0	0	0.9	0	0	0	0	0	0
78.82	3	0	7.2	0	0	0	0	0	0
91.28	0	0	18.2	0	1.6	1.6	0	1.6	1.6
105.7	0.4	2.4	23.1	0	6.4	6.3	0	6.4	6.3
122.4	3.5	9.6	18.5	0.1	12.5	12.2	0.1	12.5	12.2
141.8	9.7	16.7	11.2	2.3	16.1	16.1	2.3	16.1	16.1
164.2	14.2	17.7	6	8.1	15.6	16	8.1	15.6	16
190.1	14.8	14.2	3.2	13.7	12.5	12.9	13.7	12.5	12.9
220.2	13.4	10.4	2.1	15.7	9.3	9.6	15.7	9.3	9.6
255	11.6	7.6	1.7	15.6	7.1	7.1	15.6	7.1	7.1
295.3	9.6	5.7	1.5	14.5	5.6	5.6	14.5	5.6	5.6
342	7.5	4.3	1.4	11.8	4.4	4.3	11.8	4.4	4.3
396.1	5.5	3.2	1.3	8.3	3.2	3	8.3	3.2	3
458.7	3.9	2.5	1.1	5.1	2.2	2	5.1	2.2	2
531.2	2.7	2	0.9	2.8	1.5	1.3	2.8	1.5	1.3
615.1	1.6	1.4	0.7	1.3	1	0.9	1.3	1	0.9

712.4	0.9	0.9	0.4	0.5	0.6	0.5	0.5	0.6	0.5
825	0.4	0.6	0.2	0.2	0.4	0.3	0.2	0.4	0.3
955.4	0.2	0.3	0.1	0	0.2	0.1	0	0.2	0.1
1106	0.1	0.2	0.1	0	0.1	0.1	0	0.1	0.1
1281	0	0.1	0	0	0	0	0	0	0
1484	0	0	0	0	0	0	0	0	0
1718	0	0	0	0	0	0	0	0	0
1990	0	0	0	0	0	0	0	0	0
2305	0	0	0	0	0	0	0	0	0
2669	0	0	0	0	0	0	0	0	0
3091	0	0	0	0	0	0	0	0	0
3580	0	0	0	0	0	0	0	0	0
4145	0	0	0	0	0	0	0	0	0
4801	0	0	0	0	0	0	0	0	0
5560	0	0	0	0	0	0	0	0	0
6439	0	0	0	0	0	0	0	0	0
7456	0	0	0	0	0	0	0	0	0
8635	0	0	0	0	0	0	0	0	0
1.00E+04	0	0	0	0	0	0	0	0	0

Table A23: Intensity % data for S13 silica nanoparticles at different pH values

Size (r.nm)	Mean Intensity % for S13											
	0.50 wt.%				0.75 wt.%				1 wt.%			
	pH =1	pH =2	pH =4	pH =7	pH =1	pH =2	pH =4	pH =7	pH =1	pH =2	pH =4	pH =7
0.2	0	0	0	0	0	0	0	0	0	0	0	0
0.2316	0	0	0	0	0	0	0	0	0	0	0	0
0.2682	0	0	0	0	0	0	0	0	0	0	0	0
0.3106	0	0	0	0	0	0	0	0	0	0	0	0
0.3597	0	0	0	0	0	0	0	0	0	0	0	0
0.4166	0	0	0	0	0	0	0	0	0	0	0	0

0.4825	0	0	0	0	0	0	0	0	0	0	0	0
0.5587	0	0	0	0	0	0	0	0	0	0	0	0
0.647	0	0	0	0	0	0	0	0	0	0	0	0
0.7493	0	0	0	0	0	0	0	0	0	0	0	0
0.8678	0	0	0	0	0	0	0	0	0	0	0	0
1.005	0	0	0	0	0	0	0	0	0	0	0	0
1.164	0	0	0	0	0	0	0	0	0	0	0	0
1.348	0	0	0	0	0	0	0	0	0	0	0	0
1.561	0	0	0	0	0	0	0	0	0	0	0	0
1.808	0	0	0	0	0	0	0	0	0	0	0	0
2.093	0	0	0	0	0	0	0	0	0	0	0	0
2.424	0	0	0	0	0	0	0	0	0	0	0	0
2.807	0	0	0	0	0	0	0	0	0	0	0	0
3.251	0	0	0	0	0	0	0	0	0	0	0	0
3.765	0	0	0	0	0	0	0	0	0	0	0	0
4.36	0	0	0	0	0	0	0	0	0	0	0	0
5.05	0	0	0	0	0	0	0	0	0	0	0	0
5.848	0	0	0	0	0	0	0	0	0	0	0	0
6.772	0	0	0	0	0	0	0	0	0	0	0	0
7.843	0	0	0	0	0	0	0	0	0	0	0	0
9.083	0	0	0	0	0	0	0	0	0	0	0	0
10.52	0	0	0	0	0	0	0	0	0	0	0	0
12.18	0	0	0	0	0	0	0	0	0	0	0	0
14.11	0	0	0	0	0	0	0	0	0	0	0	0
16.34	0	0	0	0	0	0	0	0	0	0	0	0
18.92	0	0	0	0	0	0	0	0	0	0	0	0
21.91	0	0	0	0	0	0	0	0	0	0	0	0
25.37	0	0	0	0	0	0	0	0	0	0	0	0
29.39	0	0	0	0	0	0	0.2	0	0	0	0	0
34.03	0	0	0	0	0	0	0.4	0	0	0	0	0

39.41	0.3	0	0	0	0.5	0	0.4	0.3	0	0	0	0
45.64	0.9	0.4	0	0	0.9	0	0.3	0.7	0	0	0.5	0
52.85	1.2	0.9	0.1	0	1.1	0.5	0.2	1	0	0.8	1	0
61.21	1	1.3	0.4	0	1.1	1.4	0.4	1	0	1.7	1	0
70.89	0.8	1.7	1.4	0	1.1	2.5	1.1	1.1	0	2.2	0.8	0.2
82.09	1.2	2.3	3	1.5	1.5	3.6	2.5	1.7	0.2	2.1	0.8	1.7
95.07	2.5	3.5	5.4	4.5	2.6	4.8	4.4	3	1.4	1.8	1.6	4.2
110.1	4.8	5.3	8	8.3	4.5	6.1	6.5	5	3.7	1.9	3.3	6.8
127.5	7.8	7.5	10.5	11.9	6.8	7.5	8.6	7.6	6.9	3	5.9	9
147.7	10.9	9.8	12.4	14.4	9.2	8.9	10.3	10.1	10.1	5	8.9	10.4
171	13.3	11.8	13.2	15.2	11.3	10.1	11.4	12.2	12.7	7.7	11.7	11.1
198	14.3	12.8	12.9	14.2	12.5	10.8	11.6	13.2	14.1	10.4	13.6	11
229.3	13.7	12.6	11.5	11.9	12.6	10.9	11	13	14.1	12.5	14.1	10.3
265.6	11.6	11.2	9.1	8.6	11.6	10.2	9.7	11.4	12.7	13.3	13.1	9.2
307.6	8.4	8.8	6.4	5.3	9.5	8.7	7.9	8.9	10.2	12.7	10.6	7.8
356.2	4.9	5.9	3.7	2.5	6.8	6.6	5.9	5.9	7.2	10.7	7.4	6.3
412.5	2	3.1	1.6	0.7	4.1	4.4	3.9	3	4.3	7.7	4.1	4.8
477.7	0.4	1.1	0.4	0	1.8	2.3	2.2	1	2	4.5	1.5	3.4
553.2	0	0.1	0	0	0.4	0.8	0.9	0	0.5	1.8	0.1	0
640.7	0	0	0	0	0	0.1	0.2	0	0	0.3	0	2.2
741.9	0	0	0	0	0	0	0	0	0	0	0	1.2
859.2	0	0	0	0	0	0	0	0	0	0	0	0.5
995.1	0	0	0	0	0	0	0	0	0	0	0	0.1
1152	0	0	0	0	0	0	0	0	0	0	0	0
1335	0	0	0	0	0	0	0	0	0	0	0	0
1545	0	0	0	0	0	0	0	0	0	0	0	0
1790	0	0	0	0	0	0	0	0	0	0	0	0
2073	0	0	0	0	0	0	0	0	0	0	0	0
2400	0	0	0	0	0	0	0	0	0	0	0	0
2780	0	0	0	0	0	0	0	0	0	0	0	0

3219	0	0	0	0	0	0	0	0	0	0	0	0
3728	0	0	0	0	0	0	0	0	0	0	0	0
4317	0	0	0	0	0	0	0	0	0	0	0	0
5000	0	0	0	0	0	0	0	0	0	0	0	0

Table A24: Intensity % data for S13 silica nanoparticles in the presence of 0.1 M NaCl

Size	Mean Intensity % for S13											
	0.50 wt.%				0.75 wt.%				1 wt.%			
(r.nm)	pH =1	pH =2	pH =4	pH =7	pH =1	pH =2	pH =4	pH =7	pH =1	pH =2	pH =4	pH =7
0.2	0	0	0	0	0	0	0	0	0	0	0	0
0.2316	0	0	0	0	0	0	0	0	0	0	0	0
0.2682	0	0	0	0	0	0	0	0	0	0	0	0
0.3106	0	0	0	0	0	0	0	0	0	0	0	0
0.3597	0	0	0	0	0	0	0	0	0	0	0	0
0.4166	0	0	0	0	0	0	0	0	0	0	0	0
0.4825	0	0	0	0	0	0	0	0	0	0	0	0
0.5587	0	0	0	0	0	0	0	0	0	0	0	0
0.647	0	0	0	0	0	0	0	0	0	0	0	0
0.7493	0	0	0	0	0	0	0	0	0	0	0	0
0.8678	0	0	0	0	0	0	0	0	0	0	0	0
1.005	0	0	0	0	0	0	0	0	0	0	0	0
1.164	0	0	0	0	0	0	0	0	0	0	0	0
1.348	0	0	0	0	0	0	0	0	0	0	0	0
1.561	0	0	0	0	0	0	0	0	0	0	0	0
1.808	0	0	0	0	0	0	0	0	0	0	0	0
2.093	0	0	0	0	0	0	0	0	0	0	0	0
2.424	0	0	0	0	0	0	0	0	0	0	0	0
2.807	0	0	0	0	0	0	0	0	0	0	0	0
3.251	0	0	0	0	0	0	0	0	0	0	0	0
3.765	0	0	0	0	0	0	0	0	0	0	0	0

4.36	0	0	0	0	0	0	0	0	0	0	0	0
5.05	0	0	0	0	0	0	0	0	0	0	0	0
5.848	0	0	0	0	0	0	0	0	0	0	0	0
6.772	0	0	0	0	0	0	0	0	0	0	0	0
7.843	0	0	0	0	0	0	0	0	0	0	0	0
9.083	0	0	0	0	0	0	0	0	0	0	0	0
10.52	0	0	0	0	0	0	0	0	0	0	0	0
12.18	0	0	0	0	0	0	0	0	0	0	0	0
14.11	0	0	0	0	0	0	0	0	0	0	0	0
16.34	0	0	0	0	0	0	0	0	0	0	0	0
18.92	0	0	0	0	0	0	0	0	0	0	0	0
21.91	0	0	0	0	0	0	0	0	0	0	0	0
25.37	0	0	0	0	0	0	0	0	0	0	0	0
29.39	0	0	0	0	0	0	0	0	0	0	0	0
34.03	0	0	0	0	0	0	0	0	0	0	0	0
39.41	0	0	0	1.6	0	0	0	0	0	0	0	0
45.64	0	0	0	8.3	0.2	0.1	0	0	0	0	0	0
52.85	0	0	0	17.1	0.5	0.5	0	0	0	0	0	0
61.21	0	0	0	19	0.8	0.9	0	0.1	0	0	0	0
70.89	0	0	0	14.5	0.9	1	0	0.9	0	0	0.1	0
82.09	0	0	0	9.5	1	0.9	0	2.2	0	0	0.8	1.2
95.07	0	0	0.3	6.1	1	0.8	0	3.6	0	0	1.7	3.4
110.1	0	0	1.2	4.3	1.2	1.1	0.5	4.9	0	0	2.5	5.9
127.5	0	0	2.7	3.6	1.8	2.1	2	5.9	0	2.4	3.1	8.1
147.7	1.5	0	4.4	3.4	3	3.9	4.6	6.8	0	6.5	3.6	9.3
171	4.9	0	6.2	3.2	4.6	6.1	7.7	7.6	0	10.9	4.1	9.7
198	8.4	0	7.7	2.7	6.6	8.5	10.9	8.3	0	14.3	4.8	9.4
229.3	10.8	1.6	8.8	2.2	8.5	10.7	13.3	8.9	0	15.8	5.5	8.5
265.6	11.1	6	9.4	1.7	10.1	12.1	14.5	9.2	3.7	15.1	6.3	7.3
307.6	9.7	11.9	9.5	1.2	11.1	12.6	14.2	9.2	12.9	12.6	7	6.2

356.2	7.1	17	9.1	0.9	11.3	11.9	12.4	8.7	21.8	9.1	7.6	5.2
412.5	4.2	19.5	8.5	0.5	10.6	10.2	9.6	7.8	25	5.5	8	4.4
477.7	1.8	18.3	7.6	0.3	9.2	7.7	6.2	6.4	20.8	2.5	8	3.8
553.2	0.4	14.1	6.5	0.1	7.2	5.1	3.1	4.7	1.2	0.7	7.7	3.4
640.7	0	8.3	5.4	0	5.1	2.6	1	3	3.6	0	7.1	3.1
741.9	0.4	3.1	4.3	0	3.1	0.9	0	1.5	0	0	6.2	2.7
859.2	1.5	0.2	3.3	0	1.5	0.1	0	0.5	0	0	5.1	2.4
995.1	2.9	0	2.3	0	0.5	0	0	0	0	0	4	2
1152	4.4	0	1.5	0	0.1	0	0	0	0	0	2.9	1.6
1335	5.5	0	0.9	0	0	0	0	0	0	0	1.9	1.1
1545	6.1	0	0.4	0	0	0	0	0	0	0	1.1	0.7
1790	6.1	0	0.1	0	0	0	0	0	0	0.2	0.5	0.4
2073	5.5	0	0	0	0	0	0	0	0	0.8	0.2	0.1
2400	4.4	0	0	0	0	0	0	0	0	1.5	0	0
2780	3.1	0	0	0	0	0	0	0	0	2.2	0	0
3219	0	0	0	0	0	0	0	0	0	0	0	0
3728	0	0	0	0	0	0	0	0	0	0	0	0
4317	0	0	0	0	0	0	0	0	0	0	0	0

Appendix B: Apparatus Information

7.1   Haake Viscometer manual:

ROTOVISCO RV 12

Berechnungsfaktoren
Calculation factors
Facteurs de calcul

Nr. 850195
Datum: 26.4.1985
Kontr.

M 150
Nr. 840305
a= 0,0147 $\left(\dfrac{N \cdot cm}{Skt}\right)$

System	Rotor	D/L (mm)	Nr.	M (min/s)	A $\left(\dfrac{Pa}{Skt}\right)$	G $\left(\dfrac{mPa \cdot s}{Skt \cdot min}\right)$
NV	NV	40.2 /60		5.41	0,533	98,6
MV T/MV	MV I	40.08/60		2.34	0,966	412
	MV II	36.8 /60		0.9	1,13	1250
	MV III	30.4 /60		0.44	1,63	3710
SV T/SV	SV I	20.2 /61.4		0.89	3,72	4175
	SV II	20.2 /19.6		0.89	11,3	12670
P	MV I P	40.08/60		2.0	0,966	483
	MV II P	36.8 /60		0.88	1,13	1282
	SV II P	20.2 /19.6		0.78	11,3	14460
DIN 53019	MV	38.7 /58.1		1.29	0,9	700
	SV	21.3 /32		1.29	5,43	4210
HS	HS I	19.95/15				
	HS II	19.8 /15				
	PK V,.........°	50 /--				
	PK I,.........°	28 /--				
	PK II,.........°	20 /--				
	MV SP	41.6/40				
	SV SP	20.2 /61.4				

KE Mess-Technik GmbH u. Co. · Dieselstraße 6 · D-7500 Karlsruhe 41 · Telefon (07 21) 40 94-1

6.2 Sensor System MV
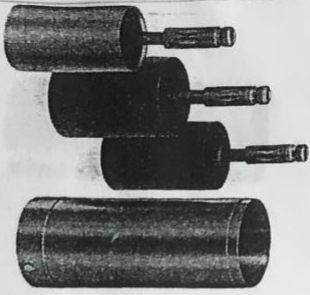
Application:

The MV is primarily used for viscosity measurements of m e d i u m v i s - c o u s liquids such as heavy oils, paints, varnishes, resins, emulsions, etc. Working in the medium shear rate range. Small yield points can be determined.

This coaxial cylinder sensor system consists of an MV cup used with three different rotors to provide different viscosity measuring ranges. MV I and MV II are both available in plastic (phenolic thermoset) and in stainless steel, 18/8. The plastic rotors are low weight and allow higher rates of rotor acceleration. They are mechanically and chemically safe for temperatures up to 100°C.

This sensor system requires the temperature vessel.

The rotors are positively mechanically centered. The top and the bottom surfaces of the rotors are recessed to minimize "end effects", i.e. their influence on torque. An air bubble is retained in the bottom recess, while the upper recess accomodates any excess sample.

The required amount of sample depends on the type of rotor used. For the purpose of reference there are two ring marks on the inside wall of the cup. The lower mark indicates the approximate sample volume required when the MV I and the MV II rotors are used in the cup MV. The upper ring mark is used for the MV III rotor.

Decreasing the temperature of a sample which just fills the annular gap between cup and rotor up to the upper rim of the rotor will cause the sample volume to shrink. This will lead to an only partly filled sensor system, to a reduced torque and to an erroneous viscosity value being below the true viscosity level.
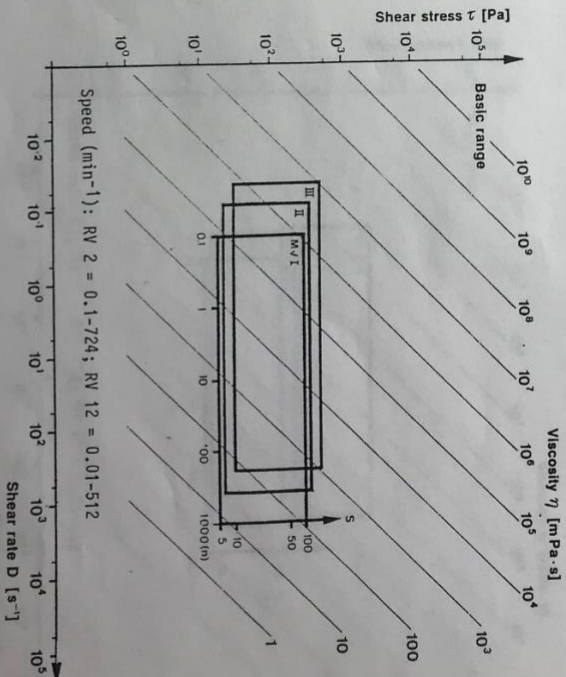
When a sample must be measured at various temperatures, it is advisable to begin at the lowest temperature. When this is not possible, the sensor system MV should be overfilled to such an extent that the sample will be slightly above the rim of the rotor even at the lowest temperature. Rotor alternative: MV DIN (see 6.6).

During a test the liquid level of the sample must just overflow into the upper recess of the rotor. The liquid level must not surpass the upper rim of the rotor by more than 1 or 2 mm. Excess sample may be removed by sucking it back by means of a syringe.

Cleaning: To remove the bottom of the cup, first loosen the knurled screw and re-move the cross-bar. (Order no. of sealing 807-0458)
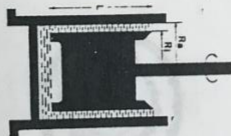
Sensor System	MV I	MV II	MV III
Inner Cylinder (rotor)			
radius R_i (mm)	20.04	18.4	15.2
height L (mm)	60	60	
Outer Cylinder (cup)			
radius R_a (mm)	21	21	21
Radii Ratio R_a/R_i	1.05	1.14	1.38
Sample Volume V (cm³)	40	55	70
Temperature: max. (°C)	100	100	100
min. (°C)	-30	-30	-30
Calculation Factors			
A (Pa/scale grad.)	3.22	3.76	5.44
M (min/s)	2.34	0.9	0.44
G (mPa·s/scale grad.·min)	1374	4171	12375

Shear stress τ [Pa]

Viscosity η [mPa·s]

Basic range

Speed (min-1): RV 2 = 0.1-724; RV 12 = 0.01-512

Shear rate D [s⁻¹]

Shear rate D

The shear rate 'D' is linearly linked to speed 'n':

$$D = M \cdot n \qquad (7)$$

The proportionality factor M recognizes the characteristic geometry of the sensor system. It is defined as the shear rate per speed unit. The following equations define this M factor:

Cylinder Sensor Systems

$$M = \frac{\pi}{15} \cdot \frac{R_a^2}{R_a^2 - R_i^2} \qquad (8)$$

Cone-and-Plate Sensor Systems

$$M = \frac{\pi}{30 \cdot \alpha} \qquad (9)$$

Note: The new SI-unit of an angle is the "radiant" rad. This correlates to the normally used "degree angle"(°):

$$1° = \frac{\pi}{180} \text{ rad } = 0.0174 \text{ rad}$$

Viscosity η:

The equation to calculate the viscosity of Newtonian liquids is:

$$\tau = \eta \cdot D \qquad (10)$$

When using the equations for τ (2) and D (7) this leads to:

$$A \cdot S = \eta \cdot M \cdot n$$

or with η:

$$\eta = \frac{A \cdot S}{M \cdot n} \qquad (11)$$

It is common practice to give viscosity in values of "milli Pascal seconds". Then (11) becomes:

$$\eta = 10^3 \cdot \frac{A \cdot S}{M \cdot n} \qquad (11a)$$

To simplify the equation a part of it is combined to a constant G being typical for each sensor system: ... can change ...

$$G = 10^3 \cdot \frac{A}{M} \qquad (12)$$

Thus the equation (11a) is changed to :

$$\eta = \frac{G \cdot S}{n} \quad (mPa \cdot s) \qquad (13)$$

8.2 Determination of instrument constants

Shear rate D, shear stress τ, and viscosity η, are computed from test results of 'n' and 'S' with the sensor factors 'M' (shear rate factor), 'A' (shear stress factor), and 'G' (viscosity factor). These factors are found in the list of calculation factors delivered with each instrument. They were established by means of an absolute test of 'weighing torques' or they are, as for instance 'M' and 'f', calculated by using the geometrical dimensions of the sensor system:

Sensor system	f . 10⁻⁴ (cm⁻³)	M (min/s)
NV	36.3	5.41
MV I / T I	65.7	2.34
MV II	76.8	0.90
MV II / T II	111	0.44
MV III	65.8	2.0
MV I P	76.8	0.88
MV II P	87.8	11 *
MV SP	253	0.89
SV I	768	0.89
SV II P	768	0.78
SV II P	572	---
SV II FL	253	4.4
SV SP	55.8	1.29
MV DIN	369.4	1.29
SV DIN	61.43	1.29
MV-E	322.1	40 *
SV-E	1172	10 *
HS I	1142	6 *
HS II	305.6	6 *
PK V, 1°	1740	6 *
PK I, 1°	4775	12 *
PKII, 1°	305.6	12 *
PK V, 0.5°	1740	12 *
PK I, 0.5°	4775	20 *
PKII, 0.5°	305.6	20 *
PK V, 0.3°	1740	20 *
PK I, 0.3°	4775	
PKII, 0.3°	4775	

* the factors given are values for reference only; for exact values, see list of calculation factors.

In case that an instrument is expanded by further measuring-drive-units the relevant values A for the range of sensor systems must be calculated:

Example - you need 'A', 'M' for RV 12 with M 150 and MV I.

The value 'a' of the measuring-drive-unit M 150 is 0.0147 Ncm/scale grad.

M 150 is 0.0147 Ncm/scale grad.
M 500 is 0.049 Ncm/scale grad.
M 1500 is 0.147 Ncm/scale grad.

$$A = f \cdot a = f(MV\ I) \cdot a(M\ 150)$$

Calculation of shear stress factor 'A':

A = 65.7 · 10⁻⁴ cm³ · 0.0147 Ncm/scale grad.
A = 0.966 (Pa/scale grad.)
Taken from the above table.

A = 0.966 · 10⁻⁴ N/cm² · scale gr...

Calculation of shear stress factor 'M':

Calculation of viscosity factor 'G':

$$G = \frac{A}{M} \cdot 1000 = \frac{0.966}{2.34} \cdot 1000 = 413$$

8.3 Calibration

The Rotovisco has been calibrated before delivery. However, the calibration may also be carried out by the customer, which, of course, requires strict adhering to the instructions of the manufacturer. It is of utmost importance to maintain the temperature indicated on the bottle of the standard liquid (±0.01°C, or at least ±0.05°C). The procedure consists of determining the "S" values for each given "n"-value. The constant for the particular sensor system can be found using the following equation:

$$G = \frac{\eta \cdot n}{S} \quad \text{(mPa·s/scale grad. · min)}$$

Whereby η represents the viscosity of the standard liquid in mPa·s as noted on bottle.

The shear stress factor A of the rotor can be determined from the following equation:

$$A = 10^{-3} \cdot \frac{\eta \cdot n \cdot M}{S} \quad \text{(Pa/scale grad)}$$

The shear rate factor M can be obtained from the list of calculation factors.

We supply the following standard liquids:

Order designation

7	Viscosity (mPa·s)	Reference temperature (°C)
200	ca. 4.5	
2 000	140	20
6 000	1 840	20
13 000	5 990	20
30 000	14 780	20
70 000	25 780	20
	66 570	10

The viscosity values given above are typical values for reference only. The exact values with reference to temperature and date are noted on each bottle.

The standard liquids can be supplied in quantities of 50, 100 and 250 cm³. The liquids should be stored in a cool and dark place.

Since standard liquids can change with time, the specifications given only apply a period of 3 months after delivery.

9.0 Measurements

To measure viscosity values, speeds or speed programs have to be preset and the resulting torque recorded. Substances, showing a time dependent viscosity value (thixotropic liquids), should be measured with a speed program using an x-y-recorder or, at fixed speed, with a y-t-recorder.

Advice on instrument settings

a) Sensitivity 'E'

The torque reading 'S' should be between 10 and 100 scale grad, which calls for setting E 1 or E 0.3. A further extension/reduction is possible through other measuring-drive-units and different sensor systems

b) Reduction 'R'

The setting of 'R' is given by the required shear rate range and the sensor used. High shear rates are possible in R 1 but for measuring the yield points or the thixotropic recovery, low shear rates should be used with setting R 10 or R 100. A speed resulting with a setting of R 10 is more accurate than a comparable speed with R 1.

c) Time settings using PG 142

Selecting t_1 is defined as the hold time period. It starts by depressing the push-button ⬦ and ends when tests actually start with rotation. If t_1 is too short, a constant temperature before starting a test cannot be guaranteed and, as a result, the reproducibility of the test results could be low.

The length of t_1 required in order to always guarantee identical test temperatures, will depend on the following:

- type of sample and its specific heat coefficient;
- temperature difference between ambient and required test temperature;
- type of sensor system selected: Gap size between inner cylinder and beaker, surface area of the inner cylinder, wall thickness of the beaker, etc.
- type of circulator used to control the temperature.

Values of $t_1 = 2$ min will be acceptable for many watery samples to be tested at or slightly above room temperature. Testing pastes or creames at temperatures above 30°C may require a $t_1 = 4$ min or more. What is suitable as t_1 must be determined by preliminary tests.

7.2   Fann Viscometer manual:

2. FANN Model 35 Viscometer

1   Introduction

Fann Model 35 viscometers are direct-reading instruments which are available in six- speed and twelve- speed designs for use on either 50 Hz or 60 Hz electrical power. The standard power source is 115 volts, but all models may be fitted with a transformer, making operation with 220/230 volts possible.

Fann Model 35 viscometers are used in research and production. These viscometers are recommended for evaluating the rheological properties of fluids, Newtonian and non-Newtonian. The design includes a R1 Rotor Sleeve, B1 Bob, F1 Torsion Spring, and a stainless steel sample cup for testing according to American Petroleum Institute Recommended Practice for Field Testing Water Based Drilling Fluids, API RP 13B-1/ISO 10414-1 Specification.

1.1   Background

Fann Model 35 viscometers are Couette rotational viscometers. In this viscometer, the test fluid is contained in the annular space (shear gap) between an outer cylinder and the bob (inner cylinder). Viscosity measurements are made when the outer cylinder, rotating at a known velocity, causes a viscous drag exerted by the fluid. This drag creates a torque on the bob, which is transmitted to a precision spring where its deflection is measured.

Viscosity measured by a Couette viscometer, such as the Model 35, is a measure of the shear stress caused by a given shear rate. This relationship is a linear function for Newtonian fluids (i.e., a plot of shear stress vs. shear rate is a straight line).

The instrument is designed so that the viscosity in centipoise (or millipascal second) of a Newtonian fluid is indicated on the dial with the standard rotor R1, bob B1, and torsion spring F1 operating at 300 rpm. Viscosities at other test speeds may be measured by using multipliers of the dial reading. A simple calculation that closely approximates the viscosity of a pseudo-plastic fluid, such as a drilling fluid is described in Section 7.

The shear rate may be changed by changing the rotor speed and rotor-bob combination. Various torsion springs are available and are easily interchanged in order to broaden shear stress ranges and allow viscosity measurements in a variety of fluids.

64

101

5.1   Operating the Model 35A and 35SA

The Model 35A and 35SA viscometers operate at six speeds, ranging from 3 rpm to 600 rpm. To select the desired speed, set the speed switch (located on the right side of the base) to the high or low speed position as desired. Then turn the motor on and move the gear shift knob (located on the top of the instrument) to the position that corresponds to the desired speed.

Table 5-1 lists the positions for the viscometer switch and the gear knob combinations to obtain the desired speed. The viscometer gear shift knob may be engaged while the motor is running. Read the dial for shear stress values.

Table 5-1 Six-Speed Testing Combinations for Models 35A and 35SA

Speed RPM	Viscometer Switch	Gear Shift Knob
600	High	Down
300	Low	Down
200	High	Up
100	Low	Up
6	High	Center
3	Low	Center

5.2

Operating the Model 35A/SR-12 and 35SA/SR-12

The Model 35A/SR-12 and 35SA/SR-12 have twelve speeds for testing capabilities. To achieve this broader testing range from 0.9 rpm to 600 rpm, an additional gear box shift lever is used; it is located on the right side of the gear box. See Figure 5-1. Move this lever to the left or right as determined from Table 5-2.

Never change the gear box shift lever while the motor is running. Changing it while the motor is running will result in gear damage.

Only the viscometer gear shift knob (on top of the instrument) can be changed while the motor is running.

68

102

Table 3-3 Rotor and Bob Dimensions

Unit	Radius (cm)	Length (cm)	Cylinder Area (cm^2) x Radius (cm)
B1	1.7245	3.8	71.005
B2	1.2276	3.8	35.981
B3	0.86225	3.8	17.751
B4	0.86225	1.9	8.876
R1	1.8415	n/a	n/a
R2	1.7589	n/a	n/a
R3	2.5867	n/a	n/a

Table 3-4 Rotor-Bob Specifications

ROTOR-BOB	R1 B1	R2 B1	R3 B1	R1 B2	R1 B3	R1 B4
Rotor Radius, R_0 (cm)	1.8415	1.7588	2.5866	1.8415	1.8415	1.8415
Bob Radius, R_i (cm)	1.7245	1.7245	1.7245	1.2276	0.8622	0.8622
Bob Height, L (cm)	3.8	3.8	3.8	3.8	3.8	1.9
Shear Gap in Annulus (cm)	0.117	0.0343	0.8261	0.6139	0.9793	0.9793
Radii Ratio, R_i/R_0	0.9365	0.9805	0.667	0.666	0.468	0.468
Maximum Use Temperature (^{o}C)	93	93	93	93	93	93
Minimum Use Temperature (^{o}C)	0	0	0	0	0	0

Table 3-5 Range of Environmental Conditions

Maximum Altitude	6562 ft (2000 m)
Temperature Range	41°F to 104°F (5°C to 40°C)
Maximum Relative Humidity (RH)	80% RH at 87.8^{o}F (31°C) or less 50% RH at 104°F (40°C)

67

103

Table 3-1 Model 35 Viscometer Specifications

Model No.	Part No.	Electrical	No. of Speeds	Speeds
35A	207198	115V, 60 Hz, 90W	6	600, 300, 200, 100, 6, 3
35SA	207199	115V, 50 Hz, 90W	6	600, 300, 200, 100, 6, 3
35A/SR-12	207200	115V, 60 Hz, 90W	12	600, 300, 200, 180, 100, 90, 60, 30, 6, 3, 1.8, 0.9
35SA/SR-12	207201	115V, 50 Hz, 90W	12	600, 300, 200, 180, 100, 90, 60, 30, 6, 3, 1.8, 0.9

Table 3-2 Model 35 Viscometer Sizes

Model No.	Part No.	Dimensions (LxDxH)	Weight
35A	207198	15.2 x 6 x 10.5 in. 39 x 15 x 27 cm	15 lb 6.8 kg
35SA	207199	15.2 x 6 x 10.5 in. 39 x 15 x 27 cm	15 lb 6.8 kg
35A/SR-12	207200	15.2 x 6 x 10.5 in. 39 x 15 x 27 cm	15 lb 6.8 kg
35SA/SR-12	207201	15.2 x 6 x 10.5 in. 39 x 15 x 27 cm	15 lb 6.8 kg
35A w/ case	101671768	8 x 16 x 19 in. 20.3 x 40.6 x 48.3 cm	26 lb 11.8 kg
35SA w/ case	101671770	8 x 16 x 19 in. 20.3 x 40.6 x 48.3 cm	26 lb 11.8 kg

66

104

3   Features and Specifications

The Fann direct-indicating viscometers are equipped with the standard R1 rotor sleeve, B1 bob, F1 torsion spring, and a stainless steel sample cup. Other rotor-bob combinations and/or torsion springs can be substituted to extend the torque measuring range or increase the sensitivity of the torque measurement.

Each viscometer is supplied with a 115 volt motor. For operation on 230 volts, a step-down transformer is required.

The viscometers are available in six-speed and twelve-speed models.
See Table 3-1, Table 3-2, Table 3-3 and Table 3-4for specifications. Table 3-5 lists the recommended environmental conditions for use.

The photo in Figure 3-1 shows the viscometer and the detailed drawing in Figure 3-2 identifies the individual parts.

Figure 3-1 Model 35SA Viscometer

65

105